

**THE ROLE OF STRAIN AND STRUCTURE ON OXYGEN ION
CONDUCTION IN NANOSCALE ZIRCONIA AND CERIA THIN FILMS**

by

Jun Jiang

A dissertation submitted to the Faculty of the University of Delaware in partial fulfillment of the requirements for the degree of Doctor of Philosophy in Materials Science and Engineering

Summer 2014

© 2014 Jun Jiang
All Rights Reserved

UMI Number: 3642318

All rights reserved

INFORMATION TO ALL USERS

The quality of this reproduction is dependent upon the quality of the copy submitted.

In the unlikely event that the author did not send a complete manuscript and there are missing pages, these will be noted. Also, if material had to be removed, a note will indicate the deletion.



UMI 3642318

Published by ProQuest LLC (2014). Copyright in the Dissertation held by the Author.

Microform Edition © ProQuest LLC.

All rights reserved. This work is protected against unauthorized copying under Title 17, United States Code



ProQuest LLC.
789 East Eisenhower Parkway
P.O. Box 1346
Ann Arbor, MI 48106 - 1346

**THE ROLE OF STRAIN AND STRUCTURE ON OXYGEN ION
CONDUCTION IN NANOSCALE ZIRCONIA AND CERIA THIN FILMS**

by

Jun Jiang

Approved:

Darrin Pochan, Ph.D.

Chair of the Department of Materials Science and Engineering

Approved:

Babatunde Ogunnaike, Ph.D.

Dean of the College of Engineering

Approved:

James G. Richards, Ph.D.

Vice Provost for Graduate and Professional Education

I certify that I have read this dissertation and that in my opinion it meets the academic and professional standard required by the University as a dissertation for the degree of Doctor of Philosophy.

Signed:

Joshua L. Hertz, Ph.D.
Professor in charge of dissertation

I certify that I have read this dissertation and that in my opinion it meets the academic and professional standard required by the University as a dissertation for the degree of Doctor of Philosophy.

Signed:

Ajay K. Prasad, Ph.D.
Member of dissertation committee

I certify that I have read this dissertation and that in my opinion it meets the academic and professional standard required by the University as a dissertation for the degree of Doctor of Philosophy.

Signed:

Chaoying Ni, Ph.D.
Member of dissertation committee

I certify that I have read this dissertation and that in my opinion it meets the academic and professional standard required by the University as a dissertation for the degree of Doctor of Philosophy.

Signed:

Joshua Zide, Ph.D.
Member of dissertation committee

ACKNOWLEDGMENTS

In the process of my Ph.D. study, research and writing up of this thesis, I received a lot of help from many kind people around. At first, I would like to thank my advisor, Dr. Joshua L. Hertz, who guides me in the research. The most important thing he taught me is that what is science and how to do research. Dr. Hertz always answers my questions with a lot of patience and shows me the fundamentals, not just the answer itself but how to solve the problems. Moreover, he spent a lot of time involving in my experiments and working with me to find the way forward.

I also would like to thank other members of my thesis committee, Dr. Prasad, Dr. Zide and Dr. Ni. I really appreciate their spending time on carefully reviewing my dissertation and providing constructive suggestions on my research project.

I thankfully acknowledge my dear group mates. Weida Shen, the collaborator in this project worked with me to push the project forward and made many findings; Philip Zandona taught me handling the sputter system and preparing the samples; Ning Ye was always around and willing to take the discussions. Their supports mean a lot to me and assist me finishing the study and research.

In addition, the persons in EM Lab helped a lot in my EM work. Dr. Ni, who taught me the EM course and led me into the microscopy world and offered a lot of advices in the EM work. Fei Deng and Frank showed me how to operate the

instruments with great patience. For the EM work, Dr. Wanfeng Li made important contributions to the TEM samples preparation. Jonathan Dickason helped me working on the photolithography work with the proficiency.

Above all, I would like to thank my wife, who not only helped a lot in the XRD and EM work with her proficiency, but also offered all kinds of ideas for setting up the experiments. Her solid support helps me a lot in both my daily life and research and contributes a lot to this thesis.

Finally, I acknowledge the funding source of my project, the U.S. Department of Energy, Office of Basic Energy Sciences, Division of Materials Science and Engineering under Award DE-SC0005403.

TABLE OF CONTENTS

LIST OF TABLES	ix
LIST OF FIGURES	x
ABSTRACT	xvii

Chapter

1	INTRODUCTION	1
1.1	Solid Oxide Fuel Cells.....	2
1.2	Solid Electrolytes.....	4
1.3	Zirconia- and Ceria-based Solid Oxide Electrolytes	6
1.4	Zirconia-based Thin Films	11
1.4.1	Increased Conductivities with Nanoscale Thin Films	16
1.4.2	Decreased Conductivities with Nanoscale Thin Films.....	19
1.4.3	Unaltered Conductivities with Nanoscale Thin Films.....	20
1.4.4	Effect of Thickness on Conductivity	21
1.4.5	Effect of Substrate on Conductivity	24
1.4.6	Effect of Microstructure on Conductivity	25
1.4.7	Effect of Strain on Conductivity.....	27
1.5	Ceria-based Thin Films	32
1.6	Summary of the Literature.....	33
1.7	Objective of Thesis.....	35
2	EXPERIMENTATION	37
2.1	Zirconia- and Ceria-based Thin Films Preparation	37
2.1.1	Sputter Deposition of Controlled Composition.....	37
2.1.2	Post Annealing.....	44
2.1.3	Substrate Preparation.....	45
2.2	Structural Characterization	46
2.2.1	X-ray Diffraction.....	46
2.2.2	Scanning Electron Microscopy.....	47
2.2.3	Atomic Force Microscopy.....	48

2.2.4	Transmission Electron Microscopy	48
2.3	Compositional Characterization	49
2.4	Interdigitated Electrode Fabrication	50
2.5	Electrochemical Characterization.....	52
3	RESULTS.....	54
3.1	Structural Characterization of YSZ Thin Films	54
3.1.1	Structural Characterization of YSZ Thin Films on MgO Single Crystal.....	54
3.1.2	Structural Characterization of YSZ Thin Films on Al ₂ O ₃ Single Crystal	67
3.2	Structural Characterization of GDC Thin Films	78
3.2.1	Structural Characterization of GDC Thin Films on MgO Single Crystal.....	78
3.2.2	Structural Characterization of GDC Thin Films on Al ₂ O ₃ Single Crystal	81
3.3	Electrochemical Characterization of YSZ and GDC Thin Films	84
3.4	Electrochemical Properties of YSZ Thin Films	87
3.4.1	Electrochemical Properties of YSZ Thin Films on MgO Single Crystal.....	87
3.4.2	Electrochemical Properties of YSZ Thin Films on Al ₂ O ₃ Single Crystal	92
3.5	Increased Conduction of YSZ Thin Films in Humid Air	100
3.6	Electrochemical Properties of GDC Thin Films	104
4	DISCUSSION.....	107
4.1	Role of Strain on Oxygen Ion Conduction in Zirconia- and Ceria- based Thin Films	107
4.2	Role of Structure on Oxygen Ion Conduction in Zirconia- and Ceria- based Thin Films	116
4.3	Proton Conduction supported by YSZ Thin Films.....	119
5	CONCLUSIONS	124
5.1	Summary.....	124
5.2	Recommendations for Future Work	126

REFERENCES	129
Appendix	
A REPRINT PERMISSION LETTERS.....	136

LIST OF TABLES

Table 1	Literature review on bulk YSZ with respect to their microstructure and dopant concentration, as shown in Figure 6.....	12
Table 2	Literature review on YSZ thin films with respect to their dopant concentration, substrate, processing method and thickness, as shown in Figure 7.....	16
Table 3	Annealing conditions for the post-annealed samples.....	44
Table 4	The geometry values of electrodes.....	50
Table 5	Deposition conditions for the samples plotted in Figure 18.....	56
Table 6	Lattice parameters and grain sizes for the samples in Figure 36.....	76
Table 7	Sample information in Figure 44 and Figure 45.....	90
Table 8	Activation energies of the $\sigma \cdot T$ product of all samples in Figure 46.....	92
Table 9	Activation energy of the $\sigma \cdot T$ product of all samples in Figure 49.....	97
Table 10	Activation energies for the samples in Figure 50.....	99

LIST OF FIGURES

Figure 1	Schematic diagram of a solid oxide fuel cell.	3
Figure 2	The phase diagram of YSZ. Reprinted with permission from reference [7].	7
Figure 3	The doping and vacancy transport in YSZ. Reprinted from reference [8].	8
Figure 4	Composition dependence of the electrical conductivity at 1000 °C for (ZrO ₂) _{1-x} (Ln ₂ O ₃) _x . Reprinted with permission from reference [9].	9
Figure 5	Temperature dependence of electrical conductivity for oxide ion conductor. Reprinted with permission from reference[10].	10
Figure 6	Arrhenius plots of the electrical conductivities of YSZ bulk samples (both single crystal and polycrystalline) taken from a number of literature sources (data references are listed in Table 1). In the plot, the line represents typical values reported for bulk YSZ, calculated as a linear regression of all of the data presented in the plot. Reprinted from reference [38].....	13
Figure 7	Arrhenius plots of the electrical conductivities of YSZ thin films taken from a number of literature sources (data references are listed in Table 2). In the plot, the line represents typical values reported for bulk YSZ, calculated as a linear regression of all of the data presented in Figure 6. Reprinted from reference [38].	15
Figure 8	The values reported for electrical conductivities at 500 °C of YSZ thin films as a function of their thickness indicate a positive correlation between film thickness and experimental repeatability. The inset presents the same information in a double log scale. The symbols represent data from the same references as indicated in Figure 7. Unlike Figure 7, plotted here are the data from all films reported in these references, not just the films that maximally deviate from the expected value. Note that some values are interpolated or extrapolated from original data to 500 °C. The black dashed line represents an average conductivity of bulk YSZ at 500 °C. Dotted lines are guides for the eye. Reprinted from reference [38].	23

Figure 9	Arrhenius plots of electrical conductivities of YSZ thin films with similar thickness grown on substrates of MgO or Al ₂ O ₃ . The symbols represent the same data as indicated in Figure 7. Reprinted from reference [38]... 24	24
Figure 10	Plot of the logarithm of the maximum change $\sigma_{tot}/\sigma_{vol}$ of the total conductivity relative to the bulk conductivity against the mismatch factor f_{YSZ}/Ins . Reprinted with permission from reference [41]. 30	30
Figure 11	Schematic diagram of RF magnetron sputtering..... 38	38
Figure 12	Schematic diagram of co-sputtering 39	39
Figure 13	(a) Side view of a sharp step and (b) a histogram of the interferometer measurement..... 40	40
Figure 14	Deposition rate of ZrO ₂ (a), CeO ₂ (b), Y ₂ O ₃ (c), and Gd ₂ O ₃ (d) films as a function of sputtering power. Reprinted from reference [11]. 40	40
Figure 15	The relationship between the expected atomic ratio and the actual atomic ratio in deposition of YSZ (a) and GDC (b). Reprinted from reference [11]. 43	43
Figure 16	Schematic diagram of various substrate surfaces 45	45
Figure 17	Representative microscopy (left) and 3D image (right) of the electrodes. 52	52
Figure 18	XRD patterns of various YSZ thin films on MgO (100). The deposition details of these films are listed in table 5. Peaks marked with a circle are indicative of the substrate. Other peaks are marked with Miller indices at the locations expected of cubic YSZ planes. Reprinted from reference [73]. 54	54
Figure 19	θ -2 θ XRD pattern of a pure ZrO ₂ film deposited on MgO (100). ZrO ₂ monoclinic peak appears at 2 θ \square 28°. Reprinted from reference [11]..... 56	56
Figure 20	XRD patterns of 50 nm thick, 14 mol% YSZ thin films deposited at 400 °C on MgO (100) substrates from Across International. Peaks marked with a circle are indicative of the substrate. Other peaks are marked with Miller indices at the locations expected of cubic YSZ planes. Reprinted from reference [73]...... 57	57
Figure 21	XRD patterns of 9 mol% YSZ thin films deposited at 650 °C on MgO (100) substrates from MTL. Samples (i) and (ii) are 50 nm thick, while	

	sample (iii) is 12 nm thick. Peaks marked with a circle are indicative of the substrate. Other peaks are marked with Miller indices at the locations expected of cubic YSZ planes. Reprinted from reference [73].	58
Figure 22	(a) Bright field image and (b) selected area electron diffraction of a (111) oriented YSZ thin film (film (iii) in Table 5). Reprinted from reference [73].	59
Figure 23	Selected area electron diffraction of a (100)-oriented YSZ thin film (film (i) in Table 5) Reprinted from reference [73].	61
Figure 24	XRD patterns of 9 mol% YSZ thin films deposited on MgO (110) substrates from MTI at 650 °C ((i) and (ii) are 50 nm thick YSZ thin films while (iii) is a 12 nm thick YSZ thin film). Peaks marked with a circle are indicative of the substrate. Other peaks are marked with Miller indices at the locations expected of cubic YSZ planes. Reprinted from reference [73].	62
Figure 25	XRD patterns of 9 mol% YSZ thin films deposited on MgO (111) substrates from MTI at 650 °C ((i) and (ii) are 50 nm thick YSZ thin films while (iii) are 12 nm thick YSZ thin film). Peaks marked with a circle are indicative of the substrate. Other peaks are marked with Miller indices at the locations expected of cubic YSZ planes. Reprinted from reference [73].	63
Figure 26	(a) AFM image of milled surface of MgO (or Al ₂ O ₃) and (b) height profile along the path indicated with a dashed line. In part (a), height is indicated by shade where the scale from black to white is 800 nm. Reprinted from reference [76].	65
Figure 27	XRD patterns of YSZ thin films on MgO. While the patterns are offset for clarity, all are plotted over the same intensity scale. Reprinted from reference [76].	66
Figure 28	θ -2 θ XRD pattern of YSZ thin films with thickness 6 nm (i), 12 nm (ii), 50 nm (iii), 100 nm (iv). Note that the plotted intensity is logarithmic. The peaks near 29° and 62° indicated with asterisks represent YSZ (111) and (222), respectively; the truncated peak near 43° and indicated with the circle is Al ₂ O ₃ (0006). Reprinted from reference [32].	67
Figure 29	The lattice parameter of YSZ thin films on Al ₂ O ₃ determined from XRD both before and after impedance measurement at 650 °C. Reprinted from reference [32].	68

Figure 30	AFM image of 50 nm thick YSZ thin films deposited on Al ₂ O ₃	69
Figure 31	(a) Bright-field image and (b) dark-field image of a 50 nm thick, as-deposited YSZ thin film. Reprinted from reference [32].	70
Figure 32	(a) high resolution cross-sectional image of a 50 nm thick, as-deposited YSZ thin film. High resolution image of 6 nm thick YSZ thin films (b) as-deposited and (c) after high temperature impedance measurements. The red marks indicate edge dislocations. Reprinted from reference [32].	71
Figure 33	(a) In-plane and (b) cross-section electron diffraction of 50 nm thick as-deposited YSZ thin films. Reprinted from reference [32].	72
Figure 34	Solid sphere model of YSZ/Al ₂ O ₃ interface. Green, blue, and red spheres represent Zr/Y, Al, and O, respectively. Reprinted from reference [32].	73
Figure 35	XRD patterns of YSZ thin films on Al ₂ O ₃ . While the patterns are offset for clarity, all except the polished sapphire sample are plotted over the same intensity scale. The film on polished sapphire had a very high peak intensity and is plotted with values reduced by a factor of 1/10. Reprinted from reference [76].	74
Figure 36	XRD patterns of YSZ thin films as-deposited (a) and after annealing (b).	75
Figure 37	θ -2 θ XRD patterns of GDC film deposited on MgO (100). Reprinted from reference [11].	78
Figure 38	Plan view SAED pattern of GDC films deposited on MgO (100) substrate. Reprinted from reference [11].	79
Figure 39	θ -2 θ XRD pattern of a bilayer film of GDC and YSZ deposited on MgO (100). A sketch of the heterostructure is shown in the inset. Reprinted from reference [11].	80
Figure 40	θ -2 θ XRD pattern of GDC thin films with thickness 15 nm (i), 30 nm (ii), 81 nm (iii), 119 nm (iv), 146 nm (v), 173 nm (vi). Note that the plotted intensity is logarithmic. The peaks near 28° and 59° indicated with asterisks represent GDC (111) and (222), respectively; the truncated peak near 43° and indicated with the circle is Al ₂ O ₃ (0006). Reprinted from reference [69].	81

Figure 41	(a) Bright field and (b) dark field (with grain boundaries indicated) TEM images of GDC thin films on Al ₂ O ₃ . (c) Selected area electron diffraction of GDC thin films on Al ₂ O ₃ . Reprinted from reference [69].	82
Figure 42	Representative impedance spectra of the 81 nm thick GDC film in air at the temperatures indicated in the plot. The inset shows the equivalent circuit used to fit the impedance spectra (R = resistor, CPE = constant phase element). Reprinted from reference [80].	84
Figure 43	Resistance of (a) MgO and (b) Al ₂ O ₃ substrates with No. 2 Pt electrodes.	86
Figure 44	Arrhenius plot of the conductivity of 50 nm thick YSZ thin films ((100) YSZ on MgO (100) has a dopant concentration of 14 mol%; all other films have 9 mol%) as well as a single crystal YSZ substrate with nominally similar composition. The dashed line gives reference values from Guo[33]. Reprinted from reference [73].	87
Figure 45	Arrhenius plot of the conductivity of 12 nm thick 9 mol% YSZ thin films as well as a single crystal YSZ substrate with nominally similar composition. Reprinted from reference [73].	89
Figure 46	Arrhenius plot of the conductivity of YSZ thin films on MgO (100). Measurements from a single crystal YSZ substrate with nominally similar composition are also provided for reference. Reprinted from reference [76].	91
Figure 47	Arrhenius plot of the initial (a) and final (b) conductivity of the 9 mol% YSZ thin films. Also shown is the conductivity evolution during repeated measurement of the film with thickness 6 nm (c), 12 nm (d), 25 nm (e), and 100 nm (f). Reprinted from reference [32].	93
Figure 48	(a) Arrhenius plot of the stable conductivity of 14 mol% YSZ thin films. (b) The temperature dependence of the conductivity of the 100 nm thick 9 mol% YSZ film, the 100 nm thick 14 mol% YSZ film, and a roughly 8 mol% YSZ single crystal. Reprinted from reference [32].	94
Figure 49	Arrhenius plot of the conductivity of YSZ thin films on Al ₂ O ₃ (0001). Measurements from a single crystal YSZ substrate with nominally similar composition are also provided for reference. Reprinted from reference [76].	96

Figure 50	Arrhenius plot of the conductivity of YSZ thin films as deposited and annealed. Measurements from a single crystal YSZ substrate with nominally composition of 8 mol% are also provided for reference.	98
Figure 51	Impedance spectra of the 50 nm (a) and 6 nm (b) thick films in both dry air and humidified air near 500 °C. The measurement frequency of a few data points are indicated. Note that the scale is different in plots (a) and (b). The gaps in data in the upper-right portions of the semicircles in plot (b) are due to an inability to collect low-noise measurements at frequencies near 3500 Hz (a repeatable interference from an unknown source).	100
Figure 52	Arrhenius plot of the conductivity of (a) the 50 nm thick YSZ thin film measured in flowing dry air and humidified air with a water vapor partial pressure of 32 mbar and (b) the 6 nm thick YSZ thin film measured in flowing dry air, open lab air, and humidified air with a water vapor partial pressure of 32 mbar.	102
Figure 53	Arrhenius plot of conductivity of GDC thin films with thickness of 15 nm, 30 nm, 81 nm, 119 nm, 146 nm, 173 nm. Solid line represents the literature value for the grain conductivity of the bulk GDC [81]. Reprinted from reference [69].	104
Figure 54	The oxygen partial pressure dependence of conductivity of GDC thin films with thickness of 15 nm, 81 nm, 146 nm and 173 nm at 500 °C. Reprinted from reference [69].	105
Figure 55	The thickness dependence of conductivity of YSZ thin films on Al ₂ O ₃	107
Figure 56	The relationship between lattice strain and activation energies.....	108
Figure 57	(a) The out-of-plane equivalent lattice parameter of GDC thin films on Al ₂ O ₃ determined from XRD and (b) The out-of-plane strain of GDC thin films on Al ₂ O ₃ determined from XRD. Reprinted from reference [69].	112
Figure 58	The thickness dependence of the (a) conductivity at 500 °C and (b) activation energy of the $\sigma \cdot T$ product (squares represent fresh samples, triangles represent annealed samples). Reprinted from reference [69].	114
Figure 59	Schematic diagram of proton conduction	120

Figure 60	Arrhenius plot of the surface conductivity of the 6 nm thick YSZ thin film measured in the flowing humidified air with a water vapor partial pressure of 32 mbar	122
Figure 61	The thickness dependence of conductivity at 500 °C	123

ABSTRACT

Solid oxide fuel cells (SOFCs), an all solid-state energy conversion device, are promising for their high efficiency and materials stability. The solid oxide electrolytes are a key component that must provide high ionic conductivity, which is especially challenging for intermediate temperature SOFCs operating between 500 °C - 700 °C. Doped zirconia and ceria are the most common solid electrolyte materials.

Recent reports have suggested that nanoscale yttria stabilized zirconia (YSZ) thin films may provide better performance in this regard. However, the mechanism behind the increased conductivity of nanoscale thin films is still unclear and the reported experimental results are controversial. In the thesis presented here, the effects of mechanical strain and microstructure on the ionic conductivity have been investigated in ultrathin zirconia- and ceria-based thin films.

Reactive RF co-sputtering with metal targets was used to prepare zirconia and ceria based thin films for high purity, modulated composition and thickness. The films were as thin as 10-20 atomic layers thick. X-ray photoelectron spectroscopy, X-ray diffraction and transmission electron microscopy were the main tools to investigate the composition, crystal orientation and microstructure of these sputtered thin films. Microscale interdigitated Pt electrodes were prepared through a lift-off process using photolithography. The electrochemical properties of these sputtered doped zirconia and ceria thin films were investigated using impedance spectroscopy.

YSZ thin films deposited on MgO (111) and, especially, MgO (100) showed highly variable crystal orientations, while MgO (110) offered much more stable

growth. Regardless of whether the growth was epitaxial or highly disordered polycrystalline, 50 nm thick YSZ thin films on MgO (100), (110), and (111) substrates exhibited similar conductivity with YSZ single crystal. While decreasing the thickness further to 12 nm, the conductivities of YSZ thin films were decreased 3 – 7 times. YSZ thin films deposited on Al₂O₃ obtained a stable epitaxial growth along [110] (111)YSZ//[10 $\bar{1}$ 0] (0001)Al₂O₃. By tailoring the thickness of YSZ thin film on Al₂O₃ from 100 nm to 6 nm, the lattice strain can be increased from nearly 1% to 2%. The corresponding conductivity increased by about 1 order of magnitude and the activation energy decreased from 0.99 eV to 0.79 eV.

Ion cleaning of the MgO substrate surface was found to change the YSZ thin films' texture without large change to the conductivity, while ion cleaning of the Al₂O₃ substrate surface decreased the crystallinity without changing the texture and reduced the ionic conductivity of YSZ thin films by a factor of 4. Thus, crystallinity not texture was found to determine the ionic conductivity. In addition, a post annealing with a temperature as high as 1000 °C was able to increase the crystallinity of YSZ thin films therefore increasing the conductivity by a factor of 2.

Gadolinia doped ceria (GDC) thin films deposited on MgO were randomly oriented along multi axes, suggesting a polycrystalline structure. While, on Al₂O₃, GDC thin films' growth became stable only oriented in (111) orientation, just like YSZ thin films on Al₂O₃. In the thickness range of 15 nm – 173 nm, the maximum conductivity of GDC thin films was obtained at the thickness of 81 nm. Interestingly, as GDC thin films' thickness increased above 100 nm, the electrical properties changed from a bulk-like conduction to a grain boundary-like conduction.

Chapter 1

INTRODUCTION

As demand for energy grows, new energy sources and new techniques for converting and storing energy are in high demand. Fuel cells are promising energy conversion devices for their high energy conversion efficiency, because they convert chemical bonds of a variety of fuels directly into electrical energy (and heat) and thereby overcome the combustion efficiency limitation (e.g., the Carnot cycle) [1]. In 1839, the fuel cell was first reported by William Grove, a Welsh physicist, who used dilute sulphuric acid as the electrolyte at room temperature. The first commercial use of fuel cells was realized more than a century later for space flight. Now, fuel cells have been used for laptops, cars, boats, and even residential buildings [2].

Compared with conventional power generation technologies, fuel cells have a lot of advantages. Beside the key feature, the high efficiency mentioned above, fuel cells are silent, environmentally friendly, and produce much less pollution. In addition, fuel cells can be quickly recharged by refueling and operated through modular construction and minimal siting restriction. Although fuel cells exhibit intriguing advantages, they also possess some serious disadvantage. The major barriers are high cost, relatively low power density and fuel availability and storage.

Based on their electrolyte, there are five major types of fuel cells: (1) phosphoric acid fuel cell; (2) polymer electrolyte membrane fuel cell; (3) alkaline fuel cell; (4) molten carbonate fuel cell and (5) solid oxide fuel cell.

1.1 Solid Oxide Fuel Cells

Solid oxide fuel cells (SOFCs) are a fuel cell technology with all solid components. Compared with other fuel cells, the use of solid components induces high stability and abates issues like corrosion and containment. For both economic and environmental concerns, SOFCs are promising. The first solid oxide fuel cell was invented by Baur and Preis in 1937 [3], nearly a century after the invention of the first fuel cell by Grove. Recent developments in SOFCs have achieved a relatively high power density of about $2 \text{ W} \cdot \text{cm}^{-2}$ at $650 \text{ }^\circ\text{C}$ [4]. Newly developed electrolytes with high conductivity may provide an opportunity to further improve the electrical performance of SOFCs at lower temperatures.

The working mechanism of SOFCs is shown in Figure 1. SOFCs consist of two electrodes (the cathode and anode) separated by a solid oxygen ion conducting electrolyte. Air (O_2) flows across the cathode side and fuels flow across the anode side, inducing an oxygen chemical potential gradient. The oxygen chemical potential gradient, which drives oxygen ion conduction from cathode to anode in the electrolyte, creates an electrical potential gradient driven through an external load. Fuel is oxidized in the anode and electrons are released to the external circuit. The electrons flow (from the anode to the cathode) as direct-current electricity. Practical fuel cells are not operated as single unit, instead they are connected using interconnects in the form of a stack in electrical series to build the voltage.

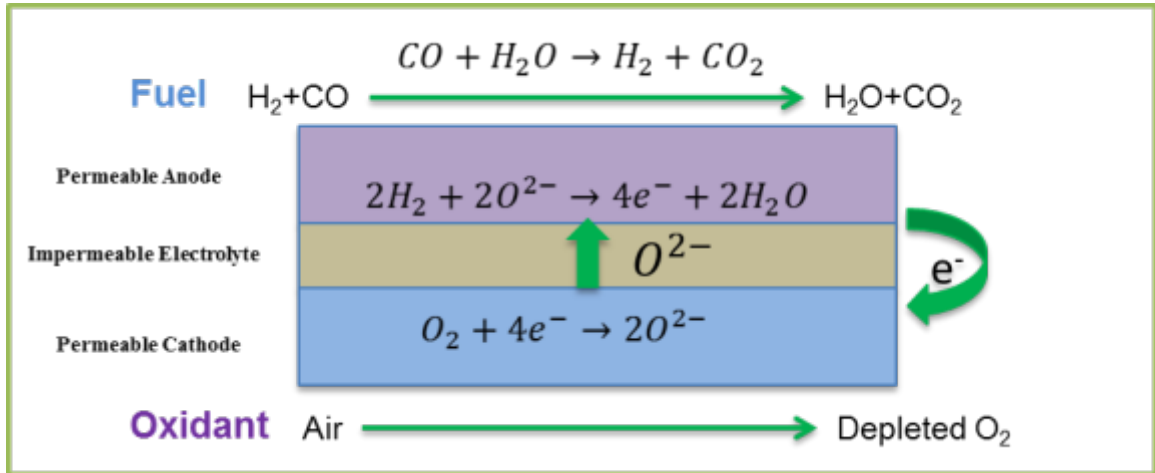


Figure 1 Schematic diagram of a solid oxide fuel cell.

As the electrodes are exposed to different atmospheres as shown above, the anode must be able to withstand the highly reducing environment, while the cathode must be able to withstand the highly oxidizing environment. The most common anode material is a nickel-Yttria stabilized zirconia (Ni-YSZ) cermet. Ni-YSZ has the advantages of high catalytic activity and low cost. Among Ni-YSZ, Ni provides electronic conductivity and catalytic activity while YSZ provides ionic conductivity, thermal expansion compatibility and mechanical stability. The common cathode materials are usually mixed ion and electron conducting ceramic materials, including strontium doped lanthanum manganite, lanthanum-strontium ferrite, lanthanum-strontium cobaltite and lanthanum strontium cobaltite ferrite. In the cathode environment, these materials show good oxidation resistance and high catalytic activity. The common solid electrolyte materials are doped zirconia and ceria, and more details about solid electrolyte will be discussed below.

SOFCs show the advantages of fuel flexibility, non-precious metal catalyst, high quality waste heat for cogeneration application, solid electrolyte and relatively high power density. At the same time, SOFCs' application is limited by the barriers like significant high-temperature materials issues, sealing issues and relatively expensive components/fabrication.

SOFCs typically operate around 1000 °C. One reason for such high operating temperatures is that the traditional electrolyte, sintered ceramic yttria-stabilized zirconia (YSZ), does not offer sufficient thermally activated ion conductance at lower temperatures. The high operating temperature increases the system cost and decreases the economic benefit [2]. The desire to reduce the operating temperature is a key driver of SOFC research. Intermediate temperature (400 °C-700 °C) SOFCs are believed to have a large potential market [2], as they still provide reasonably high efficiency and fuel flexibility while decreasing the system cost associated with high temperature.

1.2 Solid Electrolytes

Solid electrolytes, which conduct electricity by the motion of ions and exhibit negligible electronic transport, include crystalline and amorphous inorganic solids as well as ionically conducting polymers. In SOFCs, solid electrolytes work as an oxygen ion conductor and an electron insulator, so the primary requirements for solid oxide electrolyte materials are high oxygen ion conductivity and low electron conductivity. Faraday [5] first discovered that PbF_2 and Ag_2S were good ion conductors, thereby establishing both the first solid electrolyte and the first intercalation electrode. The dawn of the twentieth century saw the first technological application of ion transport in solids, when Nernst [6] (1890) proposed a new form of

electric light. He described how ZrO_2 when doped with a small amount of Y_2O_3 would emit a bright white light on the passage of a current at high temperature, due to its ability to conduct oxide ions.

Development of electrolyte materials that possess high oxygen ion conductivity at relatively low temperature is essential for the increased commercialization of electrochemical devices including fuel cells, gas sensors, and ionic membranes [1, 2]. In addition to the conductivity requirements, electrolytes in SOFCs are exposed to both the oxidizing cathode and reducing anode environment, so they must also be chemically and mechanically stable at high temperatures in both environments. For this application, the solid electrolyte must be fabricated to be non-porous to separate the fuel and oxidant. The solid electrolytes formed using powder processing routes usually must be densified at elevated temperature. A high fracture resistance and related mechanical properties are also desirable for solid electrolytes, since fracture during fabrication or service is fatal for normal operation. Finally, thermal compatibility is very important. Similar thermal expansion between the solid electrolyte and the cathode and anode decrease the possibility of fracture due to thermomechanical stress.

In an oxygen ion conductor, the conductivity is expressed as:

$$\sigma = nq\mu \quad (1)$$

where n is the effective oxygen vacancy concentration; q is the effective charge of the oxygen ion; and μ is the mobility of the oxygen ion. In addition,

$$n = n_0 \exp\left(-\frac{\Delta G_A}{kT}\right) \quad (2)$$

$$\mu = \frac{qD}{kT} \quad (3)$$

where n_0 is the total oxygen vacancy concentration and ΔG_A is the energy of dopant-vacancy association; D is the diffusion coefficient of the oxygen ion and $D = D_0 \exp(-\frac{\Delta G_m}{kT})$, where D_0 is the primary mobility of the oxygen ion and ΔG_m is the energy of vacancy migration. Then

$$\sigma = \frac{A}{T} \exp\left(-\frac{\Delta G_A + \Delta G_m}{kT}\right) \quad (4)$$

where $A = \frac{n_0 D_0 q^2}{k}$. In order to increase the conductivity, the ways to increase n_0 or D_0 or to decrease ΔG_A or ΔG_m are needed. Independently varying these parameters can be difficult. For example, in doped zirconia, increasing the dopant concentration will generally increase n_0 and ΔG_A at the same time.

1.3 Zirconia- and Ceria-based Solid Oxide Electrolytes

Zirconia-based materials are the most common solid oxide electrolytes used in commercial applications. Pure zirconia is not a good electrolyte, as it suffers from very low ionic conductivity. As shown in Figure 2, ZrO_2 shows a monoclinic crystal structure at room temperature, changing to a tetragonal phase at 1170 °C and a cubic fluorite phase at 2370 °C. Doping with various aliovalent oxides stabilizes the cubic fluorite structure to room temperature. In addition, the doping increases the oxygen vacancy concentration thereby increasing the ionic conductivity. The most commonly used dopants are Y_2O_3 , CaO , Sc_2O_3 and some rare earth oxides.

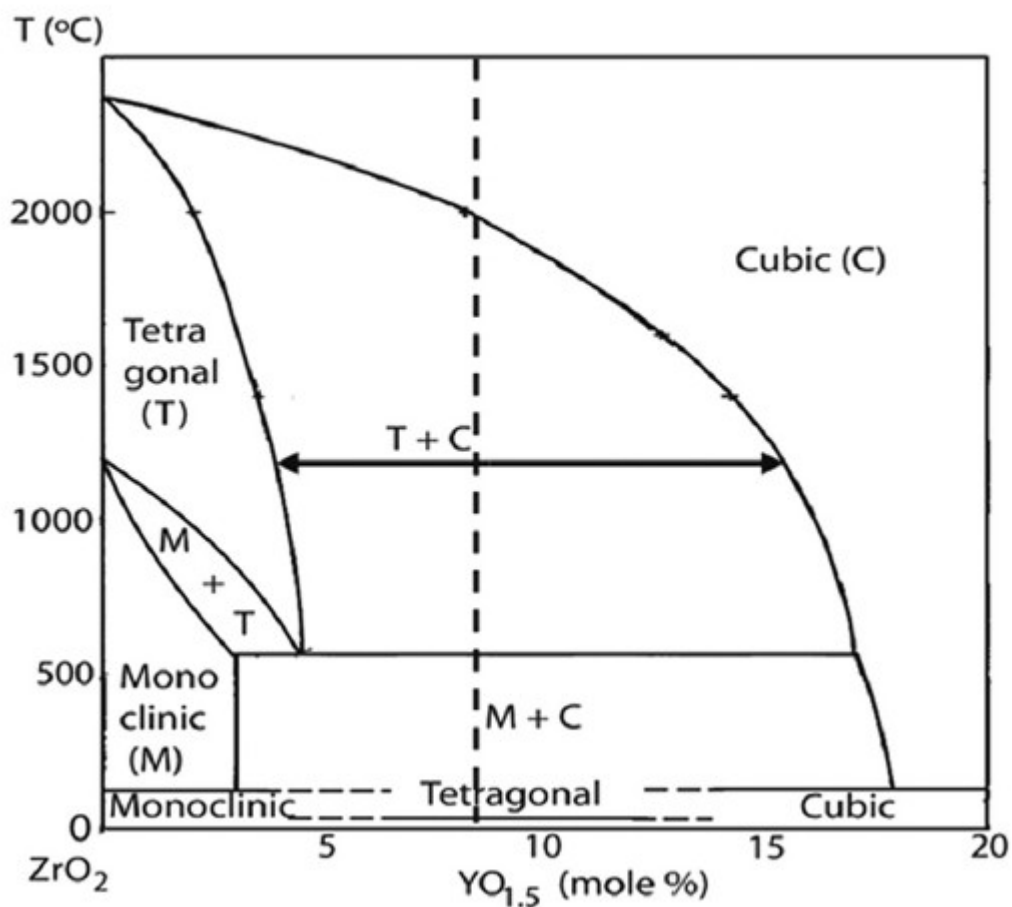


Figure 2 The phase diagram of YSZ. Reprinted with permission from reference [7].

YSZ, the yttria-doped version of these materials, has the advantages of moderately high ionic conductivity, low electron conductivity, low cost and high chemical stability. In addition to its use in SOFCs, YSZ has been widely used or researched for a number of other applications, including thermal barrier coatings, high-K dielectrics, optical coatings, and oxygen sensors.

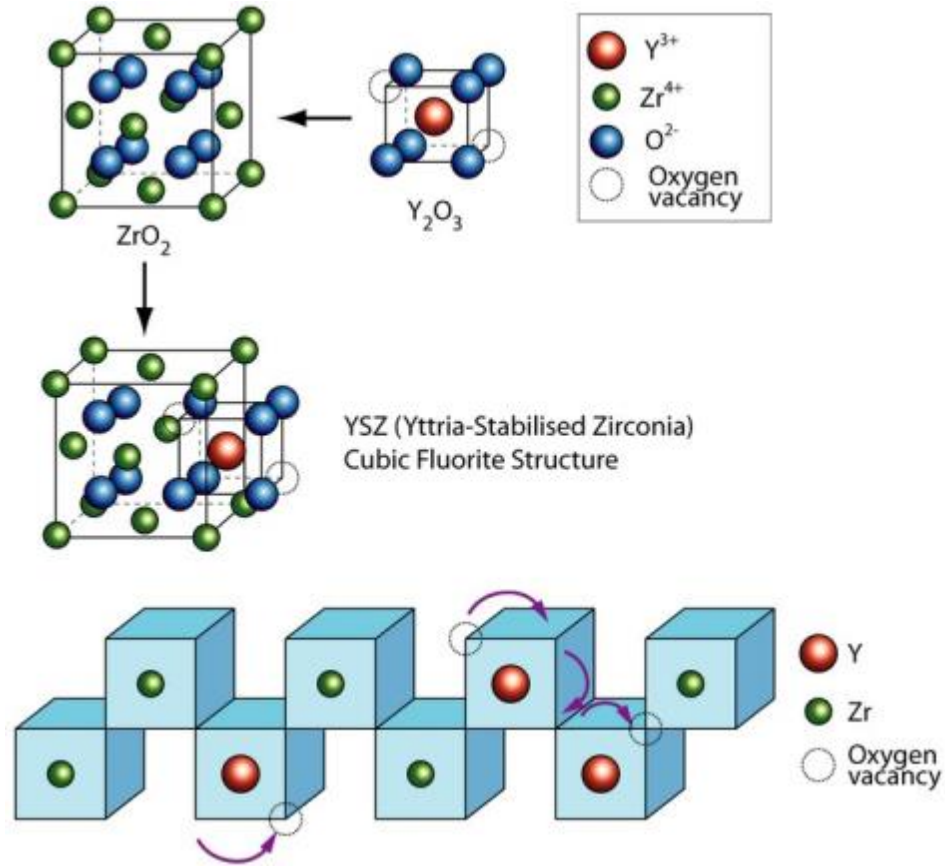
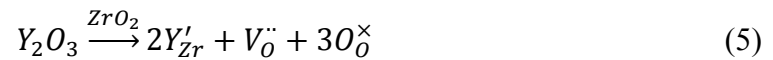


Figure 3 The doping and vacancy transport in YSZ. Reprinted from reference [8].

As shown in Figure 3, oxygen ion conduction through solid electrolytes like YSZ occurs via a vacancy mechanism. Typical oxygen ion conductors are doped materials in which dopants create a high concentration of mobile oxygen vacancy point defects. For example, in YSZ, yttrium dopants sit substitutionally on the zirconium lattice sites according to the defect chemical reaction:



where Y'_{Zr} represents a yttrium sitting substitutionally on a zirconium site with a net charge of -1 and $V_{O}^{\bullet\bullet}$ represents an oxygen vacancy with a net charge of +2. The doping

of one part yttria will induce one part oxygen vacancy, so increasing the dopant concentration will linearly increase the oxygen vacancy concentration.

As shown in Figure 4, at low levels of dopant concentration, the conductivity of YSZ increases with increasing dopant concentration. However, above a certain dopant concentration, the conductivity of YSZ decreases with increasing dopant concentration. The decreased conductivity at higher dopant concentration is believed to be due to defect ordering [1] within dopant-vacancy clusters, which increases the association energy (ΔG_A) in equation 4. The maximum conductivity is generally found at the minimum dopant concentration that is sufficient to stabilize the cubic phase of zirconia.

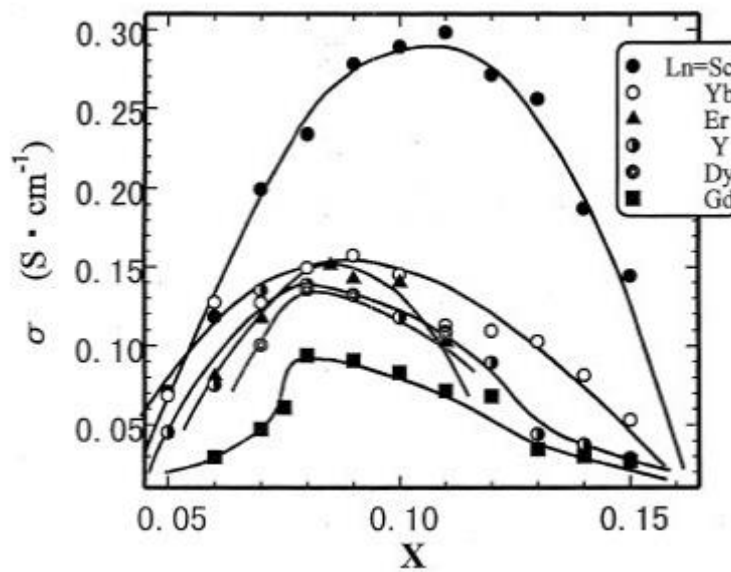


Figure 4 Composition dependence of the electrical conductivity at 1000 °C for $(\text{ZrO}_2)_{1-x}(\text{Ln}_2\text{O}_3)_x$. Reprinted with permission from reference [9].

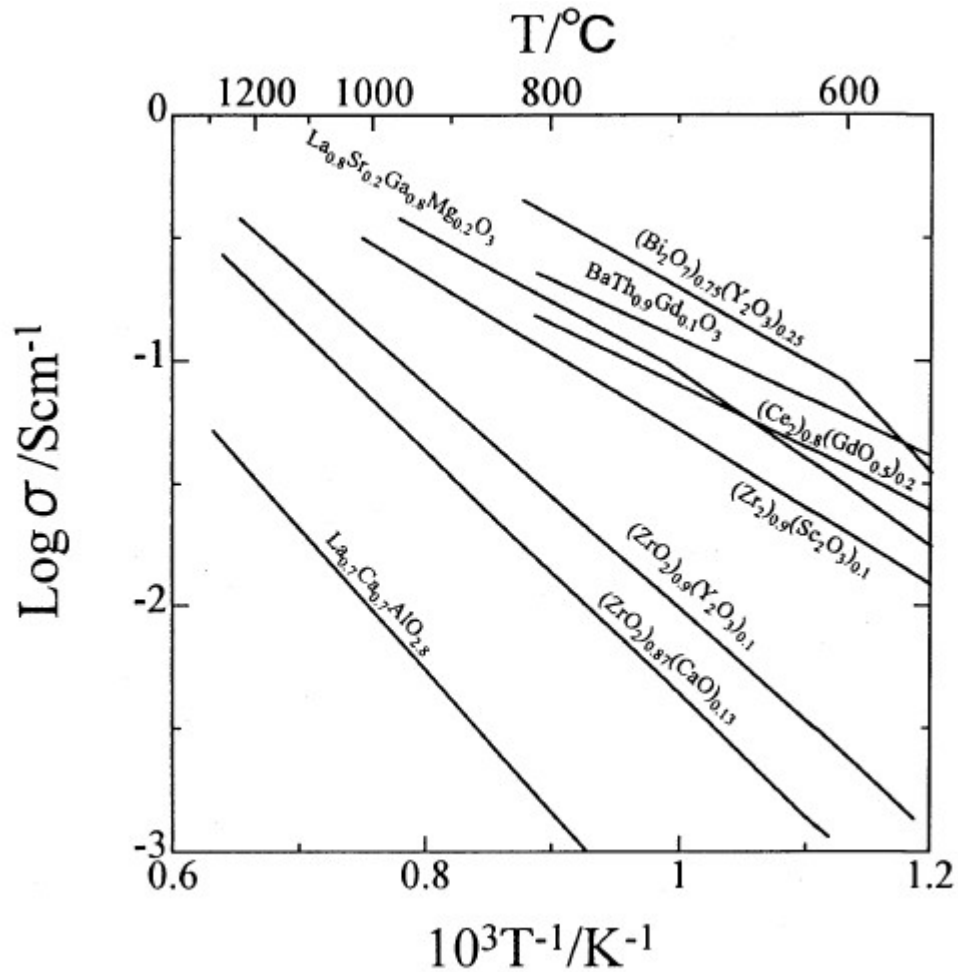


Figure 5 Temperature dependence of electrical conductivity for oxide ion conductor. Reprinted with permission from reference[10].

Doped ceria is also good solid electrolyte material [1, 10]. Unlike zirconia, both undoped and doped ceria have the fluorite cubic crystal structure. The most commonly used dopants in ceria are Gd_2O_3 , Sc_2O_3 , Y_2O_3 , CaO and some rare earth oxide. As shown in Figure 5, compared with doped zirconia, doped ceria shows a higher conductivity, which makes doped ceria a promising solid electrolyte candidate.

However, doped ceria also shows less chemical stability, which may undergo departures from stoichiometry especially in a reducing environment and exhibit significant electronic conductivity. In order to be a useful solid electrolyte, the electronic conductivity of doped ceria must be minimized under reducing environments.

1.4 Zirconia-based Thin Films

For the application in SOFCs, the main concern of zirconia based electrolytes including YSZ is insufficient oxygen ion conductivity at intermediate temperatures. However, compared with conventionally fabricated (“bulk”) materials, thin films may exhibit vastly different properties, including microstructure, stoichiometry and strain state. In addition, heterogeneous chemistry exists at the film-substrate and film-air interfaces. All of these factors may lead to altered local defect concentration or mobility, and thereby altered ionic conductivity. So the fabrication of thin films—especially nanoscale thin films—has been a promising way to increase its conductance at intermediate temperatures. YSZ thin films have been studied as model solid state electrochemical systems [11-15] as well as for possible use within fuel cells [16-19].

A number of techniques have been reported for the production of YSZ films, including sol-gel methods using dip coating and spin coating [20, 21]; powder methods such as electrophoresis and spraying [22]; and physical vapor deposition methods, including evaporation [23, 24], sputtering [11, 25, 26], and pulsed laser deposition (PLD) [27, 28]. These methods for the production of YSZ thin films were reviewed previously [29].

For YSZ bulk, the conductivity values reported by different groups are quite similar. Figure 6 plots the conductivities of polycrystalline and single crystal bulk

YSZ samples measured in a number of the same reports for calibration of the thin film results. As can be seen, the bulk samples fall within a very narrow range of values, as expected for the chemically stable and relatively impurity-insensitive YSZ. From Figure 6, YSZ bulk samples were found to exhibit conductivities all within 3×10^{-4} S/cm and 10^{-3} S/cm at 500 °C. In addition, the activation energies ranged within 1.02 eV and 1.23 eV in the presented temperature range. The relatively good repeatability among the bulk samples comes despite differences in preparation method, dopant content, and, likely, purity.

Table 1.

Literature review on bulk YSZ with respect to their microstructure and dopant concentration, as shown in Figure 6.

No.	Sample	dopant concentration	Ref.
1	polycrystalline	8.7%	[30]
2	polycrystalline	8%	[31]
3	single crystal	10%	[23]
4	single crystal	8%	[32]
5	polycrystalline	8%	[33]
6	polycrystalline	not reported	[34]
7	bulk grain	8%	[35]
8	bulk	8%	[36]
9	polycrystalline	8%	[37]

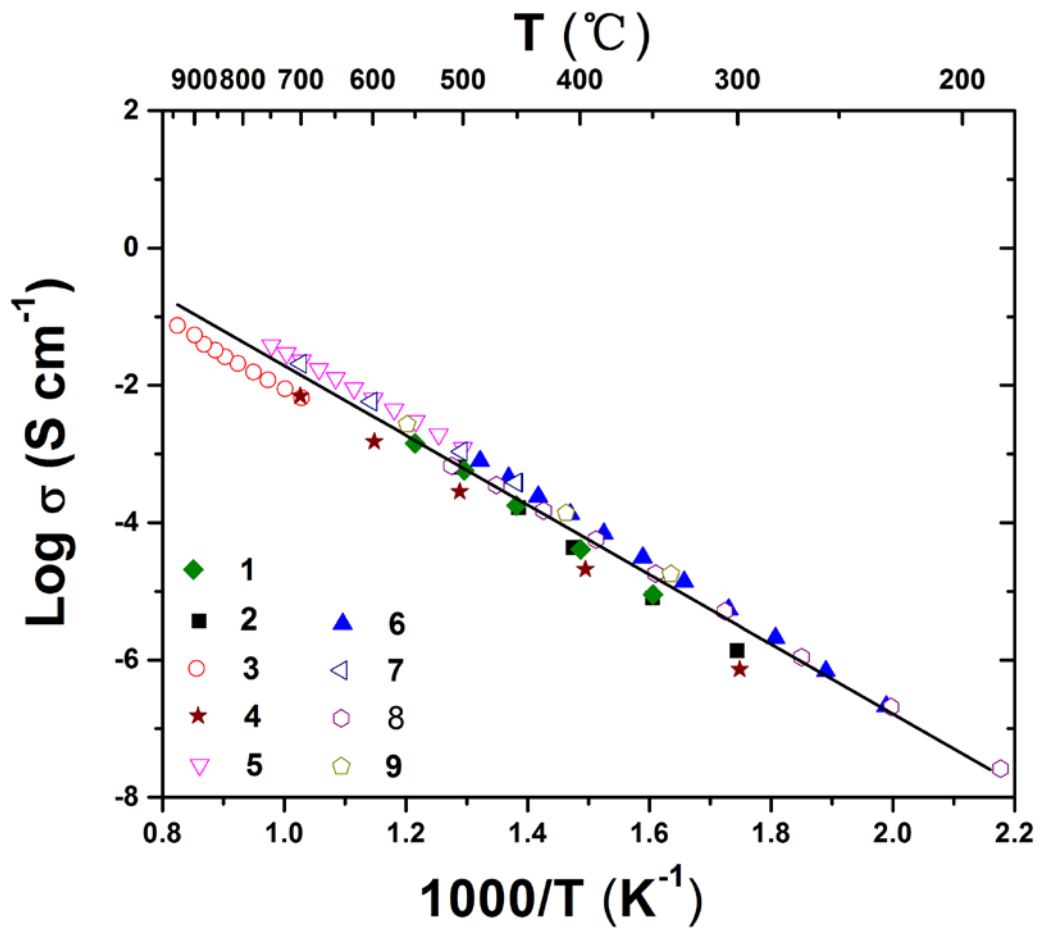


Figure 6 Arrhenius plots of the electrical conductivities of YSZ bulk samples (both single crystal and polycrystalline) taken from a number of literature sources (data references are listed in Table 1). In the plot, the line represents typical values reported for bulk YSZ, calculated as a linear regression of all of the data presented in the plot. Reprinted from reference [38].

Recent studies have reported YSZ films with thicknesses ranging from a few microns to a few nanometers. As the thickness decreases, as shown in Figure 7, YSZ

thin films show an altered conductivity compared with YSZ bulk (both single crystal and polycrystalline) [23, 32, 39-42].

The ionic conductivity increases reported in nanoscale YSZ thin films remain controversial, as the reports have been difficult to repeat. A number of experimental difficulties burden these measurements, including accurate measurement of the conductivity of relatively resistive thin films. In a highly revealing and informative paper, Kim et al. [43] found that the current flowing through myriad conduction paths parallel to the thin films may increase the apparent conductivity of ultra-thin single layer YSZ by at least one order of magnitude, especially when the conductivity is measured in an in-plane configuration using electrodes spaced far apart (i.e., when the expected resistance of the film is high). Leakage resistances were found to be as low as 150 k Ω at 600 °C. The resistance of a film structure with a thickness of just a few nanometers and inter-electrode spacing of a few millimeters may approach or exceed this value, leading to incorrectly reported, anomalously low “film” resistances. Measurement of a sample blank is recommended in order to compare the resistance with that of samples that are identical save the inclusion of a film. Such a comparison was reported in a few of the studies, and Kim et al. show that taking a few precautions indeed allows the accurate determination of the conductivity of 40 nm thick (and presumably thinner) YSZ films.

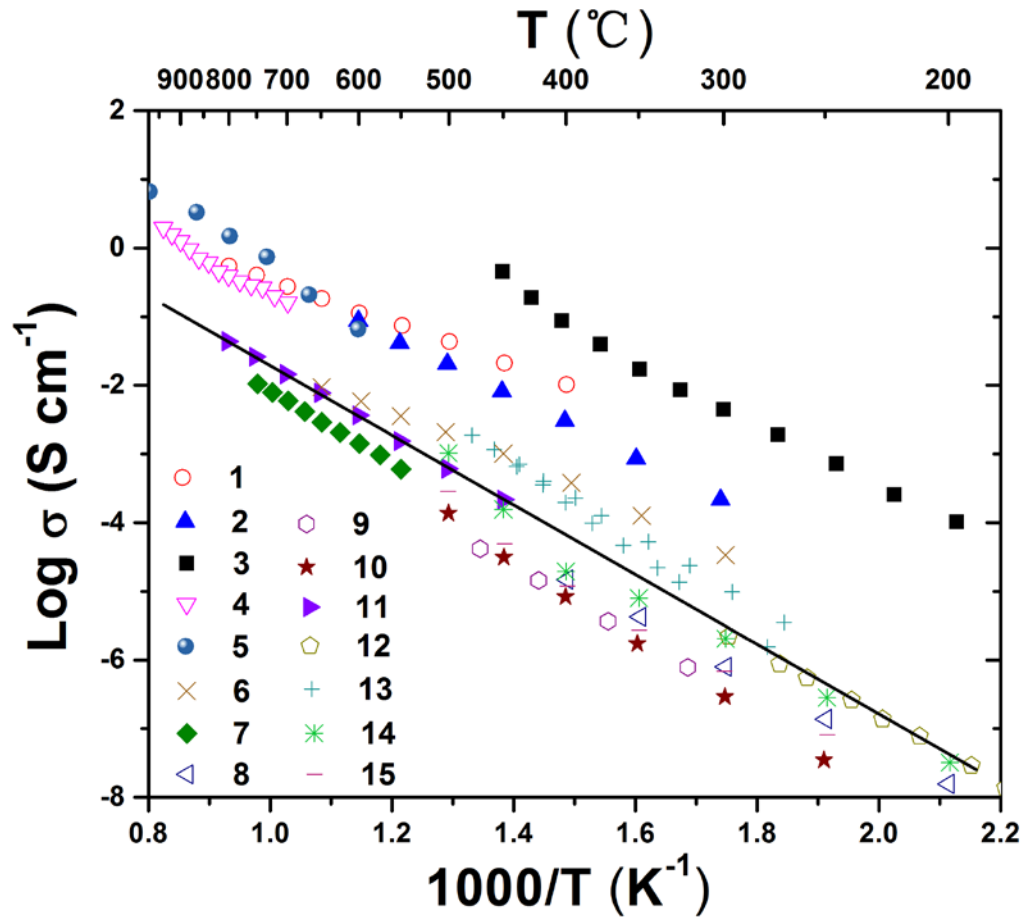


Figure 7 Arrhenius plots of the electrical conductivities of YSZ thin films taken from a number of literature sources (data references are listed in Table 2). In the plot, the line represents typical values reported for bulk YSZ, calculated as a linear regression of all of the data presented in Figure 6. Reprinted from reference [38].

Table 2

Literature review on YSZ thin films with respect to their dopant concentration, substrate, processing method and thickness, as shown in Figure 7. Note: the data is ordered in the manner in which each reference is discussed in detail below.

No.	dopant percentage	substrate	processing method	Ref.	film thickness(nm)
1	9.5%	MgO (001)	PLD	[42]	15*, 29, 58-2000
2	8.7%	Al ₂ O ₃	spin coating	[30]	400-700*
3	8.7%	MgO (110), MgO (111)	sputtering	[31]	58*, 107, 194
4	9.5%	MgO (100)	electron beam evaporation	[23]	17*, 35, 70, 210
5	8%	Si (100)	sol-gel	[21]	580*
6	9%	Al ₂ O ₃ (0001)	sputtering	[32]	6*, 12, 50, 100
7	8%	MgO (100)	PLD	[33]	12*, 25
8	8%	Si (100)	PLD	[34]	20*, 55, 90
9	8%	Si (100)	PLD	[44]	20, 55, 90*
10	8%	Al ₂ O ₃	PLD	[44]	105*
11	8%	Al ₂ O ₃ (0001)	PLD	[35]	600-1500*
12	8%	MgO (100)	sputtering	[36]	500-800*
13	9.1%	SiO ₂	sputtering	[12]	1000*
14	8%	Al ₂ O ₃ (0001)	PLD	[37]	28*, 250
15	8%	MgO (100)	PLD	[37]	65*

The symbol “*” denotes the film that was reported to have the maximum deviation in conductivity from expected values and was thus chosen to be presented in Figure 7.

Here, I categorize the reports based on increased conductivity, decreased conductivity or unaltered conductivity relative to bulk YSZ.

1.4.1 Increased Conductivities with Nanoscale Thin Films

Kosacki et al.[42, 45] reported in-plane ionic conductivity as a function of film thickness for films that ranged from 15 nm to 2 μm for YSZ films with (001) texture grown epitaxially on MgO (001) substrates via PLD at 500 °C. The in-plane conductivity was measured by two-probe impedance using silver electrodes. A 1 - 2 orders of magnitude increase in the conductivity was observed for films less than 60 nm thick, with a maximum conductivity at 800 °C of 0.6 S/cm observed for a 15 nm thick film. The author concluded that parallel paths for ion conduction existed from a YSZ bulk path and a YSZ/substrate interfacial path. In later work [30], the authors also prepared 8.7 mol% nanocrystalline YSZ thin films in the thickness range of 0.4

μm - $0.7 \mu\text{m}$ on Al_2O_3 substrates using a polymer precursor spin coating technique. The conductivity of nanocrystalline YSZ thin films was about one order of magnitude higher compared with bulk polycrystalline YSZ.

Sillassen et al. [31] (see also [40]) prepared 8.7 mol% YSZ thin films by reactive DC magnetron sputtering with thickness varied from 58 nm to 420 nm using MgO (110), SrTiO_3 (STO) (100), and MgO (111) substrates with a deposition temperature of $800 \text{ }^\circ\text{C}$. Pole figures were used to demonstrate epitaxial growth of YSZ (220) on MgO (110), YSZ (200) on STO (100), and YSZ (111) on MgO (111), however epitaxy was lost for films deposited on MgO when above an orientation-dependent critical thickness. The in-plane conductivity was measured using a four-terminal configuration with Ag paste electrodes. A greater than three order of magnitude increase in the lateral ionic conductivity of epitaxial YSZ films relative to bulk ceramics was reported. A superposition of two parallel contributions was suggested: one due to the bulk and one attributable to the film-substrate interface. At temperatures below $\approx 350 \text{ }^\circ\text{C}$, the contribution from the film-substrate interface dominated with a decrease in activation energy, whereas at higher temperatures a more “bulk-like” conductivity was observed with activation energies close to the activation energy for bulk YSZ ceramic. The strain model proposed by Schichtel et al. [41] was used to explain the increase in conductivity for the films deposited on STO. The high density of misfit dislocations at the semicoherent interface was believed to have led to even larger conductivity increases in the YSZ/MgO system.

Karthikeyan et al. [23] prepared 9.5 mol% YSZ thin films with thickness range from 17 nm to 210 nm on MgO (100) substrates by electron beam evaporation. Despite the relatively high dopant levels, the films were found to be a mixture of

cubic and tetragonal phases. The in-plane conductivity was measured by two-probe impedance using platinum electrodes. As with the reports discussed above, the conductivity of the films increased with decreasing film thickness. The increases in conductivity were attributed to space charge effects at the film-substrate interface and at the grain boundaries. As evidence, the authors noted a high activation energy for the conductivity relaxation time as determined by impedance measurements. The increased conductivity was also observed in samples deposited on Al_2O_3 and suggested that it was not primarily an effect specific to one particular kind of substrate. In later work, Karthikeyan et al. [46] reported microstructural studies carried out on YSZ thin films grown on MgO (100) and Ge (100) single crystal substrates using in-situ transmission electron microscopy. A one order of magnitude increase in total conductivity was reported for films less than 20 nm thick grown on an MgO substrate. For 17 nm films, the authors again noted an increased activation energy of the electrical relaxation time of 1.7 eV. This activation energy was ~ 1.1 eV for 933 nm thick films, comparable to bulk YSZ. Similar to the previous reports, increasing conductivity with decreasing film thickness gave evidence of enhanced interfacial conductivity.

Zhang et al. [21] fabricated dense, crack-free, and homogeneous $(\text{RE}_2\text{O}_3)_{0.08}(\text{ZrO}_2)_{0.92}$ (RE= Sc, Y) nanocrystalline thin films on Si (100) substrates using a sol-gel method. At temperatures above 600 °C, the electrical conductivity of $(\text{Sc}_2\text{O}_3)_{0.08}(\text{ZrO}_2)_{0.92}$ and $(\text{Y}_2\text{O}_3)_{0.08}(\text{ZrO}_2)_{0.92}$ nanocrystalline thin films in pure cubic phase was found to be one order of magnitude higher compared with that of the corresponding bulk materials. The in-plane conductivity was measured by two-probe impedance using platinum electrodes. The authors attributed the conductivity increase

to reductions in the grain boundary resistance; this was related to nanometric grain sizes causing increased grain boundary purity (as previously demonstrated in traditionally processed YSZ by Aoki et al. [47]).

1.4.2 Decreased Conductivities with Nanoscale Thin Films

Guo et al. [33] deposited polycrystalline 8 mol% YSZ thin films by PLD with thicknesses of 12 nm and 25 nm on MgO (100) substrates and measured the conductivity in dry and humid O₂. Impedance spectra were measured with platinum electrodes. The ionic conductivity of the nanostructured films was lower by about a factor of 4 compared with microcrystalline bulk ceramics. The authors attributed this decrease to lower bulk and grain-boundary conductivities, and thus the influence of the ZrO₂/MgO interface on ionic conduction was considered to be negligible. The authors further concluded that proton conduction was insignificant in the nanostructured films, even when measured in a humidified environment.

Navickas et al. [34] prepared 8 mol% YSZ thin films of 20 nm, 55 nm, and 90 nm thickness by PLD onto Si (100) substrates with a native silica layer. The across-plane conductivity was measured with circular gold electrodes. The conductivity of the YSZ films did not significantly depend on the layer thickness and was 3-4 times lower than a YSZ polycrystalline sample. In addition, Navickas et al. [44] suggested that the blocking effect of a native silica interlayer on a Si substrate allowed anisotropy studies of ion conduction in thin films and that simultaneous in- and across-plane conductivity measurements on YSZ layers in a single impedance spectrum were possible in a limited temperature range. It was found that the across-plane conductivity of YSZ thin films was similar to the bulk values of a macroscopic polycrystalline sample and approximately one order of magnitude higher than the in-

plane values. The activation energy of across-plane ionic conductivity (~ 0.8 eV) was lower than that of in-plane conduction (~ 1 eV). These results were attributed to the large number of grain boundaries surrounding columnar grains impeding the in-plane (but not across-plane) ion transport.

1.4.3 Unaltered Conductivities with Nanoscale Thin Films

Joo et al. [35] deposited YSZ thin films with thickness ranging between 0.6 μm and 1.5 μm on Pt (111), Pt (200) and Al_2O_3 (0001) using PLD. The conductivity was measured using both impedance and two-probe DC methods using platinum electrodes. The across-plane and in-plane conductivity values of the films were similar. In addition, the ionic conductivity and activation energy of the films were similar to those of bulk YSZ. Similar conductivities were found regardless of thickness (including both film and bulk samples) and mode of measurement (in-plane or across-plane conductivity).

Rivera et al. [36] grew textured YSZ thin films with thickness in the range 500 nm – 800 nm on MgO (100) by RF sputtering at 650 °C. Films were strongly oriented along the YSZ (200) direction, but with additional YSZ (111) peaks visible. The confirmed column-like structure had no grain boundaries perpendicular to the growth direction. Admittance spectroscopy was measured with gold electrodes. The DC across-plane conductivity in the thin films was found to be highly similar to a bulk sample.

Jung et al. [12] focused on the ability of nanometric grain sizes to stabilize the cubic fluorite phase at reduced yttria concentration. Using sputtering onto unheated fused silica substrates, 1 μm thick polycrystalline films were deposited. Impedance

spectra were measured with interdigitated platinum electrodes. Conductivity for a 9.1 mol% YSZ film was similar (though perhaps slightly larger than) bulk samples.

Gerstl et al. [37] prepared 8 mol% YSZ thin films with thicknesses of 65 nm on MgO (100) and 28 nm and 250 nm on Al₂O₃ (0001) using PLD at 500 °C – 650 °C. The film on MgO was further annealed for 16 hours at 1000 °C. Impedance spectra were measured with interdigitated Au/Cr electrodes. The bulk conductivity of all three samples were found to be close to that of the macroscopic YSZ polycrystal and the activation energy was around 1 eV, matching reference measurements.

Based on the above literatures, the factors, such as thickness, substrate, microstructure and strain are likely to affect the electrical properties of YSZ thin films. Below, these factors are discussed one by one.

1.4.4 Effect of Thickness on Conductivity

Since the interfaces with the substrate and the surrounding environment are the defining features that separate thin film and bulk samples, the relative portion of the volume that is in proximity to the interfaces—in other words, the film thickness—may be of key importance. The decreasing thickness may induce different microstructure, phase, stress state, stoichiometry, lattice parameter, or other feature correlated to the conductivity. Indeed, most of the reports that found increased conductivity in YSZ films also found that the conductivity increased as the film thickness decreased. Karthikeyan and Kosacki found that conductivity increased when the thickness was below 210 nm and 58 nm, respectively. Taking all references into account, increased (or decreased) conductivity is generally found when the film thickness is below about 500 nm.

Figure 8 plots the conductivities reported at 500 °C of YSZ films as a function of film thickness. At 500 °C, bulk YSZ is consistently reported to have a conductivity of around 10^{-3} S/cm. For film thicknesses below 1 μm , and especially below 100 nm, reported conductivity values range over four orders of magnitude, from 10^{-4} S/cm to nearly 1 S/cm. A bias towards the reporting of conductivity values that are increased and not decreased from bulk values may be expected. In spite of this, no clear correlation can be directly found between conductivity values and thickness except that the variability clearly increases as thickness decreases. Though thickness measurements become increasingly difficult—and therefore may be more uncertain—as a film becomes thinner, the variability in reported conductivity values greatly exceeds any expected film thickness measurement uncertainty.

Kim et al. [43] show that leakage current parallel to the films under test can lead to an illusionary effect where the conductivity seems to increase with decreasing thickness. Since the same parallel resistance is divided by decreasing film thickness, an inverse relationship between conductivity and film thickness might be expected in these cases; a slope of -1 should be found in log-log plots of conductivity vs. film thickness. Interestingly, the inset of Figure 8 indicates slopes that are smaller (more negative) than this value.

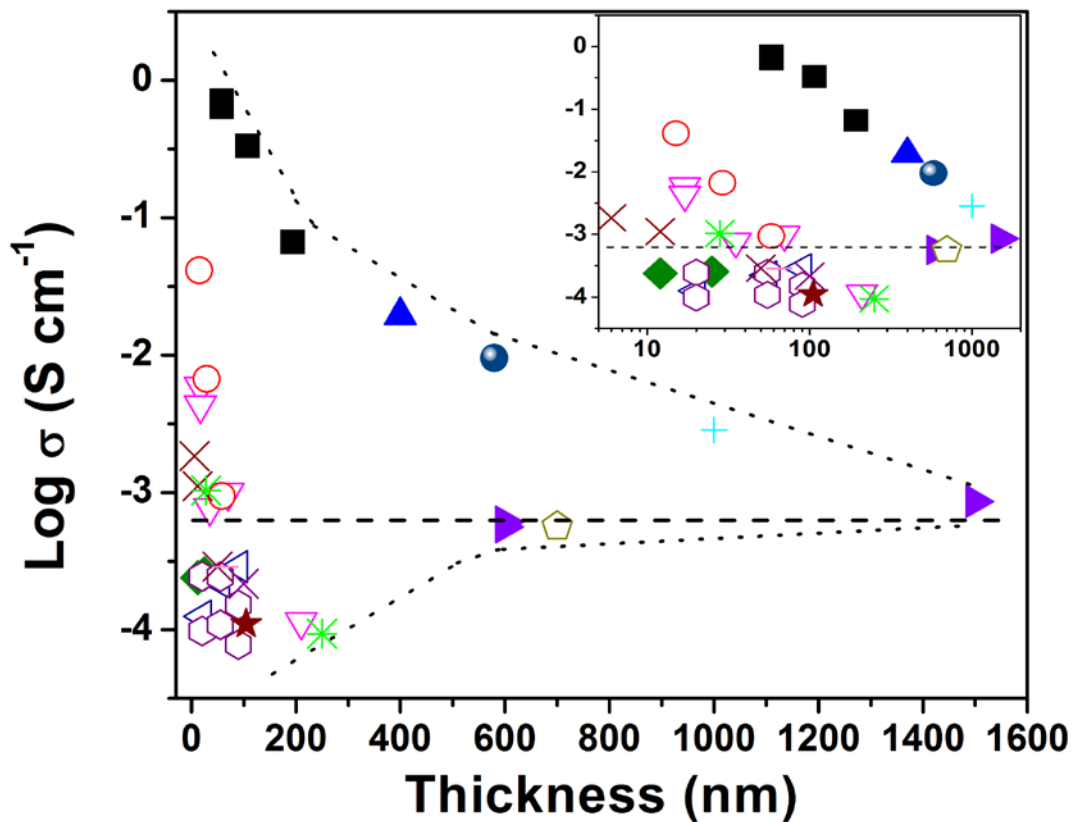


Figure 8 The values reported for electrical conductivities at 500 °C of YSZ thin films as a function of their thickness indicate a positive correlation between film thickness and experimental repeatability. The inset presents the same information in a double log scale. The symbols represent data from the same references as indicated in Figure 7. Unlike Figure 7, plotted here are the data from all films reported in these references, not just the films that maximally deviate from the expected value. Note that some values are interpolated or extrapolated from original data to 500 °C. The black dashed line represents an average conductivity of bulk YSZ at 500 °C. Dotted lines are guides for the eye. Reprinted from reference [38].

1.4.5 Effect of Substrate on Conductivity

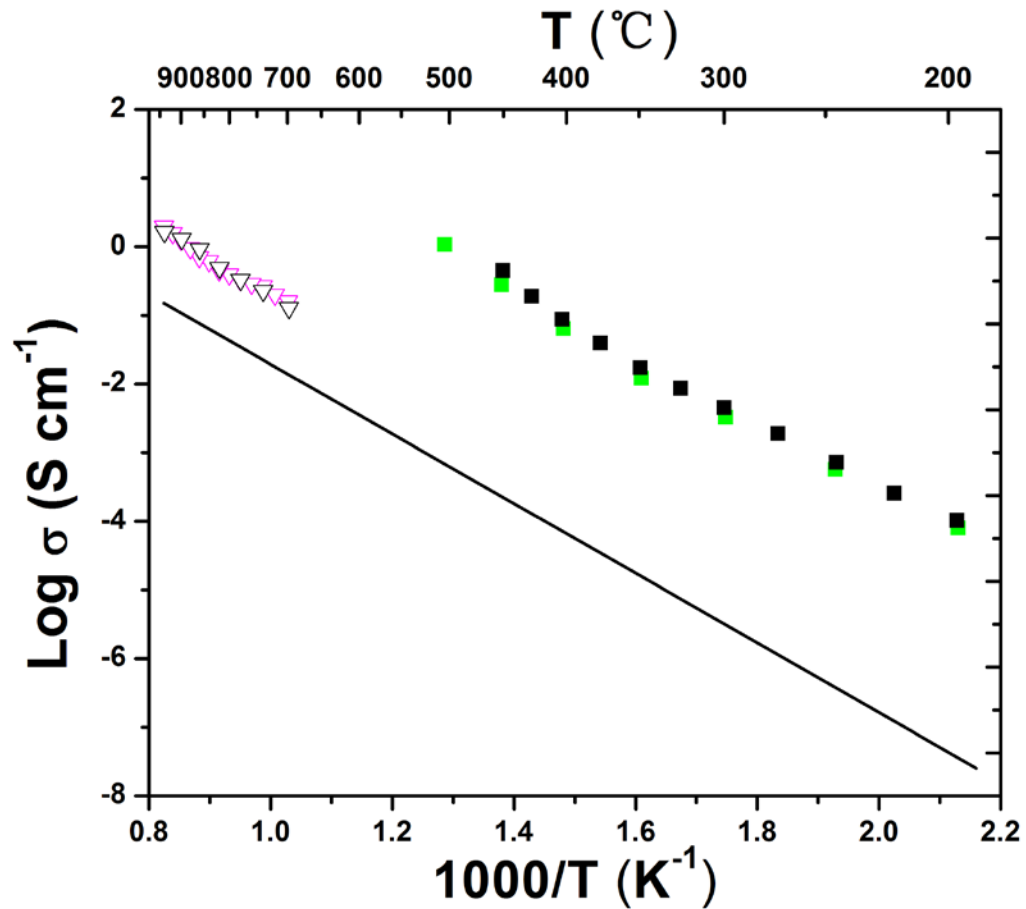


Figure 9 Arrhenius plots of electrical conductivities of YSZ thin films with similar thickness grown on substrates of MgO or Al_2O_3 . The symbols represent the same data as indicated in Figure 7. Reprinted from reference [38].

If the substrate-film interface determines the film's properties, then the substrate composition, crystal structure, and orientation may be expected to play a role. The data presented in Figure 7 included reports using a number of different substrates, including MgO, Al_2O_3 , Si, and SiO_2 . No clear effect of substrate can be found. Several groups have directly measured films deposited identically (including thickness) except

for the substrate, and these data are presented in Figure 9. Karthikayan et al. [23] deposited 17 nm YSZ on MgO and Al₂O₃ and Sillassen et al. [31] prepared 58 nm YSZ on MgO with (110) and (111) orientations. In both cases, the conductivities were quite close no matter the substrate. Based on these reports, the effect of the substrate on the YSZ film conductivity seems surprisingly negligible and other causes seem to be inducing the increased conduction. Obtaining the same result despite changing the substrate composition also suggests that leakage current through the substrate is not significant, though other sources of leakage current remain possible [43].

In addition, if ion cleaning is performed within moderate vacuum soon on the substrate surface before deposition, it is intended to enable presentation of a chemically pristine surface to the initial film deposition. Specifically, the surface can be free from adventitious carbon, moisture, and resilient inorganic contaminants. Structurally, ion cleaning might create different surface morphology and roughness [48]; chemically, ion cleaning might clean the surface of impurities and/or adjust the surface stoichiometry, in particular by creating oxygen deficiency [49]. Ion cleaning may also introduce atomic surface damage, compressive stresses, or amorphization through shot peening [50]. These differences in surface structure and chemistry are believed to influence the microstructure and electrical properties of the YSZ thin films.

1.4.6 Effect of Microstructure on Conductivity

Depending on the deposition conditions, thin films can be polycrystalline or epitaxial and thus free of grain boundary blocking effects. In addition, epitaxial thin films can exhibit different crystallographic texturing. This effect is usually attributed to lattice mismatch and free surface energy minimizations. As an example of the different microstructures that can be created, Guo et al. [33] obtained polycrystalline

YSZ thin films via PLD at a substrate temperature of 700 °C, while Kosacki [42] et al. achieved epitaxial YSZ thin films in the [100] direction by PLD on MgO (100).

The blocking effect of grain boundaries is well established in doped zirconia. Even in the absence of impurity phases, the grain boundary resistivity can be two or three orders of magnitude higher than the bulk resistivity [51]. This fact suggests that polycrystalline thin films, which typically exhibit nanometric grain sizes and thus a large number of grain boundaries between laterally separated electrodes, are likely to exhibit reduced conduction relative to conventionally fabricated samples. Accordingly, Navickas et al. [44] found that the across-plane conductivity of YSZ thin films was approximately one order of magnitude higher than the in-plane values. The activation energy of across-plane conduction (≈ 0.8 eV) was also lower than that of in-plane conduction (≈ 1 eV). The films were deposited by PLD and had a columnar grain structure. Thus, the difference between the across-plane and in-plane conduction behavior was attributed to the effect of grain boundaries partially blocking the in-plane ion transport.

Other studies cannot so clearly link grain boundary resistance to noted changes in overall conductivity. Kosacki et al. [30] prepared 8.7 mol% nanocrystalline YSZ thin films in the thickness range of 0.4 μm - 0.7 μm on Al_2O_3 substrates. The conductivity of the nanocrystalline YSZ thin films was about one order of magnitude higher compared with bulk polycrystalline YSZ. Still, the conductivity of nanocrystalline YSZ thin films with a thickness around 0.4 μm - 0.7 μm was higher than that of 29 nm thick YSZ thin film with epitaxial growth on MgO (001) reported by the same group [42].

1.4.7 Effect of Strain on Conductivity

Lattice strain is a suspected means to improve ion conduction in solid electrolytes, including in YSZ. At the same time, very high residual stresses are known to exist in thin films, especially polycrystalline films [52], and YSZ films in particular [53]. The stresses can arise from thermal expansion mismatch with the substrate, lattice parameter mismatch at coherent interfaces, ion bombardment during deposition, grain coalescence, impurity removal during thermal treatment, recrystallization, and other causes. Despite this, residual stress remains underreported in the literature. It can be difficult to control the residual stress in a film, and the biaxial stress state of a thin film may in fact change enormously with differing process parameters or during the course of a seemingly innocuous thermal treatment. For example, a 1 μm thick YSZ film sputter deposited onto an unheated fused silica substrate was measured to have around 0.5 GPa of compressive residual stress. After heating the film to 450 $^{\circ}\text{C}$ and cooling back to room temperature, the film was measured to have around 0.3 GPa of tensile residual stress [12]. Similar effects were noted in films deposited on Si substrates [53]. With such difficulty in controlling film stress, it is difficult to test the role of stress on ion conductivity in YSZ films in a systematic manner (a notable exception is to be found in Reference [41] and other works from this group).

Further, Rupp [54] reported on the importance of lattice strain to ionic conduction in metal oxide thin films. It was suggested that different thin film processing methods and thermal histories might induce or change lattice strains, including intra-grain microstrains. Lattice strain changes the bond strength between cations and anions and thus can alter ion migration barriers. The author proposed to take lattice strain as an additional microstructural measurement to characterize atomic

disorder in metal oxide thin films. Such measurements are made difficult by microstrains that yield no change in average lattice parameter but significantly increased spread in their values across regions as small as one grain.

Atomistic simulations suggest that increased oxygen ion mobility can come from tensile strain in YSZ [55]. Kushima and Yildiz predicted an enhancement of oxygen diffusivity in biaxially tensile strained 9 mol% YSZ using kinetic Monte Carlo simulations at different temperature and strain states. Dilation is suggested to decrease the ion migration barrier largely by weakening the oxygen-cation bond strength. Though increases in conductivity of up to 3-4 orders of magnitude are predicted to be possible at low temperature, the effect of strain is also predicted to diminish as temperature is increased.

The mismatch of thermal expansion coefficient between a YSZ thin film and the underlying substrate may induce stress, as a sample is typically measured in a range of temperatures. However, thermal stresses are much less likely than other sources of residual stress to cause appreciable changes in conductivity. The averaged linear thermal expansion coefficients between 25°C and 1000 °C are $10.5 \cdot 10^{-6} \text{ K}^{-1}$ for 8 mol% YSZ [56]. MgO has a thermal expansion coefficient of $13.9 \cdot 10^{-6} \text{ K}^{-1}$ between 25 °C and 1000 °C [57] and Al_2O_3 is similar. Thermal expansion mismatch strain is, to first order, $(\alpha_s - \alpha_f) * \Delta T$. For $\Delta T = 1000 \text{ K}$, the mismatch strain is only ≈ 0.001 . According to Kushima and Yildiz [55], this amount of strain would cause a roughly 50% increase in oxygen diffusivity, which is negligible relative to the reported orders of magnitude changes in conductivity. Lattice parameter mismatch between the YSZ thin film and substrate may also cause stress in thin films. However, as shown in Figure 9, the effect of the substrate is negligible for at least some substrates (MgO and

Al_2O_3 in particular). So, it is supposed that the substrate mismatch contribution to film stress is less than that arising from the other mechanisms by which residual stresses are known to develop in thin films. These other mechanisms will be highly dependent upon specifics of the film deposition process, and thus may lead to the low repeatability demonstrated in Figure 7. It should be mentioned that the amount of strain required to accommodate lattice mismatch between YSZ and either MgO or Al_2O_3 is sufficiently large to suggest incoherent interfaces.

Janek's group has reported a series of theoretical and experimental studies on the influence of interface and elastic strain on ionic conductivity in nanoscale solid electrolyte thin films [41, 58-62]. Nanoscale multilayer thin films, consisting of YSZ and insulating rare earth metal oxides ($\text{RE}_2\text{O}_3 = \text{Y}_2\text{O}_3, \text{Lu}_2\text{O}_3$ and Sc_2O_3) were fabricated with coherent or semicoherent interfaces and the in-plane conductivity was measured. As shown in Figure 10, It was found that in YSZ/ Y_2O_3 system, where the lattice misfit was 3.09% dilative, the ionic conductivity increased, with the amount of increase in proportion to the reciprocal thickness of the YSZ layers. In the YSZ/ Sc_2O_3 system, where lattice misfit was 4.28% compressive, the ionic conductivity decreased and again the effect increased in proportion to the reciprocal thickness of YSZ layers. In the YSZ/ Lu_2O_3 system, where lattice misfit was only 1.02%, the ionic conductivity remained unchanged and was independent of the thickness of YSZ layers.

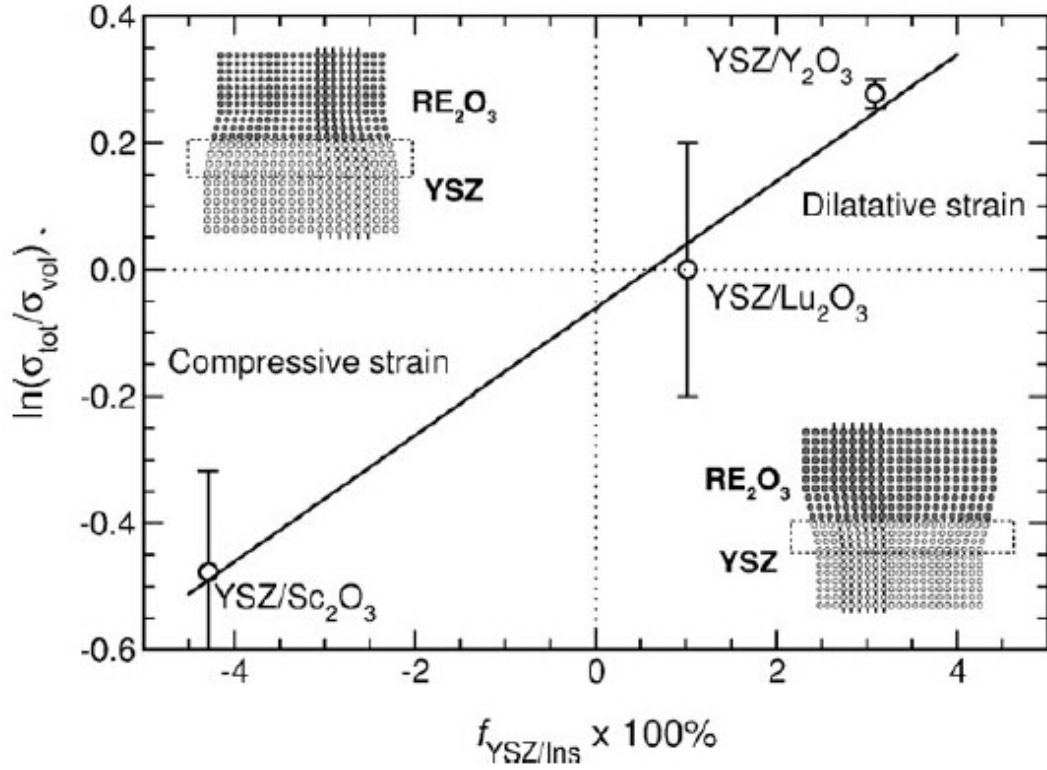


Figure 10 Plot of the logarithm of the maximum change $\sigma_{tot}/\sigma_{vol}$ of the total conductivity relative to the bulk conductivity against the mismatch factor $f_{YSZ/Ins}$. Reprinted with permission from reference [41].

It was proposed in these papers that the strained interfaces would change the total conductivity of the multilayers by an activation volume mechanism. The ionic conductivity of strained interface (σ_{int}) was different with the bulk conductivity (σ_{vol}) and quantified as below [41]:

$$\ln \frac{\sigma_{int}}{\sigma_{vol}} \approx \frac{1}{3} \frac{\Delta V_{V_O}^M}{RT} \frac{Y_{YSZ}}{1 - \nu_{YSZ}} \cdot f_{ZrO_2/RE_2O_3} \quad (6)$$

where $\Delta V_{V_O}^M$ is the volume of migration for the oxygen vacancies, Y_{YSZ} is the elasticity modulus and ν_{YSZ} the Poisson ratio of YSZ, and f_{ZrO_2/RE_2O_3} is the elastic strain. $\Delta V_{V_O}^M$ is positive for a vacancy mechanism, so when f_{ZrO_2/RE_2O_3} is positive, as in the

YSZ/Y₂O₃ system, σ_{int} is larger than σ_{vol} . When f_{ZrO_2/RE_2O_3} is negative, as in the YSZ/ Sc₂O₃ system, σ_{int} is smaller than σ_{vol} . Thus, dilative strain increases the ionic conductivity of the YSZ near the interface, and compressive strain has the opposite effect. Upon decreasing the thickness of YSZ layers, the volume ratio of YSZ near the interface increased, and so these effects are proportionally more significant to the total conductivity. Ultimately, diffusivity/conductivity increases by about a factor of 2 at 520 °C – 560 °C were found for the thinnest YSZ films in proximity to a Y₂O₃ lattice, corresponding well to the activation volume of 2.08 cm³·mol⁻¹ that was reported previously for a YSZ bulk single crystal [63]. Since this mechanism effectively reduced the activation energy of migration, larger effects are expected at lower temperatures.

A few of the reports of improved YSZ film conductivity suggested significant residual stresses in the films. Sillassen et al. found that the cubic YSZ XRD peaks were shifted towards larger d-values in the out-of-plane direction [31]. Roughly -1% in-plane elastic (compressive) strain was calculated from the apparent peak locations. Unfortunately, other papers described above provide little direct data for comparison.

Based on the simulation work of Kushima and Yildiz, the roughly 1 % strain found in the works mentioned above would increase the diffusivity by a factor of 5 around 500 °C. Such enhancement is insufficient to fully explain the orders of magnitude conductivity increases suggested in references [31]. More careful characterization of residual stresses and more direct experimental verification of the simulations are in order. Kushima and Yildiz did not directly explore the effects of in-plane compressive strain, however Schichtel et al. found experimentally that tensile strain indeed improved conductivity while compressive strains decreased it [41]. Thus,

the fact of increased variability in reported conductivity (if not yet its quantitative magnitude) can be explained by largely uncontrolled residual stresses.

1.5 Ceria-based Thin Films

Compared with YSZ thin films, gadolinium doped ceria (GDC) thin films are a promising electrolyte candidate for intermediate-temperature SOFCs because of their larger oxide-ion conductivity and lower activation energy of conduction. Much of the previous discussion concerning zirconia-based electrolytes can be applied to ceria-based electrolytes, though they remain less studied. One major concern for doped ceria is its chemical reduction at elevated temperature in a reducing atmosphere, which induces electron conductivity.

As with YSZ thin films, a number of studies of GDC thin films with nanometric thicknesses have been published recently [64-69]. For example, Suzuki et al. [66] found the ionic conductivity of 20 mol% GDC thin films increased with decreasing grain size. The author suggested that the conductivity increase was due to the segregation of impurities such as Si being reduced on a per-grain-boundary basis as the total grain boundary volume increased. This explanation follows from the work of Aoki et al., who suggested similar effects in YSZ [47]. Huang et al. [70] reported increasing conductivity with decreasing GDC film thickness from 1500 nm to 20 nm. Interestingly, an absence of grain boundary resistance was found for films with thickness close to the 10 nm – 50 nm grain sizes. The authors proposed that these effects resulted from the reduction of grain boundary volume fraction in the measurement direction, which was through the thickness of the film. Lee et al. [71] similarly found increasing conductivity with decreasing thickness. In that work, GDC thin films with thicknesses from 403 nm down to 52 nm were deposited on (0001)

sapphire substrates. They observed increasing out-of-plane dilation strain as well as both the activation energy and pre-exponential factor of the conductivity with decreasing thickness. The authors concluded that the increased strain caused these conductivity effects.

The mechanism of increased conductivity of nanoscale GDC thin films relative to bulk values remains unclear. One possibility is reduced grain boundary resistance, due to fewer impurities per grain boundary, as suggested by Suzuki [66], or reduced number of grain boundaries, as suggested by Huang [70]. Note that for these behaviors to be increasingly active for reduced film thickness, in the first explanation, the grain size must reduce as the thickness decreases, but in the second, the grain size must remain the same across all film thicknesses. Another possibility is residual stresses, including microstrain near grain boundaries and amorphous regions [54]. When decreasing the thickness, the volume fraction of the film near the substrate interface increases. The abrupt change in composition, crystal structure, thermal expansion coefficient, and lattice parameter can induce stresses in the film. The stress may weaken the ionic bond strength therefore increase the ionic diffusion [55]. Rupp recently reviewed lattice strain and atomic disorder in thin film oxide electrolytes and concluded that these factors play a key role in the ionic conductivity, in particular at determining the activation energy of conduction in doped ceria films [54].

1.6 Summary of the Literature

From the literature reports above, it is clear that the experimental results on conductivity of nanoscale YSZ and GDC thin films remain controversial. In Figure 7, each symbol represents the conductivity of one reported YSZ thin film sample with nanoscale thickness. This figure presents data from researchers that used different

deposition techniques, substrates, and processing atmospheres to prepare the nanoscale thin films, but all represent films of nominally pure YSZ deposited as a single layer. The dopant contents of all of these films were between 7.5-9.5 mol%. All of the measurements were recorded with the sample in air. YSZ is very difficult to chemically reduce, typically only exhibiting significant electron conduction at oxygen partial pressures well below 10^{-20} atm. Combined with the high oxygen diffusivity and the short diffusion path from the air interface to the entire volume of the film samples, it is difficult to imagine that any of these films, even if slightly reduced when first deposited, remain reduced when heated to measurement temperatures. Thus, it is strongly assumed that the values presented in Figure 7 represent oxygen ion and not electron (or hole) conductivity. From Figure 7, YSZ thin films were found to exhibit conductivities as low as 10^{-4} S/cm and as high as 1 S/cm at 500 °C. In addition, the activation energy for nanoscale YSZ thin films ranged from 0.62 eV to 1.24 eV in the presented temperature range. The comparative lack of repeatability among the thin film results has been somewhat controversial.

When considering reported conductivity of YSZ, it is helpful to separately consider the concentration and the mobility of the mobile oxygen vacancies. For the relatively high dopant concentrations used in nearly all studies of doped zirconia, the concentration of oxygen vacancies is fixed. The short Debye length attendant with such dopant levels means that space charge regions can only affect the defect concentration over the span of a few lattice parameters or less. Increased conductivity is thus likely to arise not from increased vacancy concentration but rather from increased vacancy mobility within the lattice structure. This situation can be compared to studies that use charge carrier redistribution near interfaces in undoped materials to

increase the mobile defect concentration [72]. As discussed above, decreasing the defect migration and/or association enthalpy is key to affecting significant change in the mobility, and doing so should lead to reduced activation energy. Tailoring the mechanical strain or introducing a high concentration of linear defects remains a theoretically valid way to change the lattice structure in a way that may increase (or, for that matter, decrease) the ion mobility.

Activation energies of the conductivity-temperature product are typically around 1.1 eV - 1.2 eV for bulk YSZ. Sillassen, et al. [31] suggested that the observed activation energy in their films of 1.24 eV at high temperature corresponds to bulk-like conduction, while the activation energy of 0.71 eV at low temperature corresponds to an interfacial conduction mechanism. Kosacki, et al. obtained [42] activation energies as low as 0.62 eV for the thinner films, supporting the notion of a high mobility interfacial conduction path. Still, for films with intermediate thickness, it was reported that the activation energy was 0.62 eV at measurement temperatures greater than 650 °C but was close to bulk values at temperatures below 650 °C. It is not clear how parallel bulk and interfacial conduction paths could lead to a reduced activation energy at increased temperature, since whichever path is more conductive should dominate the behavior.

1.7 Objective of Thesis

- Trying to explain the variation of reported YSZ thin films conductivity, as mentioned above;
- Using reactive RF co-sputtering to prepare zirconia and ceria based solid oxide electrolyte thin films with high purity and modulated composition and thickness;

- Determining the growth and quality of sputtered zirconia and ceria based thin films on MgO and Al₂O₃ substrates;
- Determine the effect of films' thickness on the ionic conductivity of YSZ and GDC thin films;
- Determining the effect of substrate surface variation on the ionic conductivity of YSZ thin films;
- Determining the effect of post-annealing on the ionic conductivity of YSZ thin films.
- Determining the effect of lattice strain on the ionic conductivity of YSZ and GDC thin films;
- Determining the effect of microstructure on the ionic conductivity of YSZ and GDC thin films;

Chapter 2

EXPERIMENTATION

2.1 Zirconia- and Ceria-based Thin Films Preparation

2.1.1 Sputter Deposition of Controlled Composition

To learn the ionic conductivity of YSZ and GDC thin films as mentioned above, these thin films need to be prepared first. In this study, RF magnetron sputtering was used to fabricate zirconia and ceria based thin films. Magnetron sputtering is a physical vapor deposition technique, commonly used for the deposition of thin films. As shown in Figure 11, due to ion bombardment, materials are ejected from a target source and deposited on a substrate, such as Al_2O_3 substrate. In magnetron sputtering, a magnetic field confines charged plasma particles close to the surface of targets, thereby increasing the deposition rate.

Oxide thin films were prepared in a multi-target, custom-built reactive magnetron sputtering chamber (PVD Products, Wilmington, MA). An oxidizing environment was used so that the oxide thin films would be fully oxidized. Process parameters, such as the target power, pressure, Ar/O_2 ratio, substrate temperature and deposition time were easily controlled using software. With pure, single element metal targets (Zr, Ce, Y, Gd), DC or RF power was used for the desired high purity and without worry of target fracture from thermal shock.

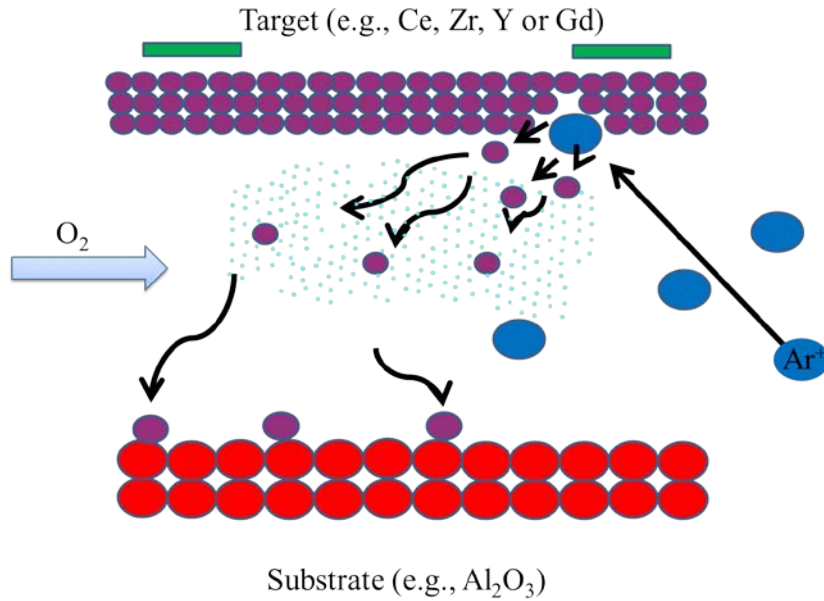


Figure 11 Schematic diagram of RF magnetron sputtering.

In order to deposit zirconia- and ceria-based thin films with controlled composition and thickness, as shown in Figure 12, the first step was calibrating the deposition rate from each target (Zr, Ce, Y, and Gd), namely the deposition rate of ZrO₂, CeO₂, Y₂O₃, Gd₂O₃. The working pressure used was 1.33 Pa (10 mTorr) with a working gas composition of 9:1 Ar:O₂ and the total working gas flow rate was held constant at 20 sccm using an active, gate valve control on the cryopump. The individual metal oxide thin films were all deposited with the substrate held at 400 °C as measured by a thermocouple in close proximity to the sample. In the later experiments, a higher substrate temperature of 650 °C was used. An increase of substrate temperature from 400 °C to 650 °C was not found to change the thickness of thin films, namely the deposition rate. Low-cost silicon substrates are used for initial work. The silicon substrate was cut from a silicon wafer to be 10 mm length×10 mm

width×0.5 mm thickness. Before being loaded into the chamber, the silicon substrate was successively rinsed using acetone, isopropanol and DI water. A substrate holder made of steel was used and able to hold 8 samples with the dimension of 10 mm length×10 mm width×0.5 mm thickness.

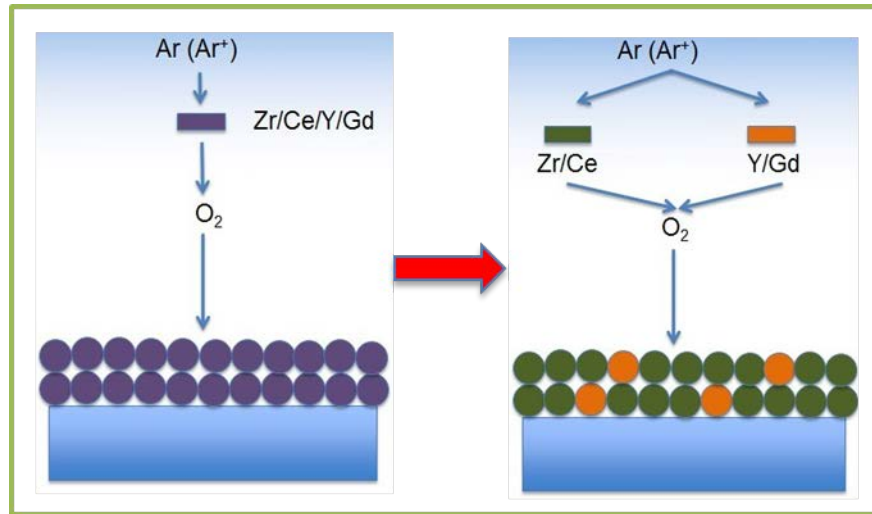


Figure 12 Schematic diagram of co-sputtering

A sharp step in topographical height between thin film and substrate was formed during sputtering by partially masking the substrate with correction fluid, as shown in Figure 13(a). The films thicknesses (and thereby deposition rate) was measured by removing the mask in an ultrasonic bath after deposition, uniformly coating the entire step with a reflective titanium film and then determining the corresponding step height using an optical interferometer (Veeco Wyko NT9100), as shown in Figure 13(b).

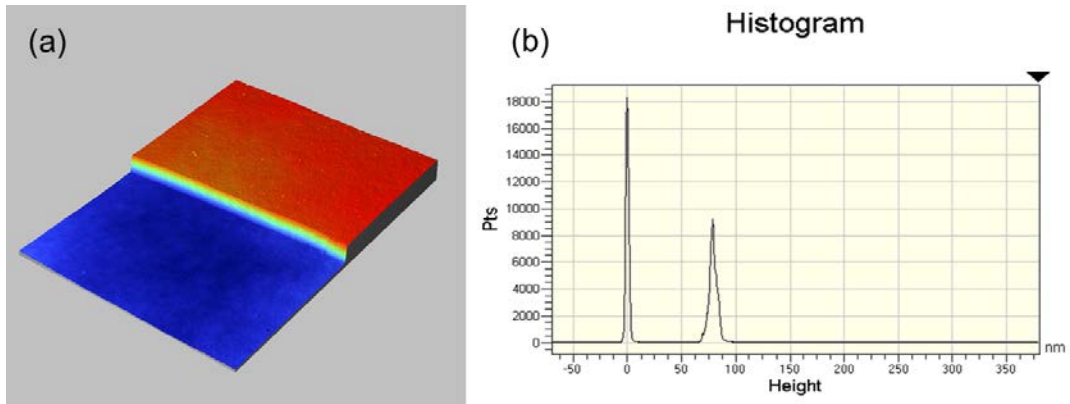


Figure 13 (a) Side view of a sharp step and (b) a histogram of the interferometer measurement.

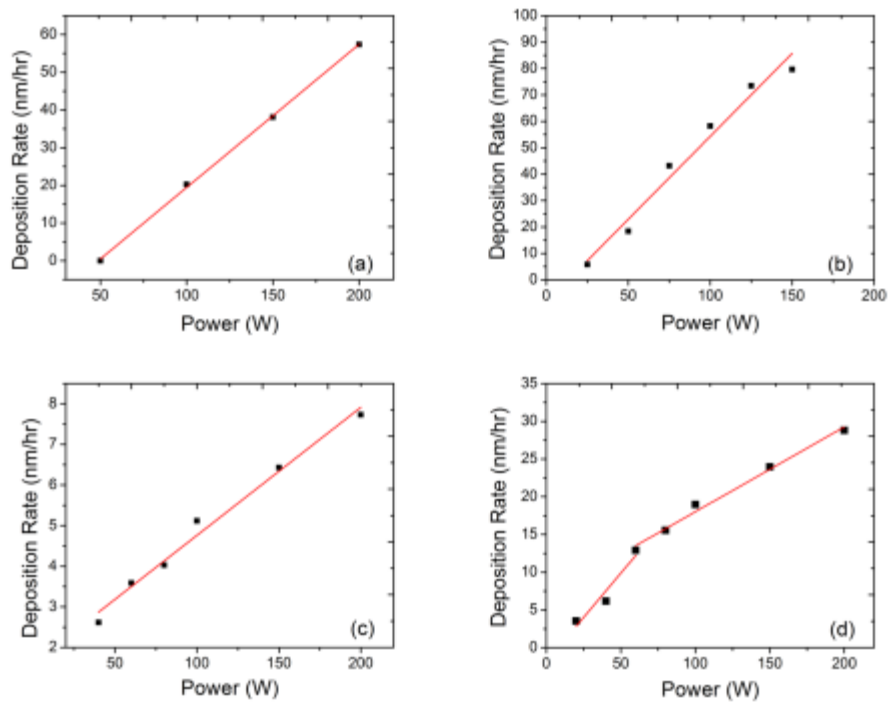


Figure 14 Deposition rate of ZrO_2 (a), CeO_2 (b), Y_2O_3 (c), and Gd_2O_3 (d) films as a function of sputtering power. Reprinted from reference [11].

The individual deposition rates of ZrO₂, CeO₂, Y₂O₃ and Gd₂O₃ are shown in Figure 14. Very good linear relationship between sputtering power and deposition rate was found in the deposition of ZrO₂, CeO₂, Y₂O₃ films. For Gd₂O₃ films, a reduced sputtering rate was consistently found at low powers, so two separate linear fits were used to fit the deposition rates at low (≤ 60 W) and high (≥ 60 W) sputtering powers. The deposition rate could be as low as nearly 0 and as high as 60 nm/hr for ZrO₂, 85 nm/hr for CeO₂, 8 nm/hr for Y₂O₃ and 30 nm/hr for Gd₂O₃. Compared with the deposition rate of ≈ 9 nm/min using reactive dc magnetron sputtering by Sillassen et al. [40], these deposition rates were much lower, so the thicknesses of these thin films could be controlled more precisely. Comparing the deposition rates of the dopants Y₂O₃ and Gd₂O₃ with the host materials ZrO₂ and CeO₂, the deposition rate of the dopants was much lower than that of the hosts, which favored the desired low concentration of dopants during co-deposition (for example, 8 mole% for YSZ and 20 mole% for GDC).

With the deposition rate measured for each target, as shown in Figure 12, series of single layer zirconia-yttria and ceria-gadolinia films with ranges of compositions were then fabricated. As shown in Figure 15, a deviation was found between the expected atomic ratio derived from the previous calibration experiments and the actual atomic ratio measured by X-ray energy dispersive spectroscopy (JEOL JSM-7400F) and X-ray photoelectron spectroscopy (ESCALab 220i-XL electron spectrometer, VG Scientific, UK). The expected atomic ratio of a film's two constituents was calculated as:

$$\text{Expected atomic ratio} = \text{Deposition rate ratio} \times \frac{\text{Density ratio}}{\text{Molar mass ratio}} \quad (7)$$

where reference values for the densities of the bulk oxides were used. The actual atomic ratio over expected atomic ratio was 1.4 for YSZ and 1.5 for GDC. The actual dopant concentration during co-deposition, on the other hand, was significantly different than the simple ratio predicted by Equation 7. One possibility is that the sputtering of the host atoms enhanced that of dopants or the deposition of the dopants weakened that of the hosts. Another possibility is that the reference values used for the density of Y_2O_3 and Gd_2O_3 films was not a satisfactory estimate.

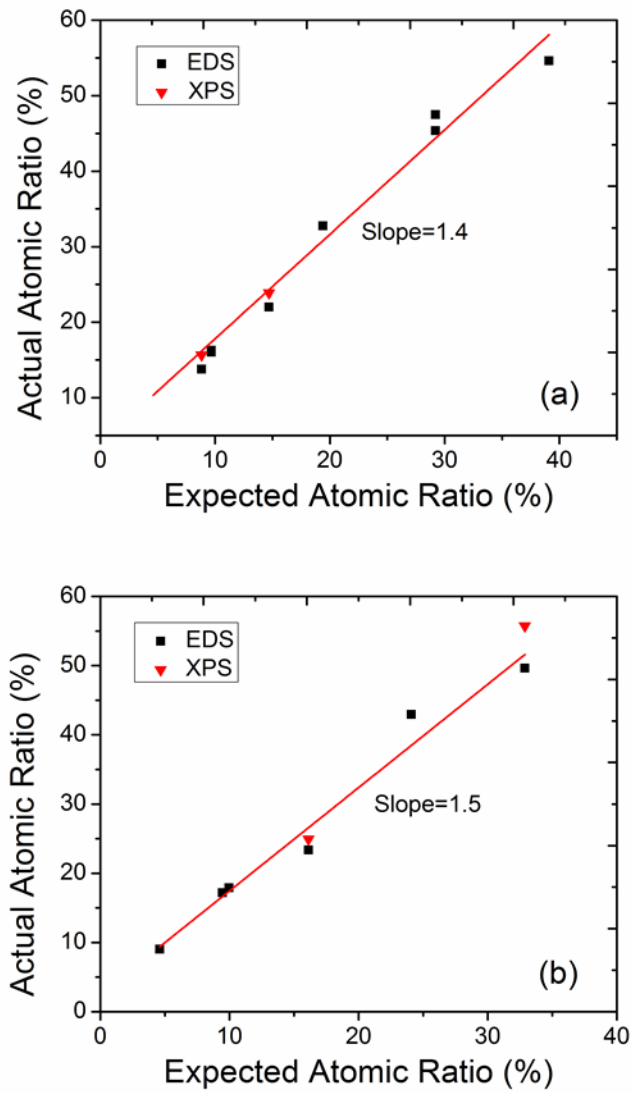


Figure 15 The relationship between the expected atomic ratio and the actual atomic ratio in deposition of YSZ (a) and GDC (b). Reprinted from reference [11].

2.1.2 Post Annealing

Table 3 Annealing conditions for the post-annealed samples.

No.	Annealing Temperature (°C)	Annealing Time (h)
1	as-deposited	0
2	650	10
3	800	5
4	800	10
5	800	20
6	1000	10

After the deposition, a group of six samples were occasionally annealed to improve the crystallinity of the sputtered thin films. A custom-built high temperature furnace capable of continuous operation up to 1600 °C was used for the post annealing. The sample chamber was a 4.5-inch diameter tube, which offered enough space for samples. The post annealing temperature, which was measured by a thermocouple in close proximity to the central area of the tube and post annealing time were controlled by a computer. As shown in Table 3, the details of the post annealing treatment are listed.

2.1.3 Substrate Preparation

At the early stage of deposition rate calibration, Si substrates were used for their low cost. All substrate surfaces must be kept clean. If the surface was contaminated, piranha was used to clean the substrate surface. Before loading the substrate into the sputtering chamber, the Si substrate was triple rinsed with acetone, isopropanol and DI water and then blown dry with filtered air to remove organic residues and other contamination.

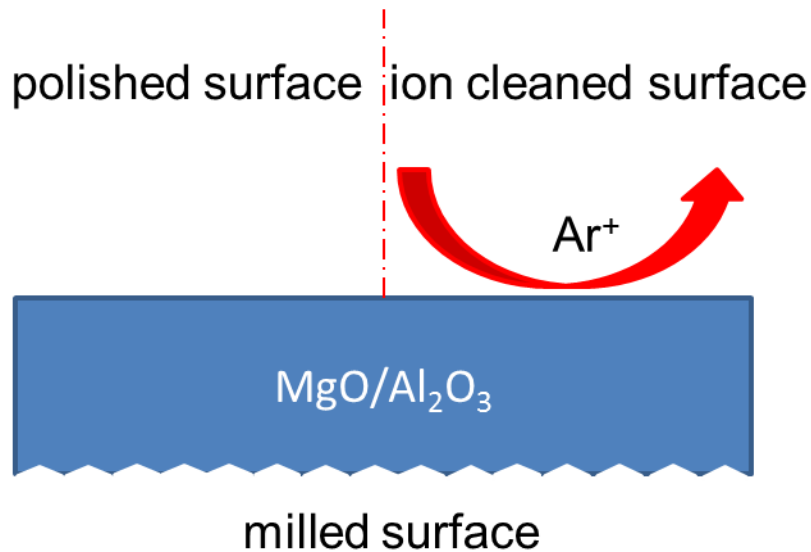


Figure 16 Schematic diagram of various substrate surfaces

Single crystal MgO (100) and Al₂O₃ (0001) (MTI Corporation) were used as the substrates for thin film samples deposition. As shown in Figure 16, the substrates were polished on one side and milled on the other side by the manufacturer. Before being loaded into the vacuum chamber, the substrates were rinsed sequentially with acetone, isopropanol, and DI water and then blown dry with filtered air to remove organic residues and other contamination.

For some samples, as shown in Figure 16, the polished surface was further ion cleaned by applying an RF bias to the substrate within the sputtering chamber before beginning the film deposition, as shown in Figure 16. The total power output from the RF source for the ion cleaning was 100 W and the chamber contained 1.33 Pa (10 mtorr) of 99.999% pure Ar. The milling rate for oxide materials under these conditions was roughly 2.4 nm min^{-1} . Ion cleaning was performed for 30 or 60 minutes, removing approximately 72 nm and 144 nm, respectively, from the surface. Deposition occurred immediately after the surfaces were ion-cleaned, with the substrates remaining in the chamber in vacuum during this time.

2.2 Structural Characterization

2.2.1 X-ray Diffraction

XRD (Rigaku IV) was used to structurally characterize the samples. XRD is a powerful technique to analyze the structure of solid materials with easy preparation of samples. $\theta - 2\theta$ pattern was used to see the crystal orientation of YSZ/GDC thin films. The thin films with multi axes must be polycrystalline with different orientated grains. The peak locations tell the lattice spacing (lattice parameters); peak shifts tell the lattice strains (no strain, uniform strain or non-uniform strain); and full widths at half maximum gives the particle size using the Scherrer Equation.

According to the Bragg equation [18],

$$n\lambda = 2d\sin\theta \quad (8)$$

where n is an integer (here $n = 1$), λ is the wave length of X-ray (1.5418 \AA), and θ is the angle between the incident ray and the scattering planes, the lattice spacing, d was determined. In addition, based on the Scherrer equation [18],

$$D = \frac{0.9 \lambda}{\beta \cos \theta} \quad (9)$$

where θ is the angle between the incident ray and the scattering planes, β is the full width at half maximum of the peak, and λ is the wavelength of X-ray (1.5418 Å), the average grain size, D was determined. It should be noted that the grain sizes calculated from this equation are those perpendicular to the substrate (i.e., in the growth direction). Thus, this value can be no larger than the thickness.

2.2.2 Scanning Electron Microscopy

Scanning electron microscopy (SEM) was used to determine the samples' topomorphology and composition. The SEM used in this project was JEOL JEM-7400F.

In this project, SEM was used to visualize the microstructure of thin films and the geometry of Pt electrodes. Cross-sectional view of the films was used to quantify their thicknesses. In addition, the microstructural visualization was used to ascertain whether or not the film was dense and continuous.

As both the YSZ and GDC films and the MgO and Al₂O₃ substrates are poor electronic conductors, a serial charging problem prevented high resolution SEM imaging. Even coating the samples with gold particles, the charging effect was still found to be serious. So SEM only offered low resolution images for the structural characterization. Pt is a good electronic conductor, so SEM could verify the geometry of Pt electrodes easily. As is described in Section 2.4, the geometry of the Pt electrodes was created using photolithography, and verification was needed to make sure the geometry was stable during the high temperature electrochemical measurement.

2.2.3 Atomic Force Microscopy

AFM (NTEGRA Prima) was used to measure the surface morphology of the samples, especially for determining the grain size. Like XRD, AFM has the advantage of easy sample preparation. When the tip is brought into proximity of a sample surface, forces between the tip and the sample lead to a deflection of the cantilever according to Hooke's Law. The cantilever used was silicon or silicon nitride with a tip radius on the order of 7 – 10 nm. Accordingly, AFM allowed measurement to nanoscale. In addition to grain size analysis, AFM was used to quantify the roughness of substrate surfaces.

2.2.4 Transmission Electron Microscopy

Transmission electron microscopy (TEM) (JEOL JEM-2010F) was the main tool to structurally characterize YSZ thin films. A JEOL JEM-2010F FasTEM with 1.0 Å lattice resolution was used in this project. Compared with XRD and AFM, the disadvantage of TEM is that the sample preparation is much more difficult. For example, a sample (solid oxide thin film on substrate) was first cut into 2 mm x 2mm using a diamond knife. Then milling the substrate side on the sand paper decreased the thickness of sample (more than 500 μm) to 100 μm. The 100 μm thick sample was thinned by dimple to 20 μm, which followed by an Ar-ion milling to obtain a tiny microscale hole.

Both bright and dark field image was used to show the structures of thin films. The grain (thus grain size) was obvious, especially in dark field image. The surface roughness was also visible. Selected area electron diffraction (SAED) show the lattice plane packing orientations, which proved the growth orientation of YSZ and GDC thin films. The high resolution TEM image show crystal lattice. The information

about film interfaces, misfit dislocations, and low angle grain boundaries were visible to assist in determining epitaxial relationships.

2.3 Compositional Characterization

X-ray photoelectron spectroscopy (XPS) was used for compositional characterization. XPS is a surface sensitive and compositionally quantitative technique, which can quantify empirical formula and chemical state of the elements in the samples. By producing a beam of X-ray, XPS irradiates the sample with the beam focused on. Electron in the sample obtains energy from X-ray and ejects from the sample. Electron sensors detect the electron by measuring the energy and number of electrons, from which the compositional information is analyzed. The XPS instruments used in this study were ESCALab 220i-XL electron spectrometer (VG Scientific, UK) and EA125 electron spectrometer (Omicron Nano Technology, Germany). Binding energies of Y, Zr and C were collected using XPS. A non-monochromatic aluminum (1486.5 eV) X-ray source was employed. Corrections were made using the adventitious carbon C1s peak located at 284.6 eV. 50 eV and 25 eV pass energies were used for survey scans and high resolution scans, respectively.

Besides XPS, energy dispersive X-ray spectroscopy (EDS) (JEOL JEM-7400F) was another technique to detect the composition of samples. The working principle is that: the instrument creates a high-energy beam of electrons, which is focused on the sample surface. The incident beam interacts with the sample atom and activates it from its ground state. An electron in sample atoms' inner shell absorbs energy from the incident beam and is ejected. An electron in the outer shell then drops into the vacancy left behind and releases a characteristic X-ray, which is detected by sensors

and reveals the compositional information of sample atoms. The compositional accuracy of EDS is generally worse compared with XPS.

2.4 Interdigitated Electrode Fabrication

Electrodes were required to make the impedance measurements. For simple data interpretation, Pt electrodes was used here as Pt is a good electronic conductor, stable in both oxidizing and reducing atmosphere and good catalyst. The samples in this study were all nanoscale thick films, which offered quite high in-plane resistance. To get a measurable resistance value using impedance spectroscopy, a micron-scale Pt electrode pattern was fabricated. Table 4 lists the geometry values of the electrodes.

Table 4 The geometry values of electrodes.

No.	1	2	3	4	5
Finger width (μm)	25	25	50	100	200
Finger spacing (μm)	10	25	50	100	200
Total length (μm)	1031600	681000	283000	115000	55000

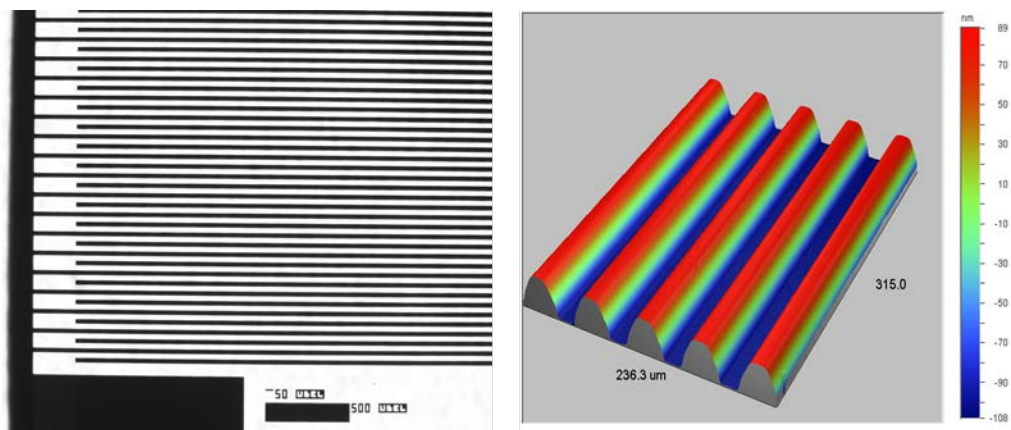
Lift-off photolithography was used to define interdigitated platinum electrodes on the samples (thin films deposited on substrates). At first, the samples were cleaned with acetone, isopropanol and DI water. A clean surface was very important for the microscale electrodes' preparation, any microscale dust or other contaminations might ruin the electrode by introducing short circuits or open circuits. If necessary, ultrasonic was used to remove any visible dust. Beside the kind of physical

contamination, the chemical contaminations might also be a serious issue. In that case, piranha was used to remove any chemical contaminations.

The second step was spin coating of the photoresist. The photoresists I tried in this study were mainly negative NR series and positive AZ series. Finally, it was found that AZ9260 was the best choice. The viscosity of AZ9260 is relatively high and the spin speed used was 4000 rpm for 1 min, which decreased the thickness of photoresist close to 7 μm . Right after the spin coating, the soft bake at 110 $^{\circ}\text{C}$ for 3 min was given to solidify the photoresist.

The next step was UV light exposure of the sample. The UV light source used had an intensity of 9.3 mJ/s. For the sample spin coated with AZ9260, the UV light exposure lasted 40 s. At last, the development with a solution of AZ400K diluted 1:3 with water for 3 min was used to develop the photoresist pattern completely.

After defining the electrode pattern, magnetron sputtering with Pt single elemental, metallic target was used to deposit Pt thin films as the electrode. The power used for sputtering was 50 W and the atmosphere pressure was 10 mtorr with pure argon (99.999%). The Pt deposition of 35 min resulted in a thickness of 200 nm. If the adhesion of oxides-Pt interface was not good, the addition of a quite thin (~ 5 nm) Ti buffer layer was used to enhance the adhesion. Figure 17 shows an electrode with a finger width of 25 μm , finger spacing of 25 μm and thickness of 200 nm.



Pt electrode

Figure 17 Representative microscopy (left) and 3D image (right) of the electrodes.

2.5 Electrochemical Characterization

Impedance spectroscopy was the primary electrochemical characterization tool in this research in order to study the ionic electrolytic conductivity which was of interest in this study. The traditional measurement of electrical resistance is performed by applying a voltage and measuring the resultant current response or vice-versa, which ignores the fact that generally more than one process may contribute to the electrical response. By determining the electrical response function in the frequency domain, impedance spectroscopy could differentiate processes with different time constants. An impedance analyzer (Alpha-A, Novocontrol Technologies), which measures the complex impedance between 3 MHz and 3 μ Hz, was used in this project.

At first, bare substrates (MgO and Al₂O₃) with identical electrodes were tested to ensure that film resistances are always at least one order of magnitude less than that of a bare substrate. After excluding the possible electronic contribution from substrates, the conductivity of thin film samples was determined by impedance

spectroscopy in the frequency range from 3 MHz to 1 Hz between temperatures of 300 °C – 650 °C in flowing dry air. The dry air prevented the possible proton conduction from humid air. The samples were loaded into a tube furnace, which was capable of operation to as high as 1200 °C.

For doped ceria, the impedance measurements were performed over a range of oxygen partial pressures (P_{O_2}). N_2/O_2 gas mixtures was responsible for offering high P_{O_2} (as high as 1 atm), while CO/CO_2 mixture was responsible for offering low P_{O_2} (as low as 10^{-30} atm). Measurement under different oxygen partial pressure was used to characterize the defect chemistry.

The impedance spectra were analyzed with ZView software (Version 3.3, Scribner Associates). Equivalent circuit modeling was used for fitting the impedance spectra. More details about equivalent circuit modeling are given in Section 3.3.

Chapter 3

RESULTS

3.1 Structural Characterization of YSZ Thin Films

3.1.1 Structural Characterization of YSZ Thin Films on MgO Single Crystal

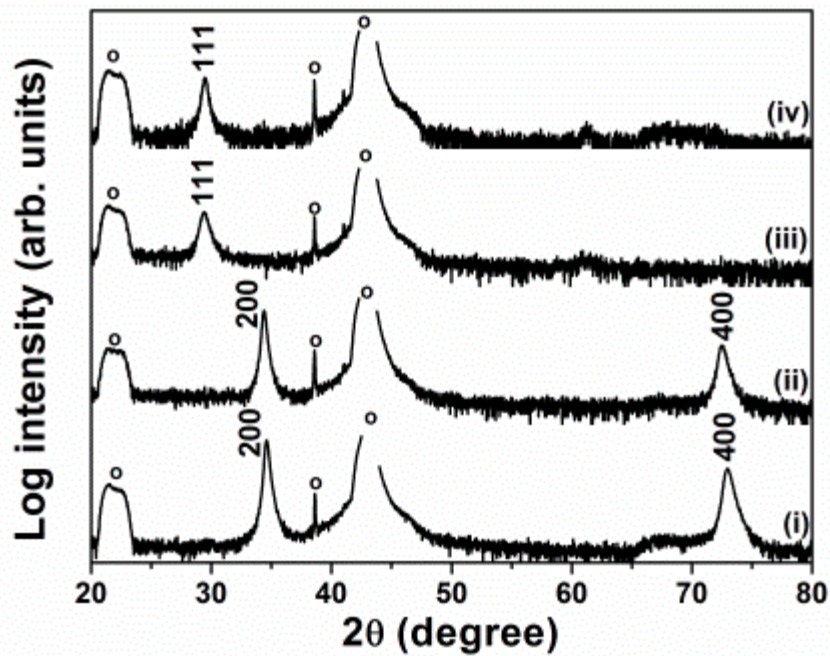


Figure 18 XRD patterns of various YSZ thin films on MgO (100). The deposition details of these films are listed in table 5. Peaks marked with a circle are indicative of the substrate. Other peaks are marked with Miller indices at the locations expected of cubic YSZ planes. Reprinted from reference [73].

With the sputtering technique mentioned in Section 2, YSZ thin films were first deposited on MgO single crystal. The structures of these YSZ thin films are shown below.

XRD patterns for various representative YSZ films deposited on MgO (100) substrates are shown in Figure 18. Compared with pure ZrO₂ thin films on MgO (100), as shown in Figure 19, which shows randomly-oriented monoclinic structure, all YSZ thin films exhibit a cubic structure. A few thicknesses, dopant concentrations, and deposition temperatures are represented; however these processing variables seemed to serve a lesser role relative to substrate supplier in determining the films' orientations. Different MgO (100) substrates from 4 suppliers were used here to check the repeatability of thin films growth. The first group of films were found to be oriented along the (100) direction on substrates from Coating & Crystal Inc. and Across International but along the (111) direction on substrates from MTI and Superconix. In later depositions, it was found that the crystal orientation was only repeatable on the substrates from Coating & Crystal Inc. and Superconix.

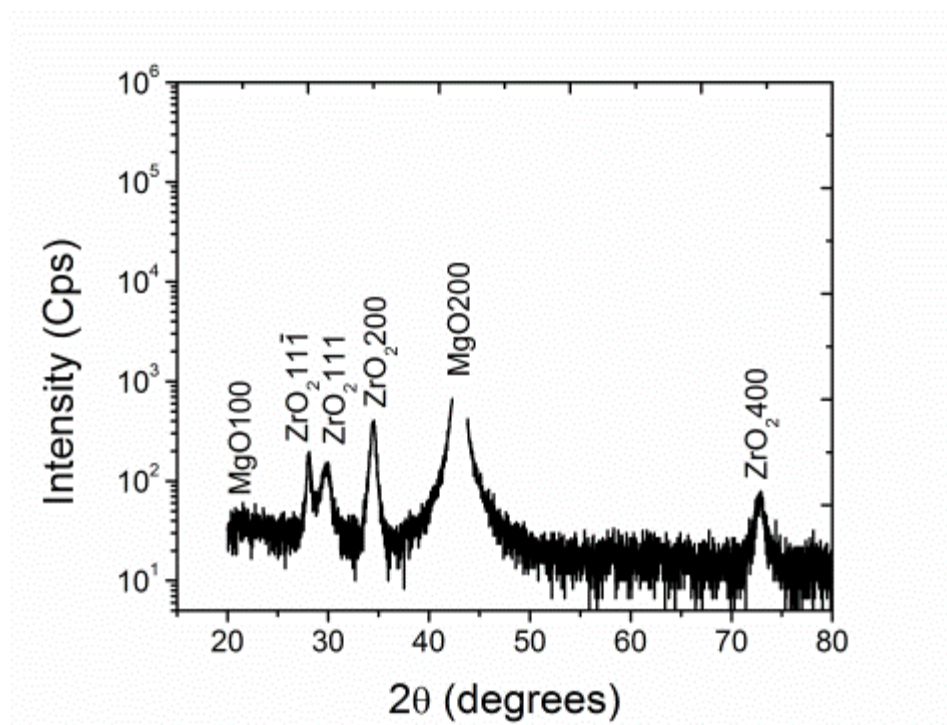


Figure 19 θ - 2θ XRD pattern of a pure ZrO_2 film deposited on MgO (100). ZrO_2 monoclinic peak appears at $2\theta \approx 28^\circ$. Reprinted from reference [11].

Table 5 Deposition conditions for the samples plotted in Figure 18.

No.	Thickness (nm)	Dopant	Deposition	Substrate
		concentration (mol%)	Temperature ($^\circ C$)	Supplier
(i)	75	9	400	Coating & Crystal
(ii)	50	14	400	Across International
(iii)	50	14	400	Superconix
(iv)	50	9	650	MTI

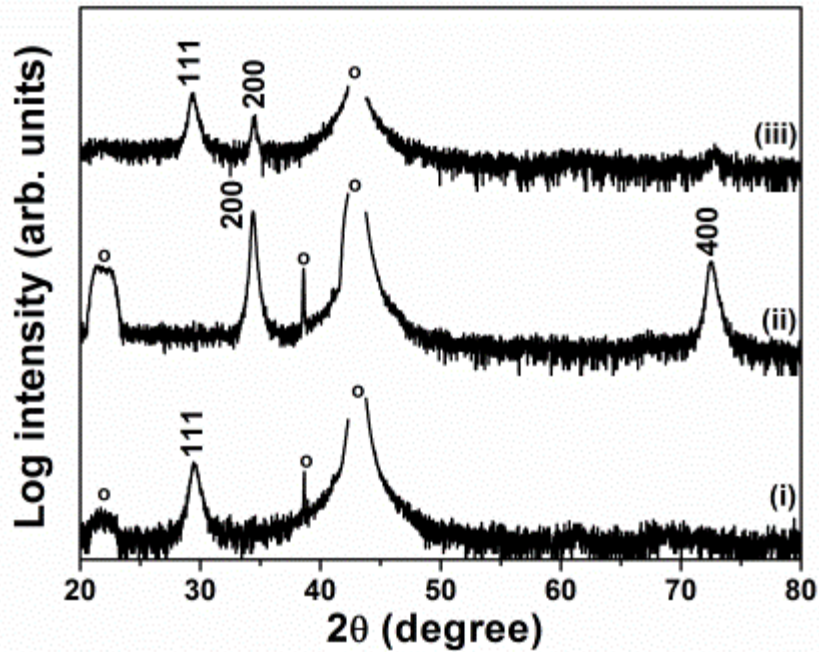


Figure 20 XRD patterns of 50 nm thick, 14 mol% YSZ thin films deposited at 400 °C on MgO (100) substrates from Across International. Peaks marked with a circle are indicative of the substrate. Other peaks are marked with Miller indices at the locations expected of cubic YSZ planes. Reprinted from reference [73].

Figure 20 shows that films deposited under seemingly identical conditions on substrates from Across International were found at times to be oriented strongly in the (100) direction, other times in the (111) direction, and still other times with mixed (111) and (100) orientations. On substrates from MTI, as shown in Figure 21, films at times were oriented strongly in the (111) direction and at other times with mixed (111) and (100) orientations. Qualitatively, based on large differences in the peak intensities, films with (100) texture had better crystallinity relative to the films with (111) or

mixed (100) and (111) texture. Here, crystallinity refers to the degree of structural order such that better crystallinity means less amorphous and/or micro-strained material in the film.

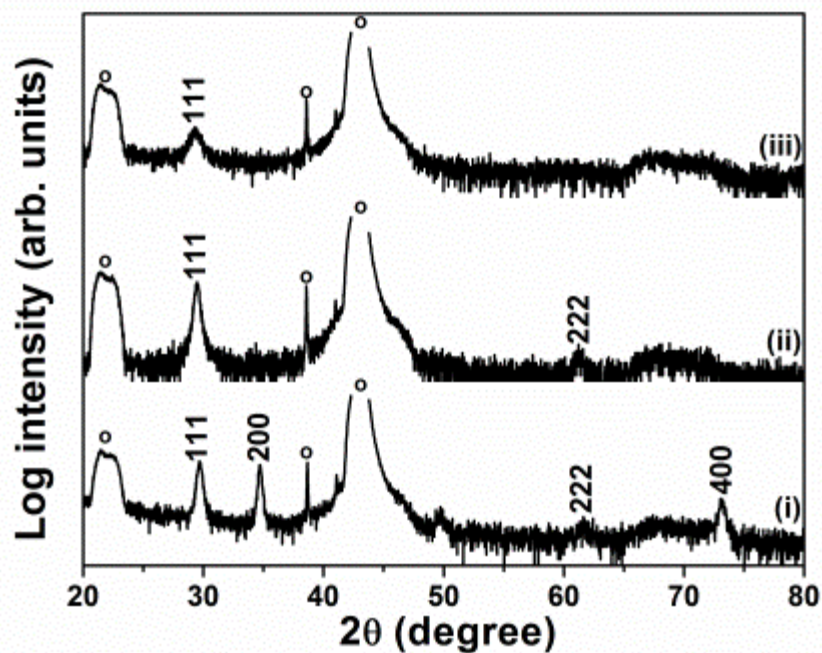


Figure 21 XRD patterns of 9 mol% YSZ thin films deposited at 650 °C on MgO (100) substrates from MTI. Samples (i) and (ii) are 50 nm thick, while sample (iii) is 12 nm thick. Peaks marked with a circle are indicative of the substrate. Other peaks are marked with Miller indices at the locations expected of cubic YSZ planes. Reprinted from reference [73].

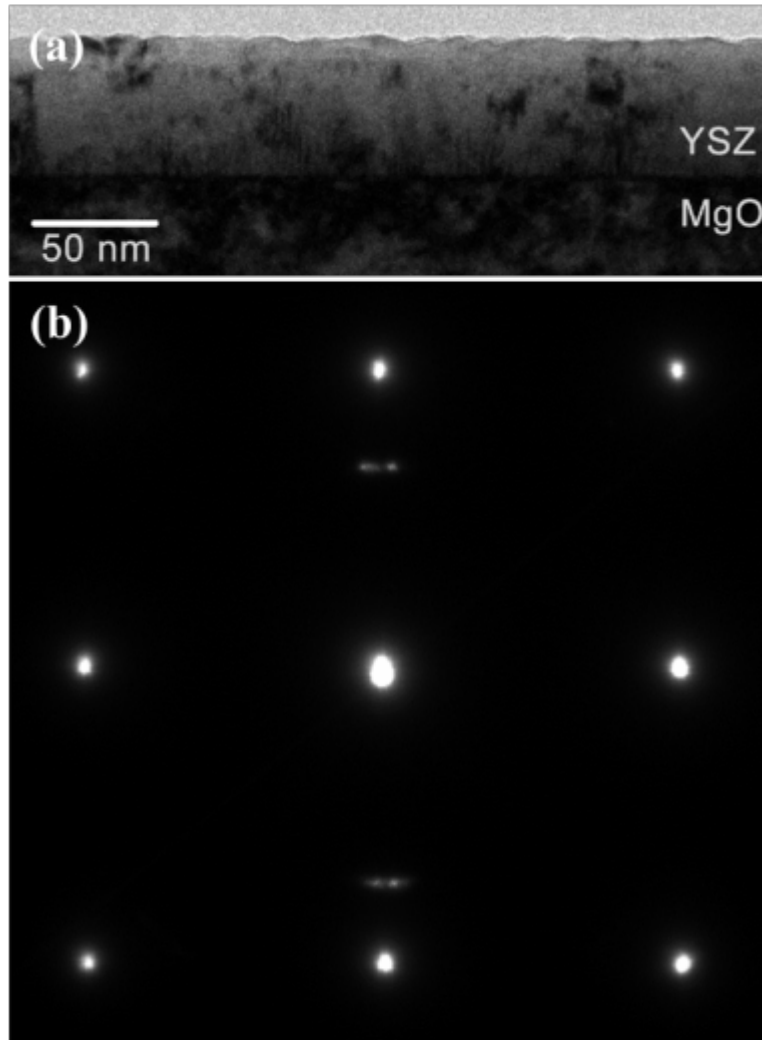


Figure 22 (a) Bright field image and (b) selected area electron diffraction of a (111) oriented YSZ thin film (film (iii) in Table 5). Reprinted from reference [73].

Figure 22(a) shows a cross-section view of a YSZ thin film on MgO (film (iii) in Table 5). The YSZ thin film is dense, continuous and homogeneous in thickness, which is around 50 nm, corroborating with the interferometer measurement. The YSZ/MgO interface is flat and the surface of the YSZ thin film is smooth. The

selected area electron diffraction (SAED) pattern for this film is shown in Figure 22(b). The weak arcs indicative of the YSZ (111) plane in Figure 22(b) suggest that (111) oriented films on MgO (100) have significant range of plane tilt and are thus polycrystalline. On the other hand, as shown in Figure 23, for (100) oriented YSZ on MgO (100) (film (i) in Table 5), a square array of plane-view diffraction spots confirms cube-on-cube epitaxial growth (though likely with some population of very low angle grain boundaries).

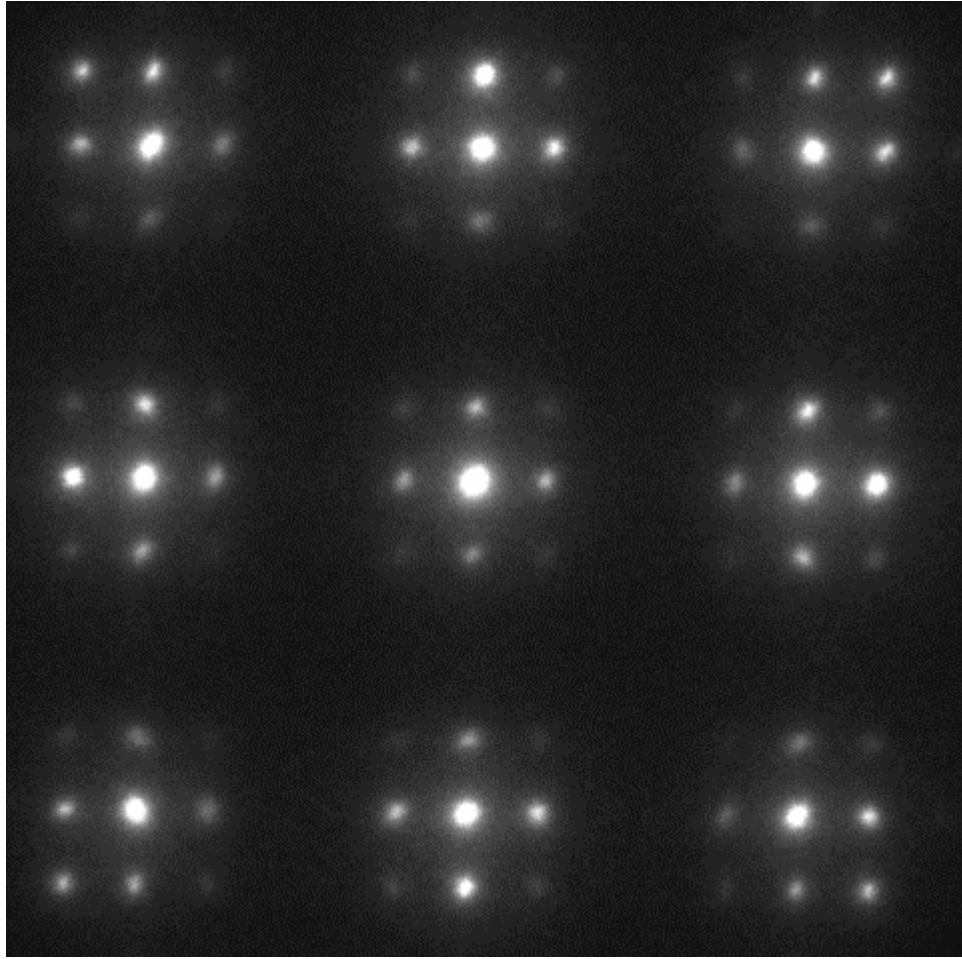


Figure 23 Selected area electron diffraction of a (100)-oriented YSZ thin film (film (i) in Table 5) Reprinted from reference [73].

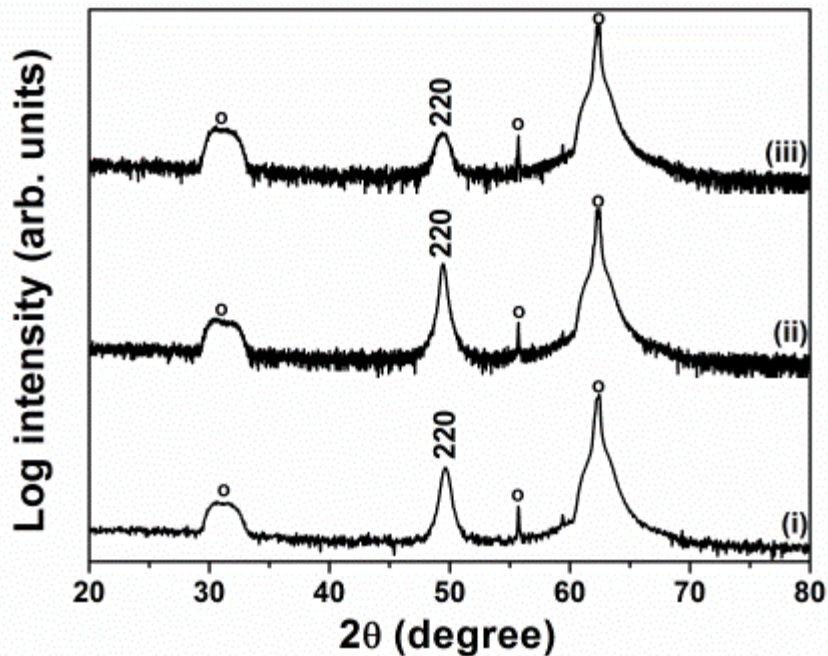


Figure 24 XRD patterns of 9 mol% YSZ thin films deposited on MgO (110) substrates from MTI at 650 °C ((i) and (ii) are 50 nm thick YSZ thin films while (iii) is a 12 nm thick YSZ thin film). Peaks marked with a circle are indicative of the substrate. Other peaks are marked with Miller indices at the locations expected of cubic YSZ planes. Reprinted from reference [73].

Figure 24 shows XRD patterns for three films of 9 mol% YSZ deposited on MgO (110) substrates (MTI) at 650 °C; the first two are 50 nm thick while the third one is 12 nm thick. Films deposited on MgO (110) substrates were repeatedly highly textured along the (110) direction. As shown in Figure 25, when the same films were deposited on MgO (111) substrates (MTI), the YSZ thin films were repeatedly oriented in (111) direction, though occasionally with a small amount of additional (100) orientation. The substrate peaks of sample (i) look different from the other two

samples, which may be due to different quality of substrate preparation resulting in slight surface crystallographic misalignment. Reseating the sample within the diffractometer and remeasuring did not produce a significantly different result. A similar result may also be noted in Figure 20, film (iii).

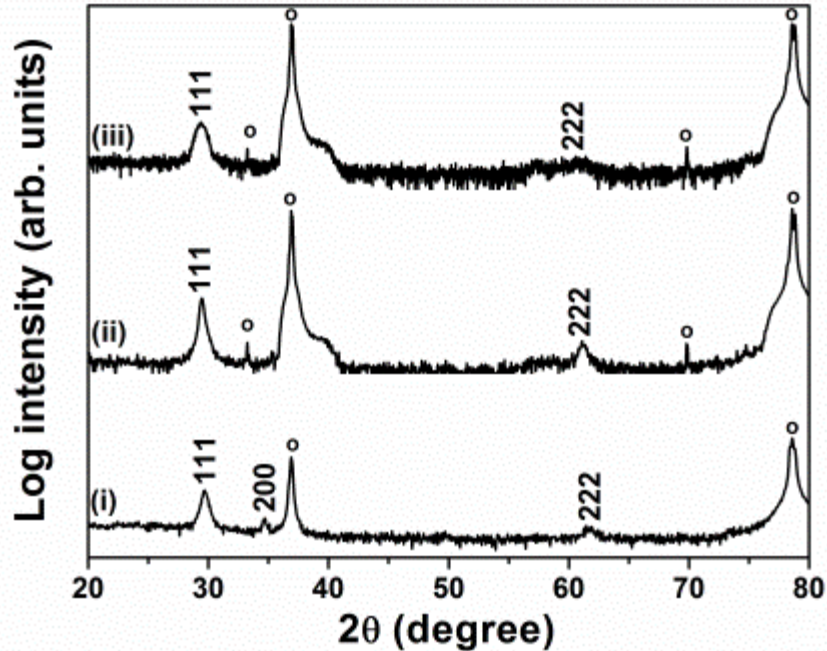


Figure 25 XRD patterns of 9 mol% YSZ thin films deposited on MgO (111) substrates from MTI at 650 °C ((i) and (ii) are 50 nm thick YSZ thin films while (iii) are 12 nm thick YSZ thin film). Peaks marked with a circle are indicative of the substrate. Other peaks are marked with Miller indices at the locations expected of cubic YSZ planes. Reprinted from reference [73].

From both XRD and SAED, YSZ film growth on MgO (100) was found to be epitaxial (or nearly so) at times, as Kosacki et al. [42] reported, but polycrystalline with (111) or both (111) and (100) orientations at other times, as Guo et al. [33] and

Rivera et al. [36] reported. Thus, the growth of YSZ thin films on MgO (100) was highly unstable in my study. Unintentional variability in the processing parameters used here is not believed to be sufficient to explain this instability. Instead, we believe the growth may largely depend on the final cut and polish quality of the MgO surface. The effects on film quality of slightly mis-oriented or vicinal substrate surfaces have been known for a long time in silicon processing[74], with similar behavior noted specifically for MgO (100) [75]. More experimentation is needed to confirm such a role of the MgO surface, including determination of whether the role is physical or chemical in nature. Clearly, the film deposition method and process specifics will also play a role, but in my work these parameters were not sufficient to explain the variability in film orientation and quality.

Regarding films on (111) MgO substrates, a similar correlation can be made in that film (i) in Figure 25 exhibited both different substrate peaks and a mixed orientation film. More strongly preferred (111) film orientation thus appears to be related to a higher quality (111) MgO substrate surface. Sillassen et al. [31] found that YSZ films deposited on MgO (111) when 58 nm thick displayed only the YSZ (111) peak but when 107 nm thick displayed an additional YSZ (200) peak. On MgO (110) substrates, the only YSZ peak found was (220) for films with thicknesses ranging from 58 nm to 420 nm. The structural findings presented here thus match these reported results well.

Above all, it is concluded that on MgO single crystal, YSZ thin films' growth was not repeatable. However, as discussed in Section 1.4.5, an ion milling of substrate surface may influence the thin films' growth. Here, different MgO substrate surfaces, which were introduced in Section 2.1.3, were tried for YSZ thin films deposition.

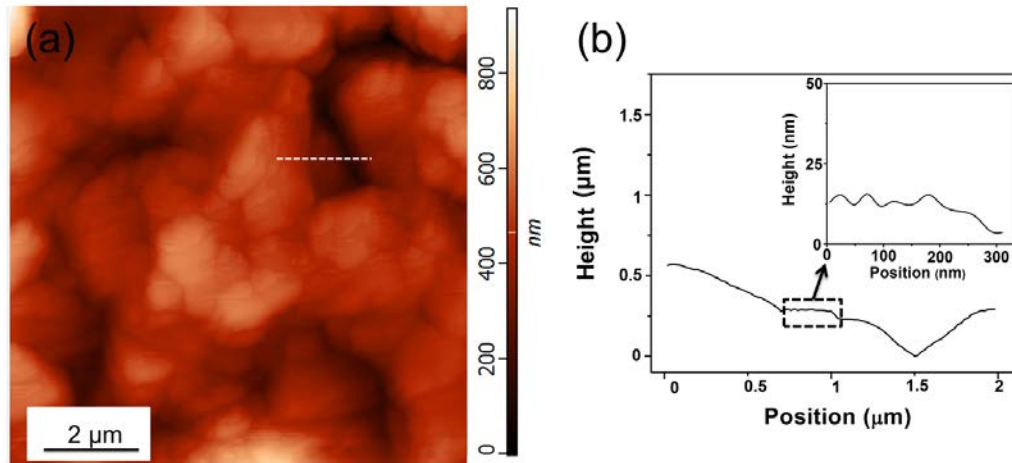


Figure 26 (a) AFM image of milled surface of MgO (or Al₂O₃) and (b) height profile along the path indicated with a dashed line. In part (a), height is indicated by shade where the scale from black to white is 800 nm. Reprinted from reference [76].

Figure 26 shows the surface morphology of the milled surface of an MgO substrate as measured by AFM. The surface morphology of the milled Al₂O₃ substrate was substantially similar. The roughness (R_A) calculated from the AFM images was around 116 nm. Sputtering is well known to provide very uniform, conformal coatings as long as the surface does not have reentrant features or high aspect ratio topographical features [77]. As seen in the height profile, the surface topographic features are all at relatively low angle. Thus, films sputtered onto this surface are expected to be continuous. The polished and ion cleaned surfaces were also measured, however the roughnesses were immeasurably low, below 1 nm, and could not be reliably quantified.

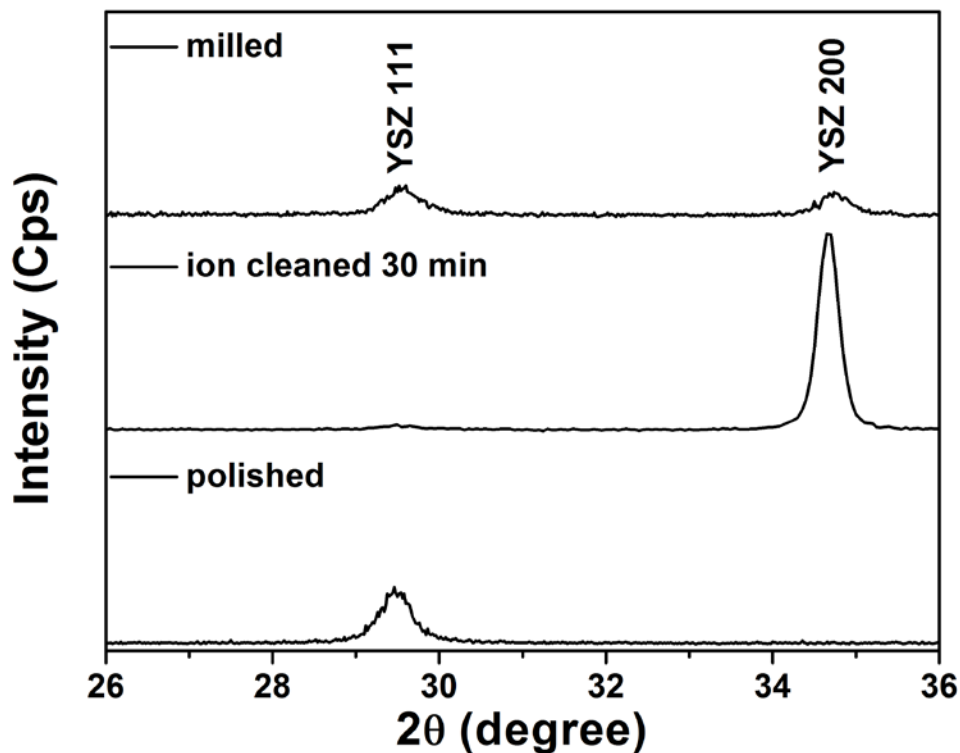


Figure 27 XRD patterns of YSZ thin films on MgO. While the patterns are offset for clarity, all are plotted over the same intensity scale. Reprinted from reference [76].

As shown in Figure 26, YSZ films deposited on MgO have different orientations depending on the surface treatment. Specifically, films deposited on polished MgO have strong (111) texture, while films on an ion cleaned MgO surface have strong (100) texture but with a very weak additional (111) peak apparent. YSZ films on a milled MgO surface had little apparent preferred orientation, with both (111) and (100) peaks at similar, low intensities.

3.1.2 Structural Characterization of YSZ Thin Films on Al₂O₃ Single Crystal

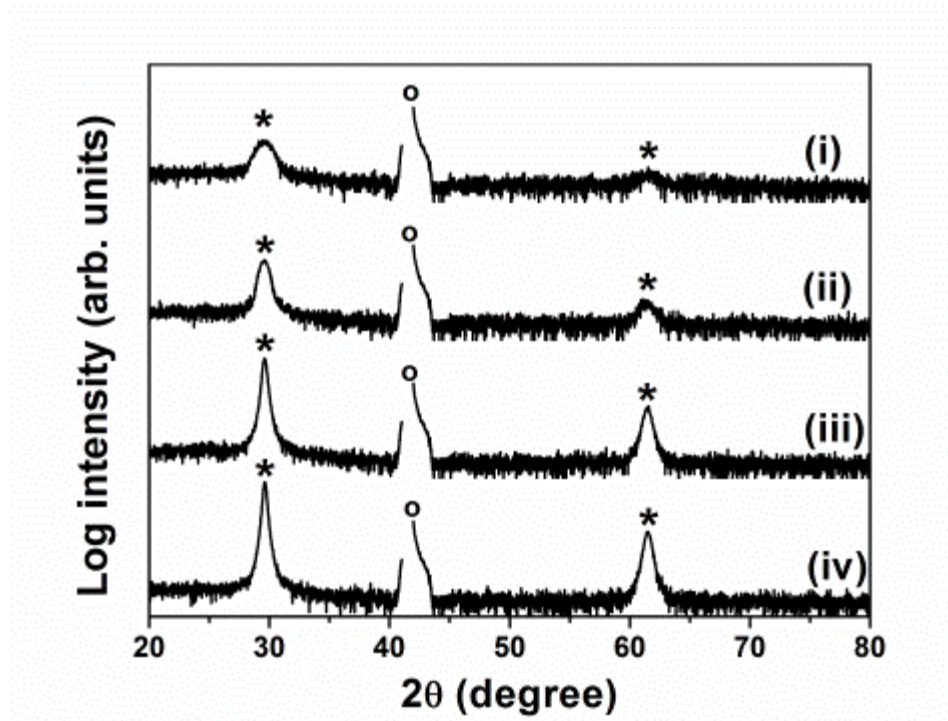


Figure 28 θ - 2θ XRD pattern of YSZ thin films with thickness 6 nm (i), 12 nm (ii), 50 nm (iii), 100 nm (iv). Note that the plotted intensity is logarithmic. The peaks near 29° and 62° indicated with asterisks represent YSZ (111) and (222), respectively; the truncated peak near 43° and indicated with the circle is Al₂O₃ (0006). Reprinted from reference [32].

In the above section, MgO single crystal substrate does not offer a repeatable growth for YSZ thin films. Here, Al₂O₃ single crystal substrates were used to see if there was any difference compared with MgO.

Figure 28 shows the XRD patterns of YSZ thin films with a thickness of 6 nm, 12 nm, 50 nm, and 100 nm. The films are all strongly oriented in the (111) direction on (0006) Al₂O₃. The thinner films exhibit broader, less intense peaks, which is to be

expected for columnar grains with thickness equal to the sub-100 nm film thickness. The consistent orientation suggests these thin films have a quite stable growth pattern on Al_2O_3 despite the high lattice mismatch between the film and substrate.

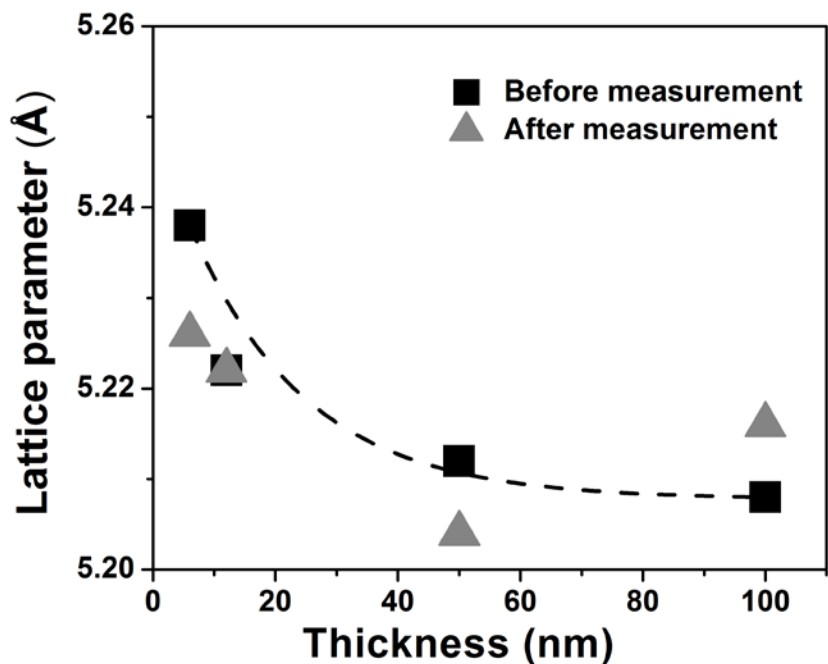


Figure 29 The lattice parameter of YSZ thin films on Al_2O_3 determined from XRD both before and after impedance measurement at 650 °C. Reprinted from reference [32].

Figure 44 presents the lattice parameters calculated from the (111) peak locations using Bragg equation, both before and after the in situ heating that occurred during the impedance measurement. The lattice parameters (5.21 Å~5.24 Å) of all thin films exceeded the literature value of 5.14 Å for 8 mol% bulk YSZ, indicating significant lattice dilation in the direction perpendicular to the substrate (i.e., the

(111)-plane spacing). The lattice parameters decreased with the increasing thickness, suggesting that the strain was due to interaction with the substrate.

Figure 30 shows AFM image of YSZ thin films deposited on Al_2O_3 . The AFM image exhibited the grains, with a grain size of around 20 nm. The roughness of film surface was just 1 nm.

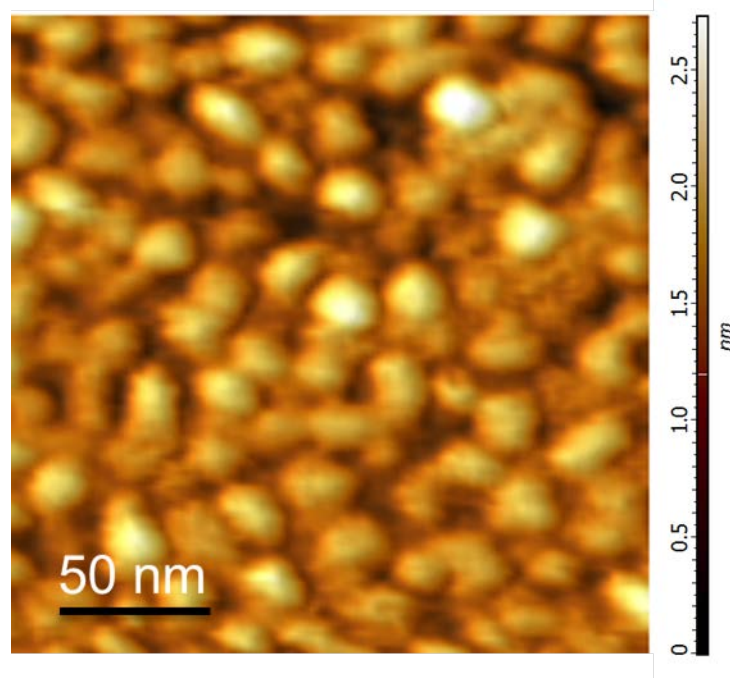


Figure 30 AFM image of 50 nm thick YSZ thin films deposited on Al_2O_3

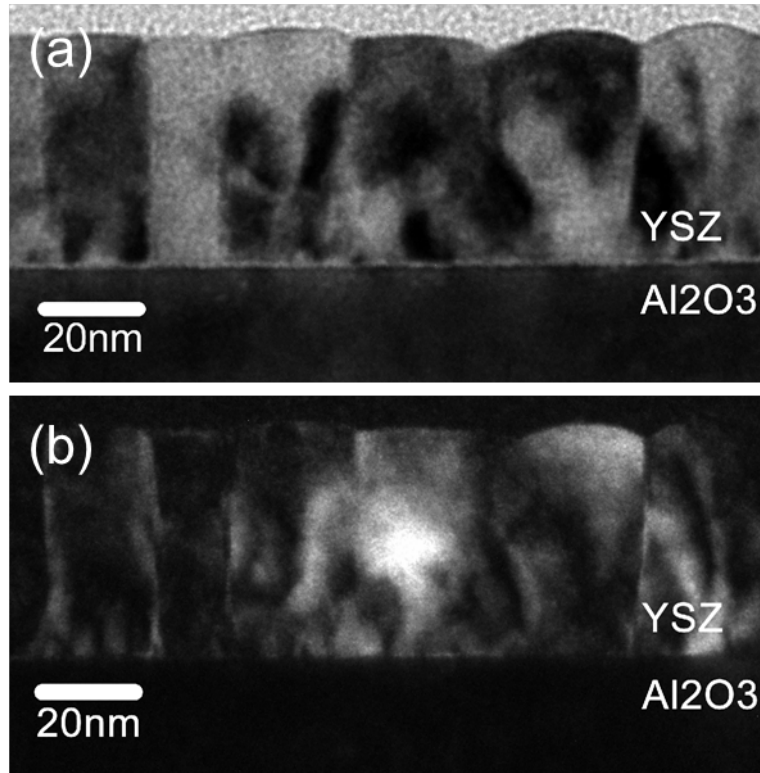


Figure 31 (a) Bright-field image and (b) dark-field image of a 50 nm thick, as-deposited YSZ thin film. Reprinted from reference [32].

Figures 31 (a)-(b) present the bright and dark field TEM images of an as-deposited 50 nm thick YSZ film on Al_2O_3 . Grain boundaries are quite clear and reveal the columnar structure of the sputtered films. Lateral grain size was found to be close to 10 nm – 20 nm, which corresponded to the grain size distribution found from AFM surface morphology measurements, as shown in Figure 30. The contrast on the YSZ thin film (dark area on the bright field image and bright area on the dark field image) indicates the existence of highly strained regions.

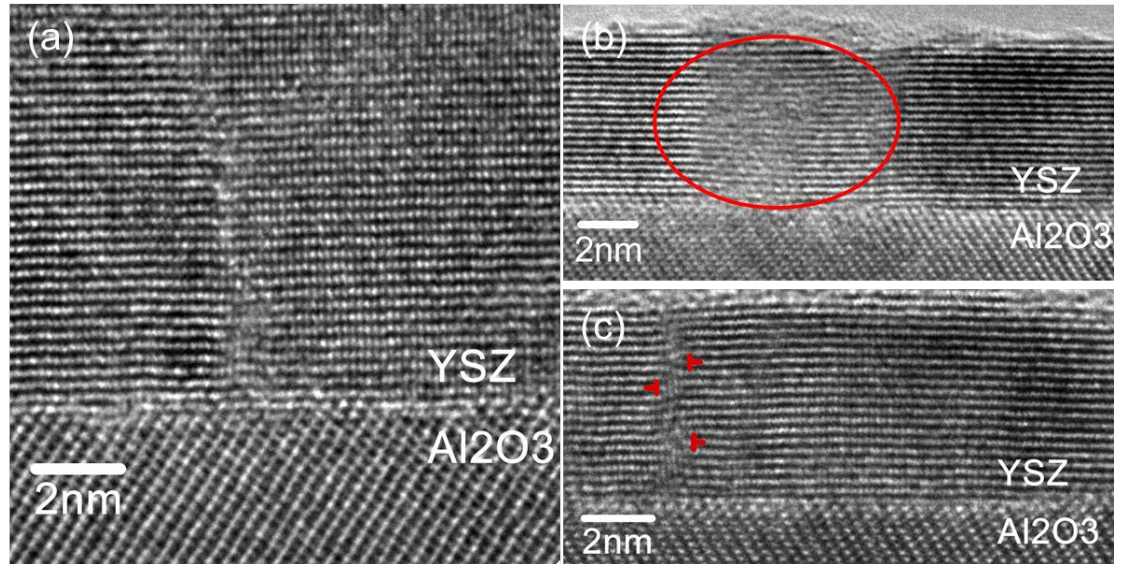


Figure 32 (a) high resolution cross-sectional image of a 50 nm thick, as-deposited YSZ thin film. High resolution image of 6 nm thick YSZ thin films (b) as-deposited and (c) after high temperature impedance measurements. The red marks indicate edge dislocations. Reprinted from reference [32].

Figure 32(a) shows high resolution TEM of 50 nm thick YSZ thin film on Al_2O_3 . The highly regular lattice structure shows that the film grew with high crystal quality on Al_2O_3 . The YSZ/ Al_2O_3 interface appears to be sharp, with no amorphization. Near the center of the image is a grain boundary. The YSZ lattice is continuous across the boundary, and thus it appears to be a low angle grain boundary. The decreased atomic misplacement of low angle grain boundaries may decrease the ion conduction blocking effect normally associated with a grain boundary, since this effect is believed to arise from crystallographic mismatch [33, 78]. The lattice continuity may also keep the strain continuous through grains rather than releasing the strain around high angle grain boundaries.

High resolution TEM images of a 6 nm thick film both as-deposited and after high temperature measurement are shown in Figures 32(b)-(c). Unlike the 50 nm thick film, in the as-deposited 6 nm thick film some amorphous or highly defected regions are apparent within the otherwise regular lattice, as highlighted in Figure 32 (b). Specifically, the areas near the left and right edges of the image exhibit a highly regular, continuous lattice, while the central area has significant lattice distortion. In the annealed film (Figure 32(c)), the lattice is much more regular throughout the film. It is believed that an annealing or recrystallization process occurred while being held at 650 °C, removing the defects and creating the low-angle grain boundaries. Like the 50 nm thick film, lattice continuity is maintained across the grain boundaries by the creation of low angle grain boundaries. As noted in Figure 32(c), edge dislocations were created near the grain boundaries and oriented in the in-plane direction, parallel to the substrate.

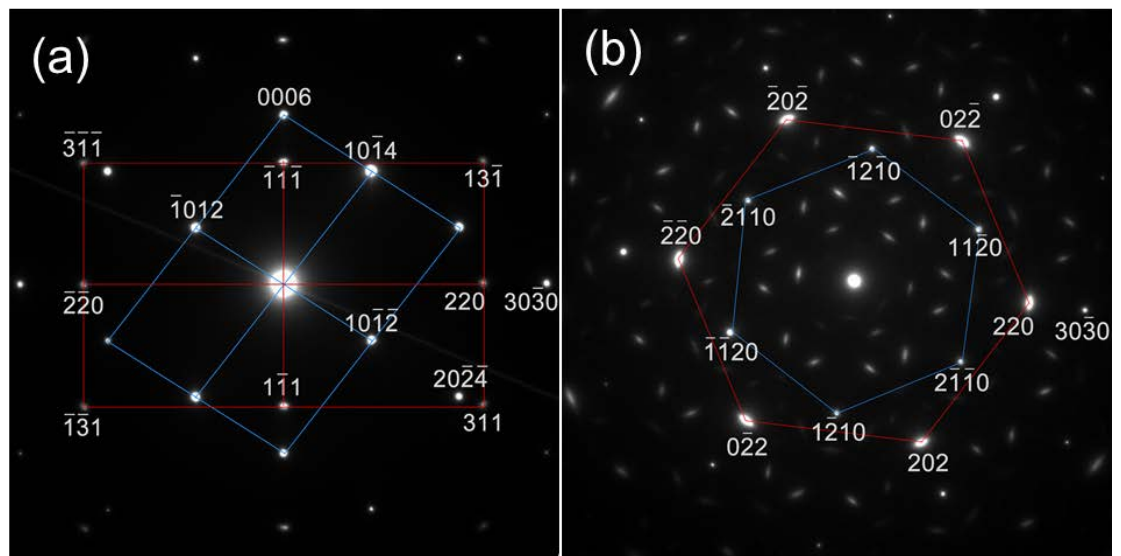


Figure 33 (a) In-plane and (b) cross-section electron diffraction of 50 nm thick as-deposited YSZ thin films. Reprinted from reference [32].

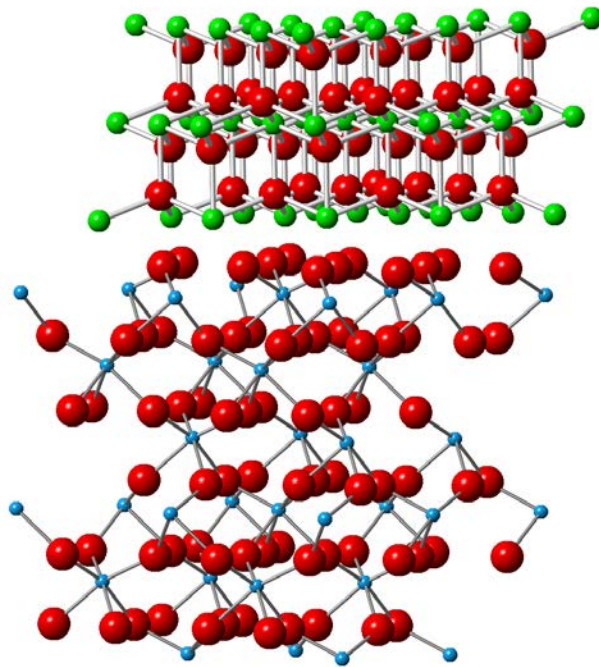


Figure 34 Solid sphere model of YSZ/ Al_2O_3 interface. Green, blue, and red spheres represent Zr/Y, Al, and O, respectively. Reprinted from reference [32].

Figures 33(a)-(b) show across-plane and in-section electron diffraction patterns of an as-deposited 50 nm thick film. In the plane view, the hexagonal packing of both Al_2O_3 and YSZ suggests epitaxial growth in $[110]\text{YSZ}/[10\bar{1}0]\text{Al}_2\text{O}_3$ direction. Note that the unindexed satellite spots in Fig. 33(b) are due to double reflections. In cross-section view, the pattern suggests the $(111)\text{YSZ}/(0001)\text{Al}_2\text{O}_3$ alignment perpendicular to the substrate, corroborating the XRD data, and $[110]\text{YSZ}/[10\bar{1}0]\text{Al}_2\text{O}_3$ alignment parallel to the substrate, corroborating the plane view diffraction. Taken together, the growth of YSZ on Al_2O_3 is epitaxial along $[110]$ $(111)\text{YSZ}/[10\bar{1}0]$ $(0001)\text{Al}_2\text{O}_3$, despite the presence of the low angle grain

boundaries. According to the epitaxial growth orientation, the packing model around the YSZ/ Al_2O_3 interface is shown in Figure 34. Here, both YSZ (111) plane and Al_2O_3 (0001) plane show at least 3-fold symmetry (Al_2O_3 (0001) plane shows a 6-fold symmetry), matching well with each other.

Just like MgO substrate, different Al_2O_3 substrate surfaces were tried for YSZ thin films deposition to see if different substrate surfaces influence the thin films growth.

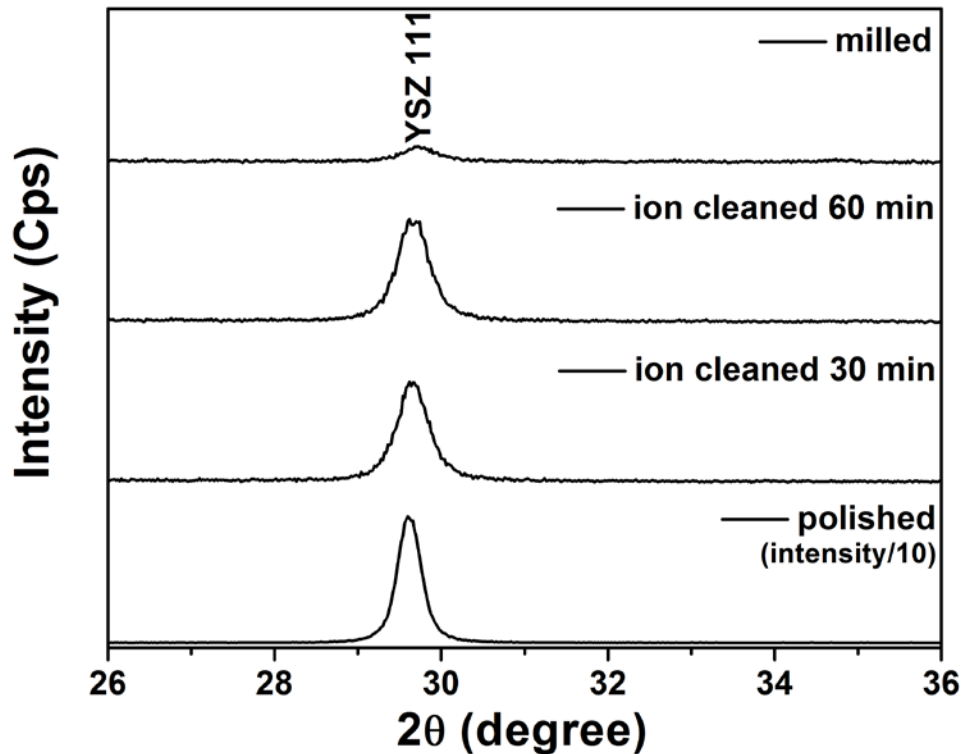


Figure 35 XRD patterns of YSZ thin films on Al_2O_3 . While the patterns are offset for clarity, all except the polished sapphire sample are plotted over the same intensity scale. The film on polished sapphire had a very high peak intensity and is plotted with values reduced by a factor of 1/10. Reprinted from reference [76].

As shown in Figure 35, all films deposited on Al_2O_3 substrates exhibit (111) textures. The specimen deposited onto a polished surface exhibited extremely high diffraction intensity relative to all other samples. The diffracted intensity decreases sharply for the films on ion cleaned surfaces, and it decreases even further on the milled Al_2O_3 surface. Interestingly, ion cleaning of the Al_2O_3 surface for 30 min or 60 min makes little difference in this regard.

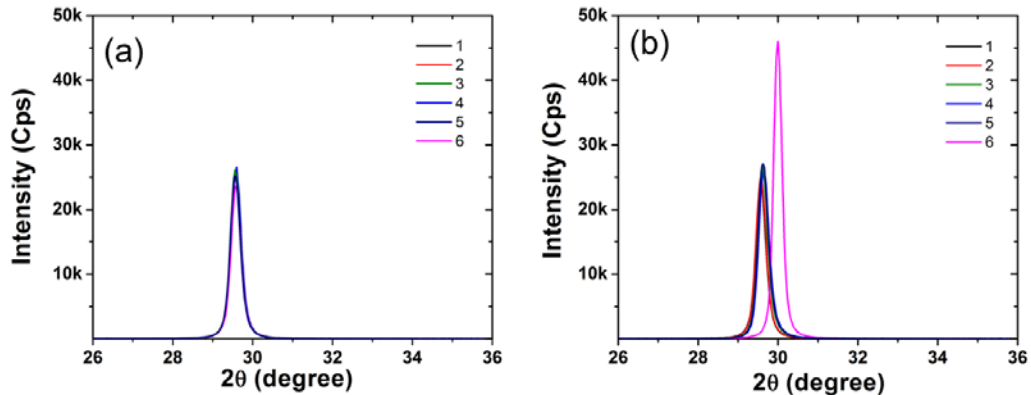


Figure 36 XRD patterns of YSZ thin films as-deposited (a) and after annealing (b).

A post annealing is also believed to change the microstructure of YSZ thin films. Here, a group of 6 samples were post annealed to see the effect of post annealing on the structure of YSZ thin films, more details about post annealing have been given in Section 2.1.2.

Figure 36 shows the XRD patterns of as-deposited and post-annealed YSZ thin films on polished Al_2O_3 . As shown in Figure 36(a), the as-deposited YSZ thin films exhibited similar XRD patterns, which show the cubic phase of YSZ. All films are all strongly oriented in (111) orientation only with a peak location at 29.6° . According to

the Bragg equation [18], the out-of-plane lattice parameters were calculated to be 5.23 - 5.24 Å, as shown in Table 6. Taking the standard lattice parameter of YSZ as 5.14 Å [79], there exists nearly 2% dilation strain in out-of-plane direction. In addition, based on the Scherrer equation [18], the average grain size was around 27 - 28 nm.

Table 6 Lattice parameters and grain sizes for the samples in Figure 36.

No.	Lattice parameter (as-deposited) (Å)	Lattice parameter (after annealing) (Å)	Grain size (as-deposited) (nm)	Grain size (after annealing) (nm)
1	5.23	5.23	27	27
2	5.23	5.23	27	27
3	5.24	5.23	28	28
4	5.24	5.22	28	27
5	5.23	5.22	28	27
6	5.23	5.16	27	33

As shown in Figure 36(b), the annealing may change the XRD pattern. The low annealing temperature of 650 °C, which is same as the deposition temperature made no difference. The mediated annealing temperature of 800 °C (for 5 h, 10 h and 20 h) shifted the peak location right (by 0.04° – 0.06°) and increased the intensity a little bit. More obviously, the high annealing temperature of 1000 °C (for 10 h) shifted the peak location right by 0.4° and increased the intensity 2 times. No difference of

lattice parameter was observed as the film was annealed at 650 °C, even the decrease of lattice parameter at 800 °C (0.01 Å) was negligible. While annealed at 1000 °C, YSZ films obtained a decrease of 0.07 Å in lattice parameter and released the dilation out-of-plane strain. The grain sizes of annealed films kept the same as 27 – 28 nm, just like the as-deposited except that the films annealed at 1000 °C exhibited an increased grain size of 33 nm.

Based on the structural characterization of YSZ thin films, it is found that on MgO (especially on MgO (100) and MgO (111)), the thin films growth is not quite repeatable. However, on Al₂O₃, YSZ thin films achieved a quite repeatable epitaxial growth. YSZ thin films on Al₂O₃ obtained a quite good crystallinity and the grain boundary seemed to be low angle grain boundary with the existence of some edge dislocations.

3.2 Structural Characterization of GDC Thin Films

3.2.1 Structural Characterization of GDC Thin Films on MgO Single Crystal

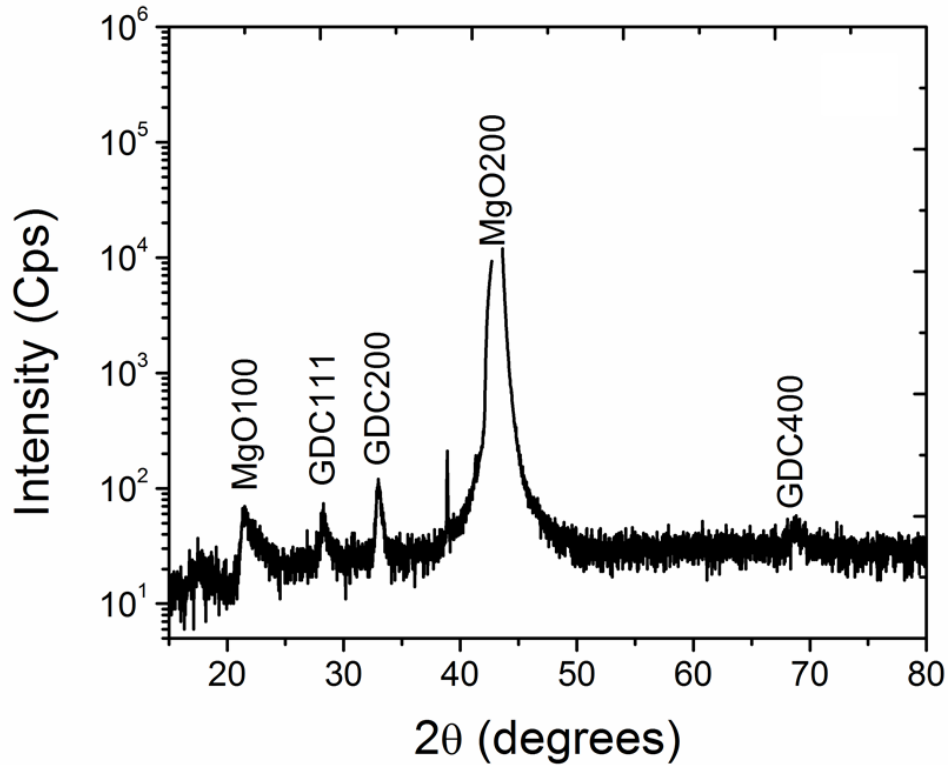


Figure 37 θ - 2θ XRD patterns of GDC film deposited on MgO (100). Reprinted from reference [11].

Besides YSZ thin films, GDC thin films are also interesting solid electrolytes. Just like YSZ thin films, GDC thin films were deposited on both MgO and Al₂O₃ single crystal substrates. The structures of GDC thin films were shown below.

Both MgO (100) and Al₂O₃ (0001) were tested as substrates for epitaxial growth of 20 mol% 75 thick GDC thin films. Figures 37 shows the XRD patterns of

GDC films deposited on MgO (100) substrates. On MgO (100), GDC exhibited only weak peaks along multiple axes, indicative of randomly oriented, nanocrystalline grains. A larger lattice mismatch between MgO and GDC relative to YSZ may be the reason for this kind of growth.

Figure 38 shows the plan view SAED pattern of GDC film (≈ 75 nm) deposited on MgO (100). From the arcs in the SAED pattern, the GDC film is confirmed to be polycrystalline, though not completely randomly oriented. Rotation may occur at the interface between the GDC film and MgO substrate.

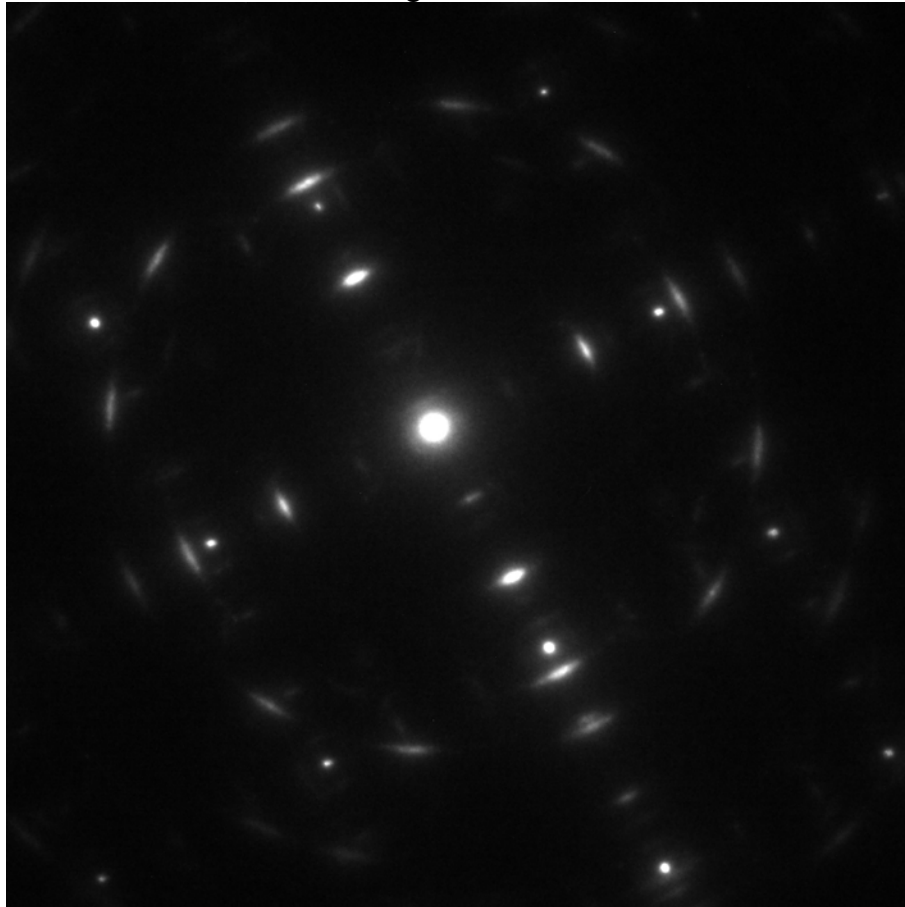


Figure 38 Plan view SAED pattern of GDC films deposited on MgO (100) substrate. Reprinted from reference [11].

The GDC directly deposited on MgO (100) was poorly textured (Figure 37). To see if the textured YSZ layer could be used as a buffer layer for textured GDC film growth on MgO (100), a multilayer of YSZ and GDC films was fabricated. The GDC was deposited on the top surface of YSZ, as shown in the inset of Figure 39. The films were each approximately 75 nm thick. According to the diffraction pattern in Figure 23, both films in this sample were highly oriented along the (100) direction. Thus, the intermediate lattice parameter of YSZ—between that of MgO and GDC—allows the use of YSZ as a buffer layer for oriented GDC film growth.

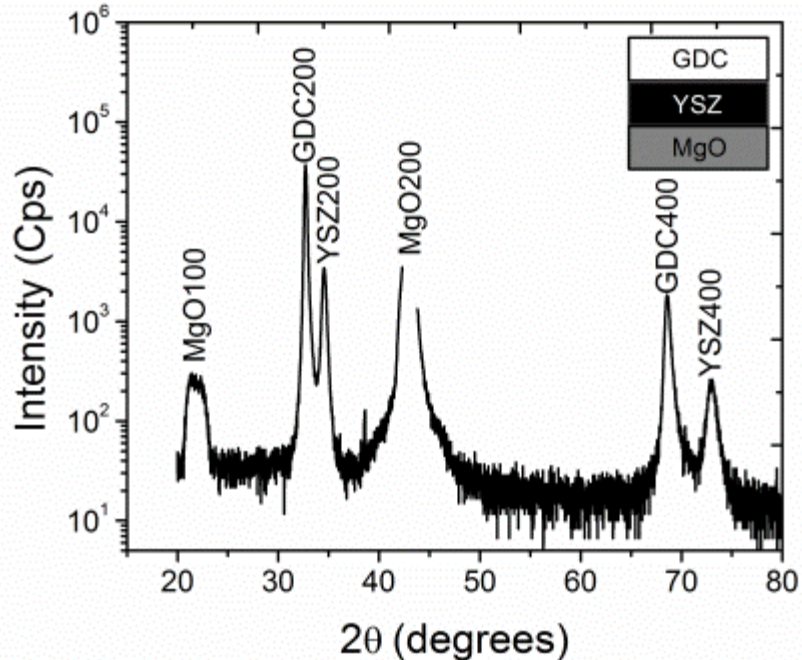


Figure 39 θ - 2θ XRD pattern of a bilayer film of GDC and YSZ deposited on MgO (100). A sketch of the heterostructure is shown in the inset. Reprinted from reference [11].

3.2.2 Structural Characterization of GDC Thin Films on Al₂O₃ Single Crystal

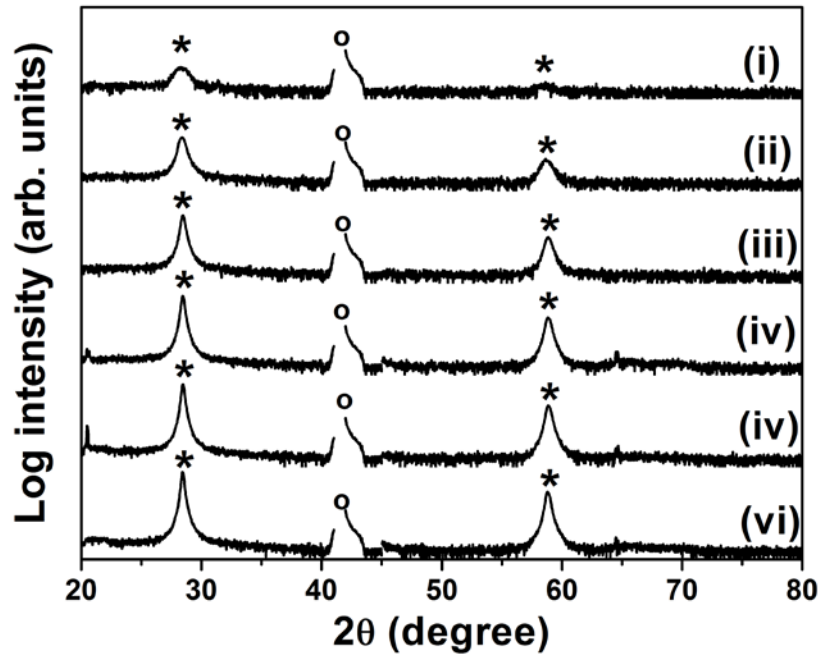


Figure 40 θ - 2θ XRD pattern of GDC thin films with thickness 15 nm (i), 30 nm (ii), 81 nm (iii), 119 nm (iv), 146 nm (v), 173 nm (vi). Note that the plotted intensity is logarithmic. The peaks near 28° and 59° indicated with asterisks represent GDC (111) and (222), respectively; the truncated peak near 43° and indicated with the circle is Al₂O₃ (0006). Reprinted from reference [69].

As shown above, GDC thin films deposited on MgO turns out to be randomly oriented nanocrystalline. Then how about GDC thin films on Al₂O₃?

Typical θ - 2θ XRD patterns of GDC thin films with a thickness of 15 nm, 30 nm, 81 nm, 119 nm, 146 nm and 173 nm are shown in Figure 40. Only (111) and (222) peaks appear for all films regardless of thickness, showing that GDC achieved a stable crystal orientation on Al₂O₃ (0006) despite the high lattice mismatch between the film

and substrate. The thinner films exhibited broader, less intense peaks. This result is consistent with the decreased grain size normal to the diffraction planes that is implied by columnar grains as film thickness is decreased. Alternatively, decreasing crystallinity or increased microstrain (i.e., spread of lattice parameter values) near the substrate interface may also lead to this observed behavior.

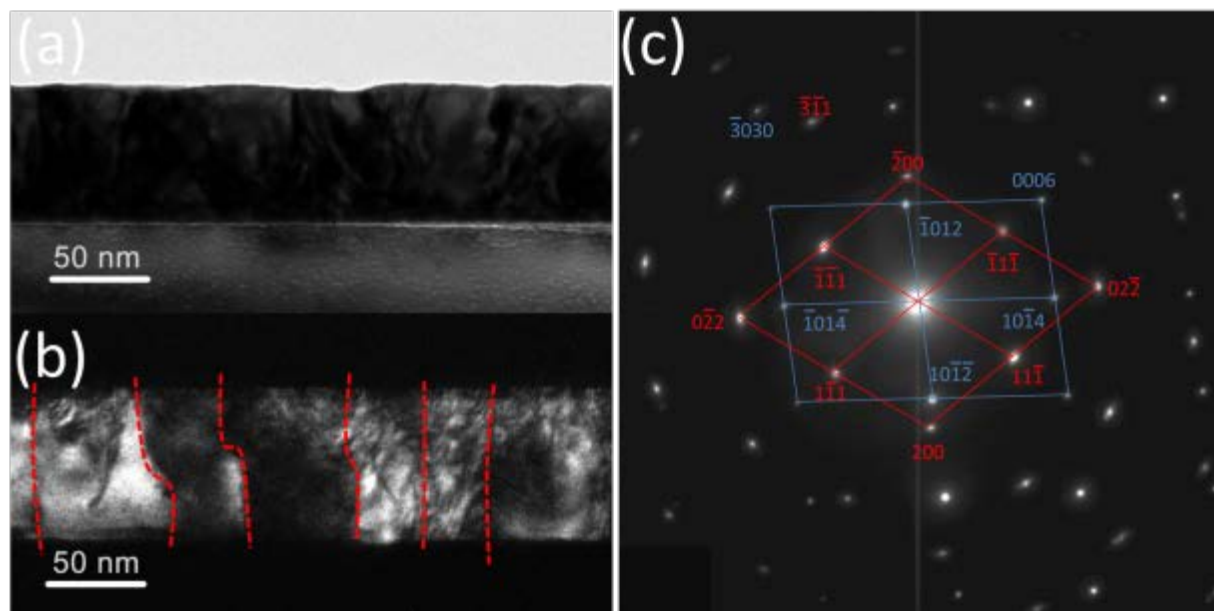


Figure 41 (a) Bright field and (b) dark field (with grain boundaries indicated) TEM images of GDC thin films on Al_2O_3 . (c) Selected area electron diffraction of GDC thin films on Al_2O_3 . Reprinted from reference [69].

Bright field and dark field TEM images of a 75 nm thick GDC thin film on Al_2O_3 are shown in Figure 41(a) and 41(b). The thin films have a columnar microstructure and a lateral grain size of 20 nm – 60 nm. In addition, the contour exhibits distorted grain boundaries as indicated in Figure 41(b) with dashed lines. These distorted grain boundaries seemed to increase through the thickness of the film,

with more distortion at the top surface and less near the substrate interface. In the selected area electron diffraction shown in Figure 341c), GDC (111) aligns with Al_2O_3 (0006) in the out-of-plane direction, which corresponds to the XRD results.

3.3 Electrochemical Characterization of YSZ and GDC Thin Films

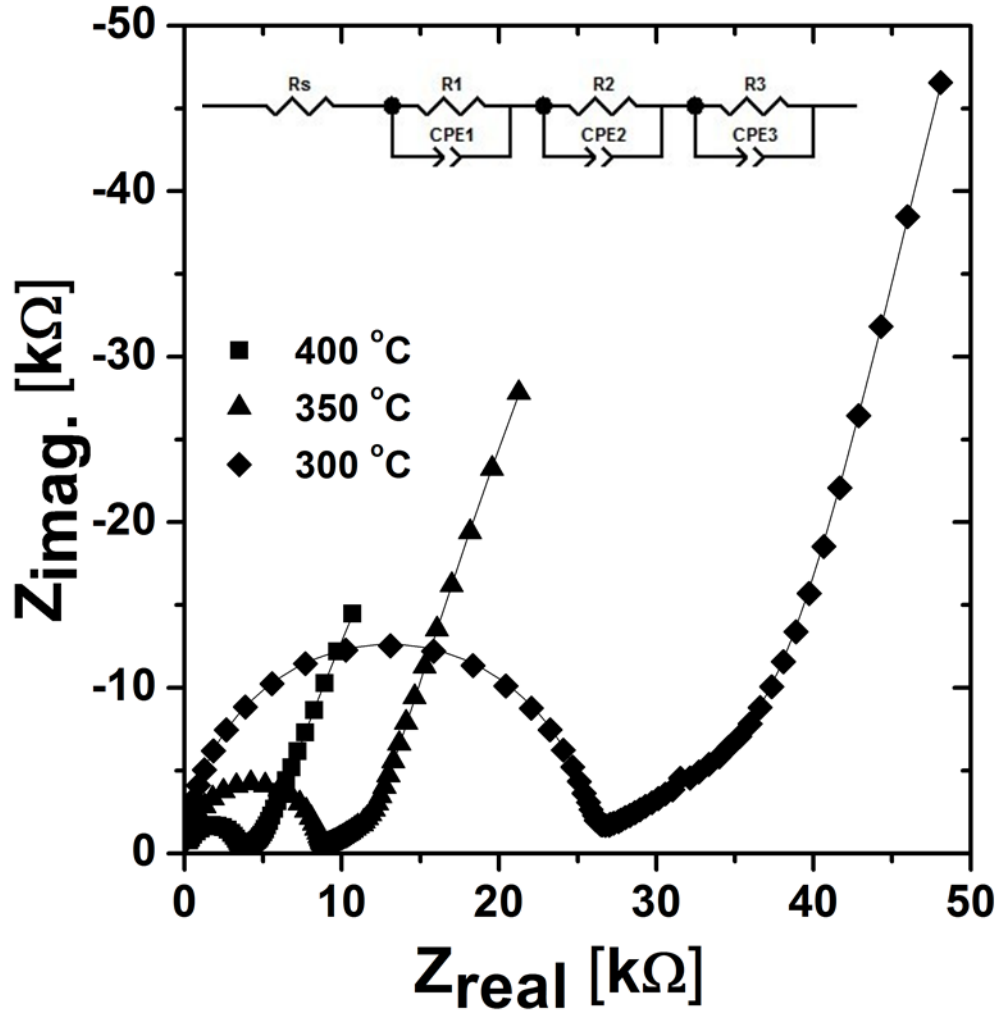


Figure 42 Representative impedance spectra of the 81 nm thick GDC film in air at the temperatures indicated in the plot. The inset shows the equivalent circuit used to fit the impedance spectra (R = resistor, CPE = constant phase element). Reprinted from reference [80].

Typical impedance spectra are shown in Figure 42. Because YSZ and GDC thin films exhibited similar impedance spectra, the analysis of GDC thin film below also works for YSZ thin films. Two semicircular arcs and an intermediate, highly depressed arc were obtained for all impedance spectra. The inset equivalent circuit in Figure 42 was used to fit the impedance spectra. R_s represents the intercept of the first semicircle with x axis. R_s was roughly 100 - 200 Ω for all samples, temperature, and oxygen partial pressures. The electron conduction through the platinum wiring and/or thin film electrodes are the presumed cause of the resistance of R_s . R_1 and constant phase element 1 (CPE1) represent the first semicircle at relatively high frequency. The characteristic exponent of CPE1 was consistently ≈ 1 , indicating that nearly ideal capacitive behavior was observed. CPE1 had a capacitance roughly 10^{-11} F for all samples, temperatures, and oxygen partial pressures and was ascribed to the capacitance of the film, substrate, and air between the electrodes. Joo et al. [81] reported a capacitance of $\sim 10^{-11}$ F for GDC thin films deposited on Al_2O_3 by pulsed laser deposition. The low capacitance of CPE1 corroborates resistor R_1 as the electrolytic resistance of the GDC films, and R_1 is the main concern of this work. As is often the case for nanocrystalline, thin film samples, there is likely to be little ability to discriminate between grain and grain boundary impedance in frequency space. R_2 , R_3 , CPE2 and CPE3 represent the second semicircle and the depressed arc found at low frequencies. Both CPE2 and CPE3 have equivalent capacitances $\geq 10^{-6}$ F. Such high capacitances indicate that these impedance features are due to the surfaces and/or electrodes, which are not of direct interest to this work. Bieberle-Hutter et al. [68] also reported a capacitance of $\sim 10^{-5}$ F for electrodes in the Pt/GDC system. These impedance features were also found on measurements of a YSZ single crystal (with

nominally identical electrodes), so neither is believed to be due to grain boundaries. Examining the data collected here using modulus plots as in reference [82] did not enable distinguishing of grain and grain boundary contributions. R1 was converted to a conductivity using the known film thickness and electrode geometry.

Before measuring the conductivity of YSZ thin films, bare MgO and Al₂O₃ substrates with identical electrodes was measured as a test to ensure that film resistances were always at least an order of magnitude less than that of the substrate. As shown in Figure 43, the resistance of both MgO and Al₂O₃ substrate with No. 2 electrode in Table 4 is above 100000 Ω.

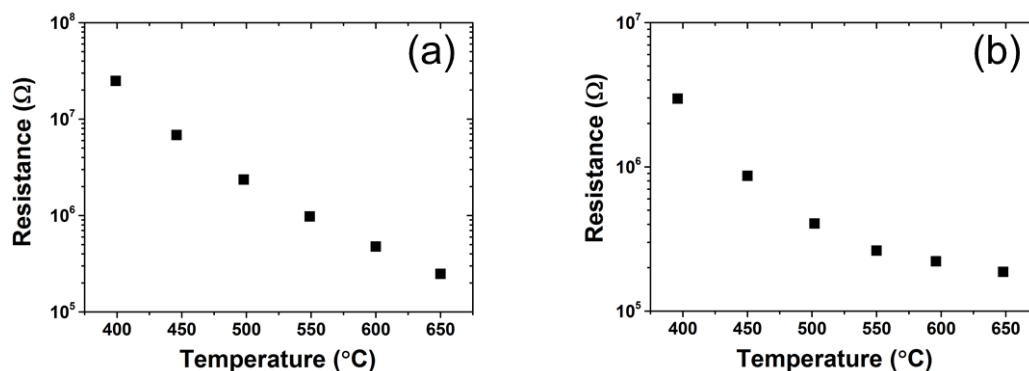


Figure 43 Resistance of (a) MgO and (b) Al₂O₃ substrates with No. 2 Pt electrodes.

3.4 Electrochemical Properties of YSZ Thin Films

3.4.1 Electrochemical Properties of YSZ Thin Films on MgO Single Crystal

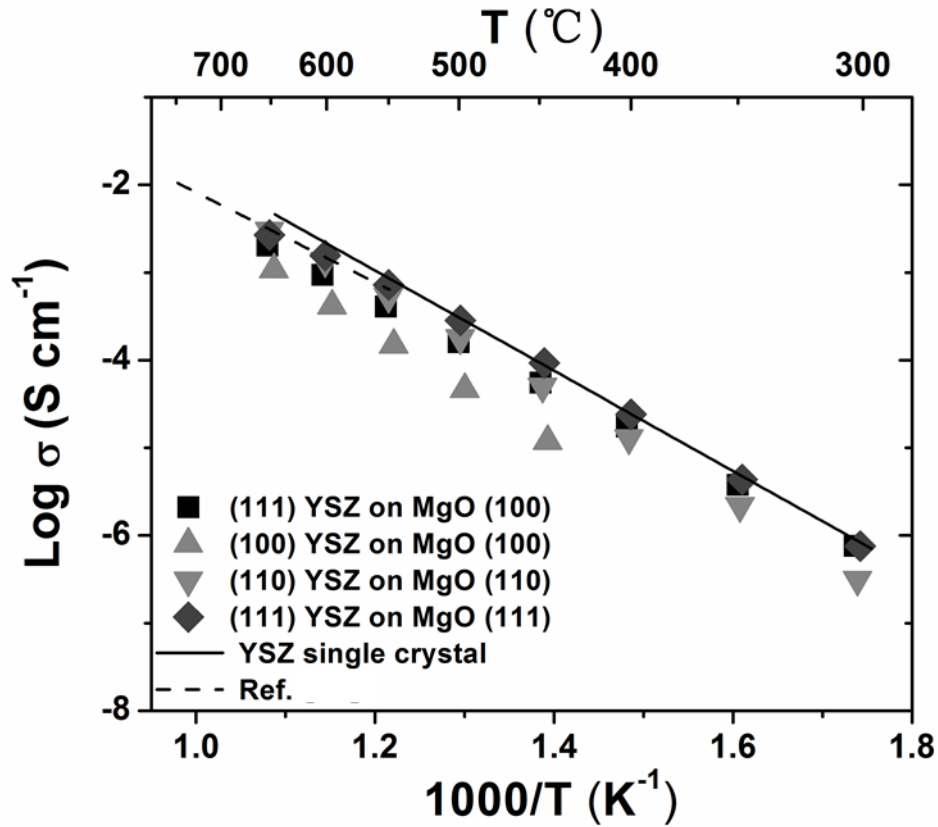


Figure 44 Arrhenius plot of the conductivity of 50 nm thick YSZ thin films ((100) YSZ on MgO (100) has a dopant concentration of 14 mol%; all other films have 9 mol%) as well as a single crystal YSZ substrate with nominally similar composition. The dashed line gives reference values from Guo[33]. Reprinted from reference [73].

The ionic conductivity of 50 nm thick YSZ thin films deposited at 650 °C on MgO (100), MgO (110), and MgO (111) are shown in Figure 44. For comparison, the conductivity of a YSZ single crystal measured in this study and reference data of

polycrystalline YSZ thin films with nanometric grain sizes from Guo et al. [33] are included. The activation energies for every sample are listed in Table 7. The (111) oriented YSZ on MgO (100), (110) oriented YSZ on MgO (110), and (111) oriented YSZ on MgO (111) have the same dopant concentration (9 mol%) and deposition temperature (650 °C). Despite the differences in orientation and, possibly, grain size, crystallinity, residual strain, and other properties, the conductivities of these films were all nearly the same as the reference data or slightly lower. As shown in Table 7, the activation energies ranged between 1.27 eV and 1.09 eV. The (100) oriented film on MgO (100) had significantly lower conductivity and higher activation energy (1.34 eV), but this is most assuredly due to the higher dopant concentration (14 mol%). This effect of dopant concentration is well known [1].

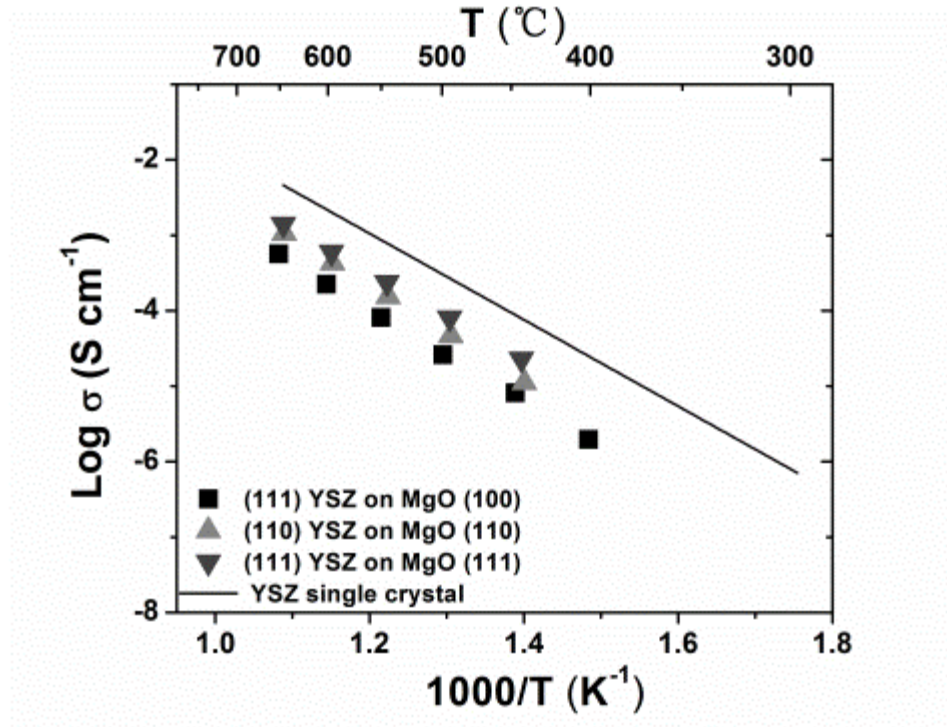


Figure 45 Arrhenius plot of the conductivity of 12 nm thick 9 mol% YSZ thin films as well as a single crystal YSZ substrate with nominally similar composition. Reprinted from reference [73].

Upon decreasing the YSZ thickness from 50 nm to 12 nm, the resistances measured began to approach that of the bare substrates such that the ratio of bare substrate resistance to sample resistance was below 10. In these cases, parallel conduction through the substrate is no longer negligible, and the precision in the determination of film conductivity is reduced. Specifically, if one ignores the current leakage through the substrate, the films may seem to be more conductive than they truly are. Despite this, Figure 45 shows that the overall apparent conductivities of the 12 nm YSZ thin films on MgO (100), MgO (110) and MgO (111) are 3 - 7 times lower compared with that of YSZ single crystal.

Table 7 Sample information in Figure 44 and Figure 45.

Name	Sample	Activation energy	Lattice parameter (as deposited)	Lattice parameter (after high temperature characterization)
50 nm (111) YSZ on MgO (100)	(ii) in Figure 21	1.09 eV	5.247 Å	5.234 Å
50 nm (100) YSZ on MgO (100)	(ii) in Figure 20	1.34 eV	5.217 Å	5.192 Å
50 nm (110) YSZ on MgO (110)	(ii) in Figure 24	1.27 eV	5.216 Å	5.218 Å
50 nm (111) YSZ on MgO (111)	(ii) in Figure 25	1.16 eV	5.257 Å	5.254 Å
12 nm (111) YSZ on MgO (100)	(iii) in Figure 21	1.27 eV	---	---
12 nm (110) YSZ on MgO (110)	(iii) in Figure 24	1.33 eV	---	---
12 nm (111) YSZ on MgO (111)	(iii) in Figure 25	1.22 eV	---	---

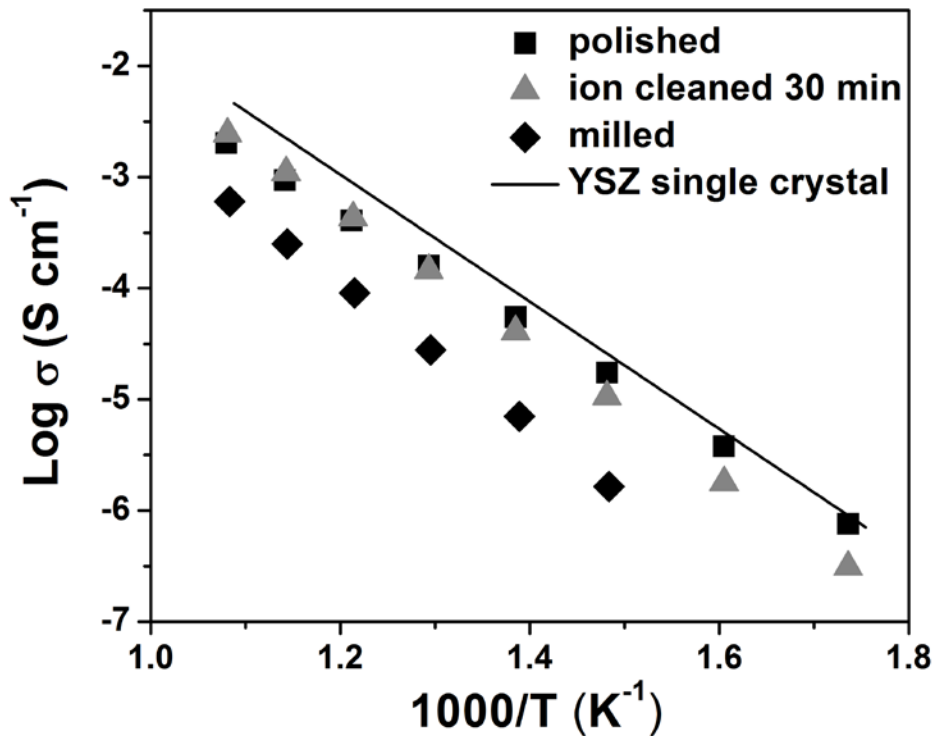


Figure 46 Arrhenius plot of the conductivity of YSZ thin films on MgO (100). Measurements from a single crystal YSZ substrate with nominally similar composition are also provided for reference. Reprinted from reference [76].

Arrhenius plots of the ionic conductivity of 50 nm thick YSZ thin films on different MgO substrate surfaces are shown in Figure 46. The conductivities of YSZ thin films on polished MgO and ion cleaned MgO are close to—though slightly less than—that of a YSZ single crystal. The YSZ thin film on the milled MgO surface exhibited a conductivity nearly 0.5 – 1 order of magnitude less. As mentioned above, 50 nm thick YSZ films on polished MgO (100) substrates exhibited similar ionic

conductivity to a YSZ single crystal, regardless of whether the film was oriented along the (111) or (100) direction or mixed orientations. As shown in Table 8, the activation energy of YSZ on polished MgO was 1.09 eV, lower than the one on ion cleaned MgO (1.26 eV) and the one on milled MgO (1.34 eV). The error of the activation energy determined from repeated measurements of the same sample was less than 0.01 eV.

Table 8 Activation energies of the $\sigma \cdot T$ product of all samples in Figure 46.

No.	Sample	Activation energy (eV)
1	film on polished MgO	1.09
2	film on ion cleaned 30 min MgO	1.26
3	film on milled MgO	1.33
4	YSZ single crystal	1.19

3.4.2 Electrochemical Properties of YSZ Thin Films on Al₂O₃ Single Crystal

Figure 47 shows the conductivity of the YSZ thin films with different thickness on Al₂O₃. All measurements were performed by heating the sample to 650 °C (the same as the deposition temperature) and then measuring the impedance every ≈ 50 °C while decreasing the temperature. Figure 47(a) plots the conductivities of the YSZ thin films during a first measurement after film deposition. The thinner films exhibited higher conductivity and lower activation energy, which ranged from 1.06 eV for the 100 nm thick sample to 0.74 eV for the 6 nm thick sample. Note that the activation energies given are those of the $\sigma \cdot T$ product.

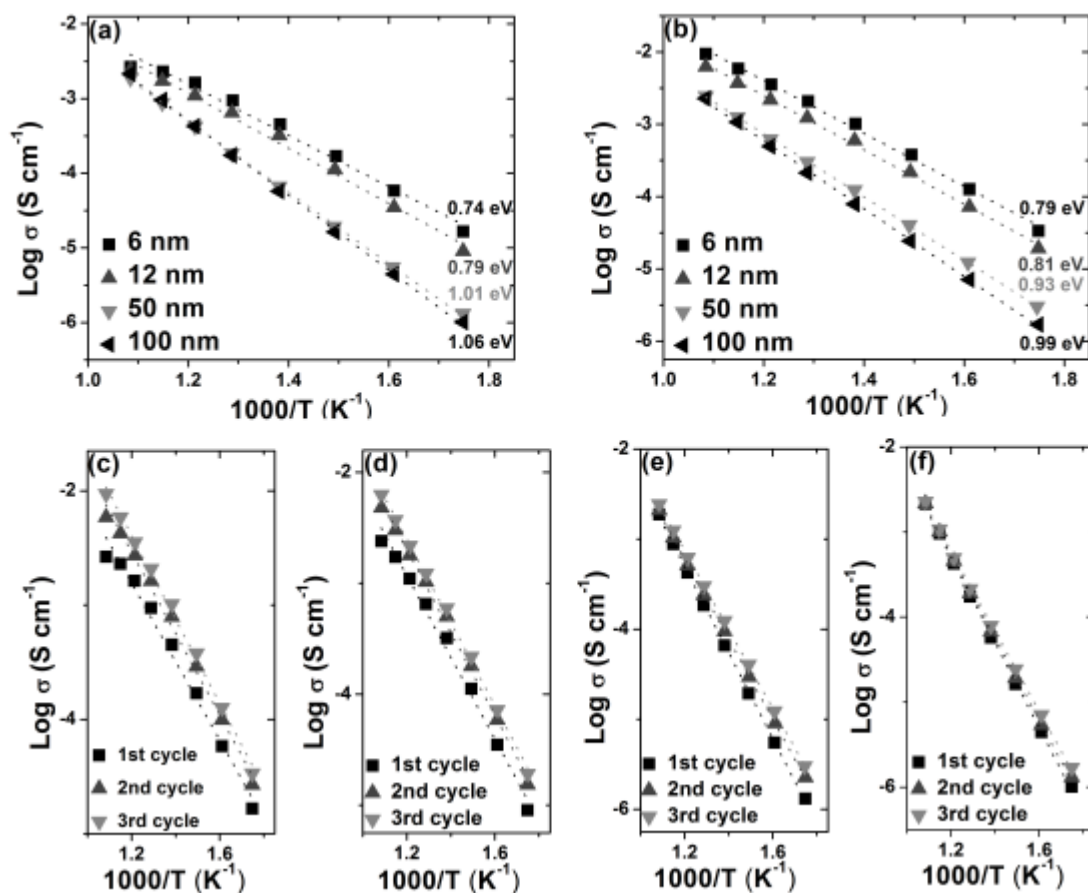


Figure 47 Arrhenius plot of the initial (a) and final (b) conductivity of the 9 mol% YSZ thin films. Also shown is the conductivity evolution during repeated measurement of the film with thickness 6 nm (c), 12 nm (d), 25 nm (e), and 100 nm (f). Reprinted from reference [32].

At the highest measurement temperature, 650 °C, the films all initially exhibited the same conductivity value, but as the measurement continued, the thinner films evolved towards increasing conductivity values. This behavior is apparent as nonlinear Arrhenius conductivity behavior. To further investigate this evolution, the samples were measured over the entire temperature range repeatedly. Figures 47(c)-(f)

show the measured conductivity of each YSZ thin film during the first three measurement cycles. After the third measurement cycle, the samples' conductivities were stable. The conductivity of the 6 nm thick film increased relative to its initial measurement by more than half an order of magnitude. The 12 nm and 50 nm thick films also exhibited increasing conductivity during the measurement, but the relative increase was less. The 100 nm thick film's conductivity was stable during all measurements. Figure 47(b) presents the stable conductivities for the samples measured during the third impedance measurement cycle. Decreasing film thickness yielded higher conductivity and lower activation energy, changing from 0.99 eV for the 100 nm thick film to 0.79 eV for the 6 nm thick film.

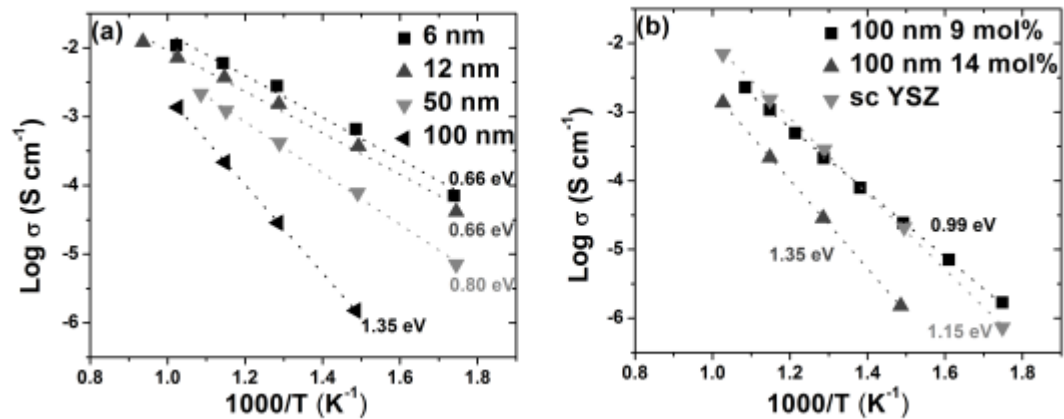


Figure 48 (a) Arrhenius plot of the stable conductivity of 14 mol% YSZ thin films. (b) The temperature dependence of the conductivity of the 100 nm thick 9 mol% YSZ film, the 100 nm thick 14 mol% YSZ film, and a roughly 8 mol% YSZ single crystal. Reprinted from reference [32].

In order to test the effect of dopant concentration, the experiment was repeated with 14 mol% YSZ (lower dopant concentrations were not tried due to concern about

transformation to tetragonal or monoclinic phase zirconia). Figure 48(a) shows the stable conductivity of 14 mol% YSZ films with a thickness of 6 nm, 12 nm, 50 nm, and 100 nm. Similar conductivity evolution behavior was observed at the high measurement temperatures, with the thinner films again increasing in conductivity while the thicker films were stable. The effects of film thickness on conductivity were more dramatic in these films, as the activation energy decreased from 1.35 eV for the 100 nm thick film to 0.66 eV for the 6 nm thick film.

Figure 48(b) compares the conductivity of the 100 nm thick films with 9 mol% and 14 mol% YSZ composition as well as, for reference, a roughly 8 mol% YSZ single crystal. The YSZ single crystal measured here exhibited similar magnitude and activation energy for the conductivity with literature values for such samples. The 100 nm thick 9 mol% YSZ film had similar conductivity values to the single crystal and behaved like bulk YSZ, though with a slightly reduced activation energy. The 100 nm thick 14 mol% YSZ had lower conductivity and higher activation energy. This behavior is expected since ~8 mol% dopant is known from bulk studies to provide the optimal conductivity, with activation energy increasing with the dopant content. Thus, in this work, the 100 nm thick films have conductivity behavior similar to bulk samples while the thinner films deviate from expectation.

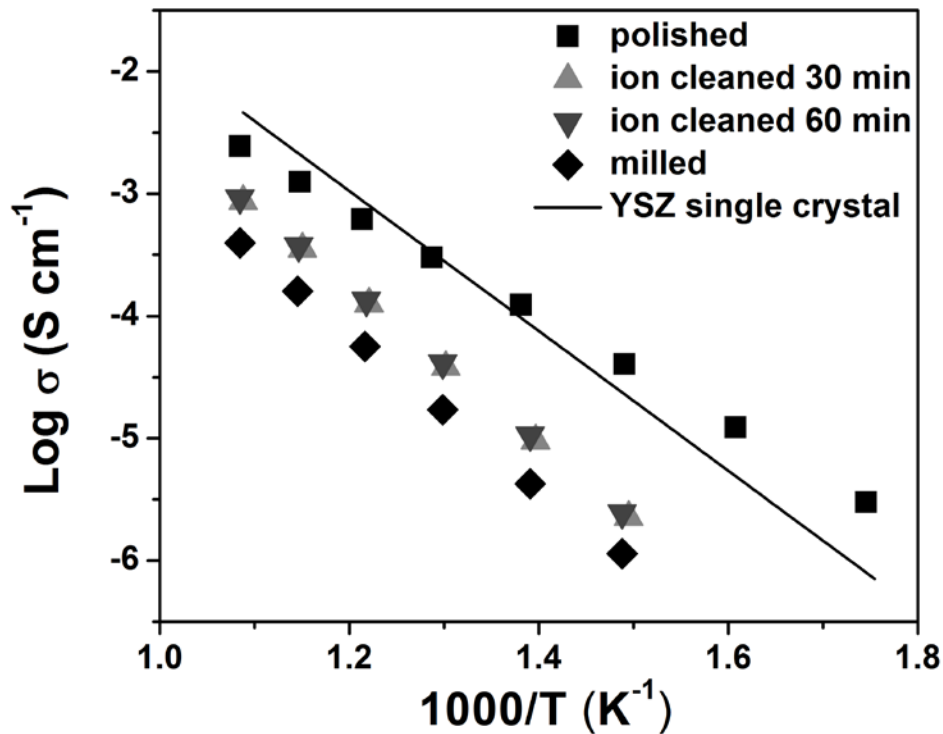


Figure 49 Arrhenius plot of the conductivity of YSZ thin films on Al_2O_3 (0001). Measurements from a single crystal YSZ substrate with nominally similar composition are also provided for reference. Reprinted from reference [76].

Arrhenius plots of the ionic conductivity of 50 nm thick YSZ thin films on different Al_2O_3 substrate surfaces are shown in Figure 49. YSZ films on polished sapphire exhibited a conductivity close to the YSZ single crystal though with a slightly reduced activation energy. In contrast, films on ion cleaned Al_2O_3 had a conductivity 4 times less. This result did not change with different ion cleaning times. On a milled Al_2O_3 surface, the conductivity of YSZ thin film was reduced even

further to roughly 1 – 1.5 orders of magnitude lower compared with YSZ single crystal. The activation energy of films on ion cleaned and milled sapphire was nearly the same at 1.32 eV, which is quite close to the activation energy of films on milled MgO as mentioned above.

Table 9 Activation energy of the $\sigma \cdot T$ product of all samples in Figure 49.

No.	Sample	Activation energy (eV)
4	film on polished sapphire	0.99±0.026 ^a
5	film on ion cleaned 30 min sapphire	1.32
6	film on ion cleaned 60 min sapphire	1.33
7	film on milled sapphire	1.32
8	YSZ single crystal	1.19

^a Unless indicated, the measurement error of the activation energy based on repeated measurement of single samples was less than 0.01 eV.

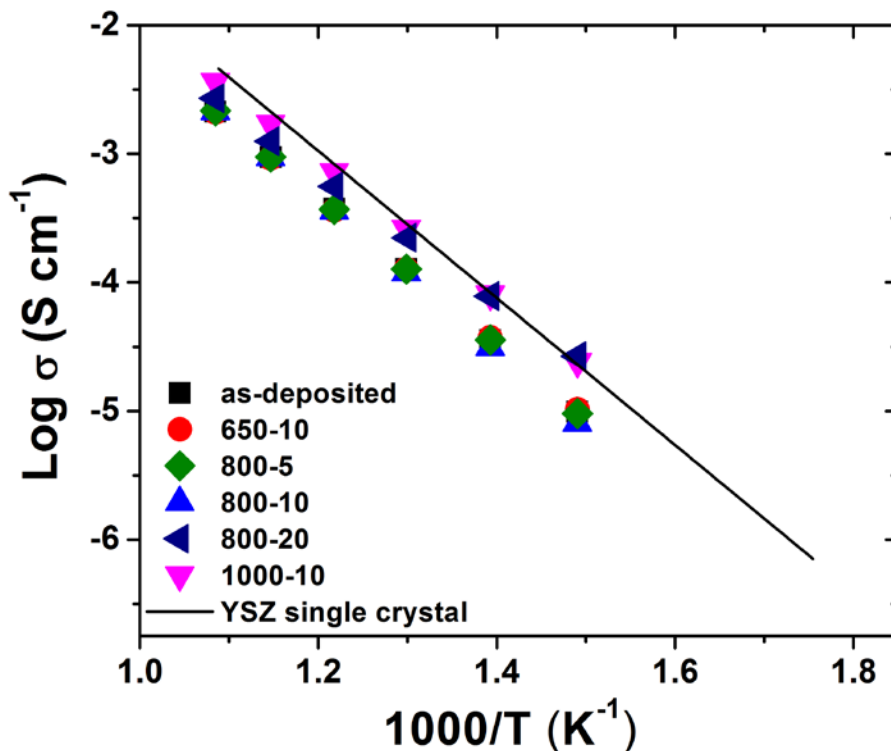


Figure 50 Arrhenius plot of the conductivity of YSZ thin films as deposited and annealed. Measurements from a single crystal YSZ substrate with nominally composition of 8 mol% are also provided for reference.

The ionic conductivities of fresh and annealed samples are shown in Figure 50. For comparison, the conductivity of a YSZ single crystal measured in this study is included. The as-deposited film obtained a conductivity nearly 2 times lower compared with YSZ single crystal. The annealing of 650 °C for 10 h made no difference on the conductivity magnitude. The annealing of 800 °C for 5 h and 10 h did not change the conductivity magnitude, either, while increasing the annealing time to 20 h increased the conductivity of films especially at lower temperatures. The film

annealed at 800 °C for 20 h exhibited a conductivity close to the YSZ single crystal although the value at high temperatures was still a little bit lower. The annealing of 1000 °C for 10 h increased the conductivity further, which was nearly the same as that of the YSZ single crystal.

Table 10 Activation energies for the samples in Figure 50.

No.	Activation Energy (eV)
1	1.23±0.005
2	1.20±0.012
3	1.26±0.002
4	1.12±0.012
5	1.18±0.012
6	1.02±0.023
YSZ single crystal	1.19±0.004

As shown in Table 10, the activation energies of samples were listed. The activation energy of 1.23 eV for as-deposited films was quite close to that of YSZ single crystal (1.19 eV). The annealing of 650 °C for 10h and of 800 °C for 5 h and 10 h did not change the activation energy too much. Increasing the 800 °C annealing time further to 20 h decreased the activation energy significantly to 1.02±0.02 eV. The

annealing of 1000 °C for 10 h decreased the activation energy, too and the reduced activation energy was just 1.12 ± 0.01 eV.

3.5 Increased Conduction of YSZ Thin Films in Humid Air

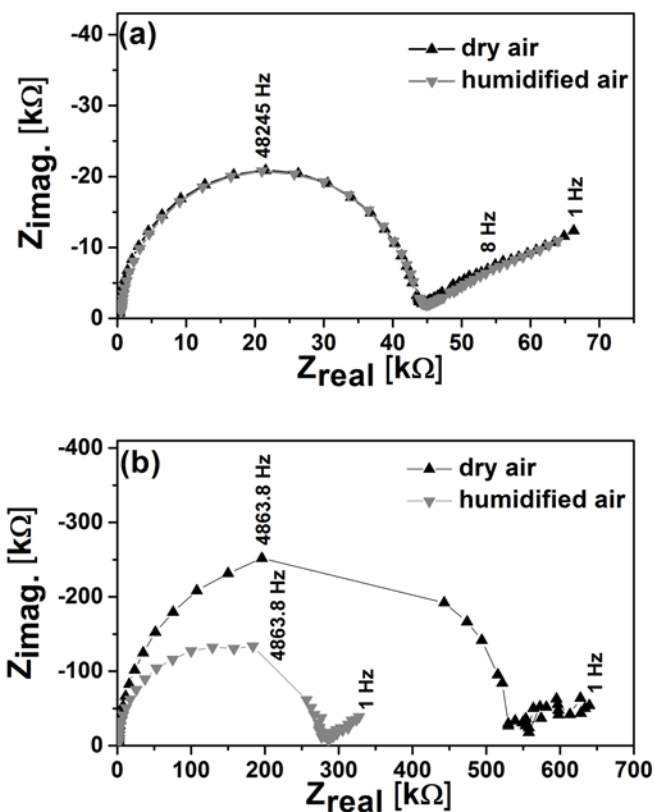


Figure 51 Impedance spectra of the 50 nm (a) and 6 nm (b) thick films in both dry air and humidified air near 500 °C. The measurement frequency of a few data points are indicated. Note that the scale is different in plots (a) and (b). The gaps in data in the upper-right portions of the semicircles in plot (b) are due to an inability to collect low-noise measurements at frequencies near 3500 Hz (a repeatable interference from an unknown source).

In this study, it is interesting to see an increased conductivity of ultra-thin YSZ thin films in humid air. Representative impedance spectra are shown in Figure 51. The 50 nm thick film has almost identical impedance in both dry and humidified air at 500 °C. Conversely, the 6 nm thick film exhibited a resistance in humidified air roughly half of that in dry air (Figure 51(b)).

With the known electrode geometry and film thickness, the resistance obtained from equivalent circuit fitting of the impedance spectra is converted to the conductivity. Figure 52(a) presents the conductivity of the 50 nm thick YSZ thin film in both dry and humidified air. Over the entire measured temperature range (350 °C - 650 °C), the conductivity measured in humidified air was nearly same as that in dry air, whose magnitude was also similar to that of a YSZ single crystal. The activation energies in both dry and humidified air are 1.14 eV, close to that of a YSZ single crystal (1.19 eV). Below 350 °C, the impedance is out of the measurement range of the spectrometer. The similarity in both dry and humidified air strongly suggests that proton conduction in the 50 nm thick YSZ film is negligible. Electron/hole conduction is expected to be negligible based on the wide electrolytic domain of YSZ [1]. Pure oxide ion conductivity in these films is strongly supported by similarity of the measured conductivity to that of a YSZ single crystal.

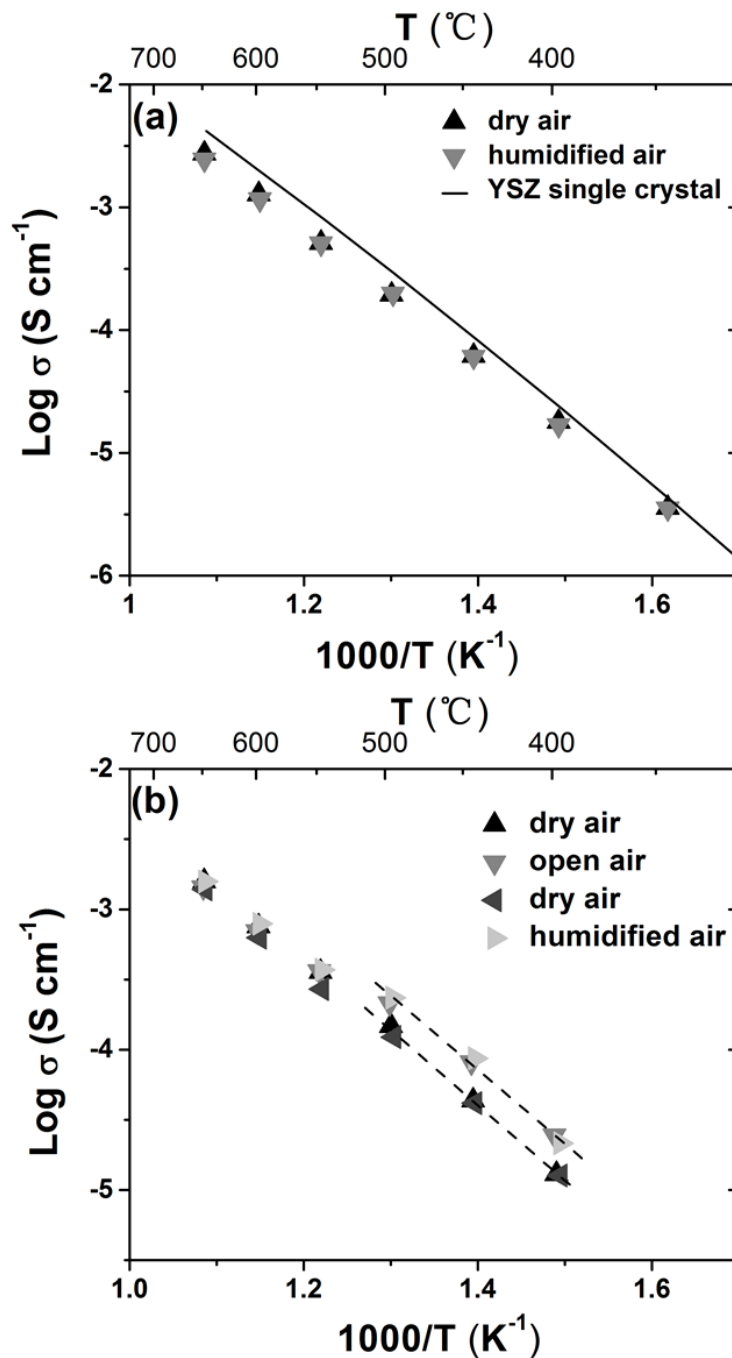


Figure 52 Arrhenius plot of the conductivity of (a) the 50 nm thick YSZ thin film measured in flowing dry air and humidified air with a water vapor partial pressure of 32 mbar and (b) the 6 nm thick YSZ thin film measured in flowing dry air, open lab air, and humidified air with a water vapor partial pressure of 32 mbar.

As shown in Figure 52(b), the conductivities of the 6 nm thick films are nearly the same in dry and humidified air at temperatures above 550 °C. The activation energies are 1.03 eV, slightly lower than that of 50 nm thick film (1.14 eV). Below 500 °C, the 6 nm thick film exhibited a conductivity in humidified air twice the value of that in dry air. The activation energy in humidified air is 1.09 eV, while the value in dry air is 1.13 eV. Below 400 °C, the impedance of this film falls out of the measurable range. In the temperature range of 400 °C – 500 °C, the 6 nm thick film exhibited an increased conductivity in humid air relative to that in dry air. This result suggests that the conductivity in the humidified air is a mixed oxygen ion and proton conduction; however, the conductivity in dry air is predominantly due to oxygen ion conduction over the entire measured temperature range.

The conductivity increase in the presence of water is reversible. Figure 52(b) shows two sets of measurements in dry air. These measurements were taken before and after the measurements in open lab air, and the measurement in flowing, humidified air occurred after that. As can be seen in the plot, the conductivity reversibly changed back-and-forth between the values in flowing dry air and the values in humid air.

3.6 Electrochemical Properties of GDC Thin Films

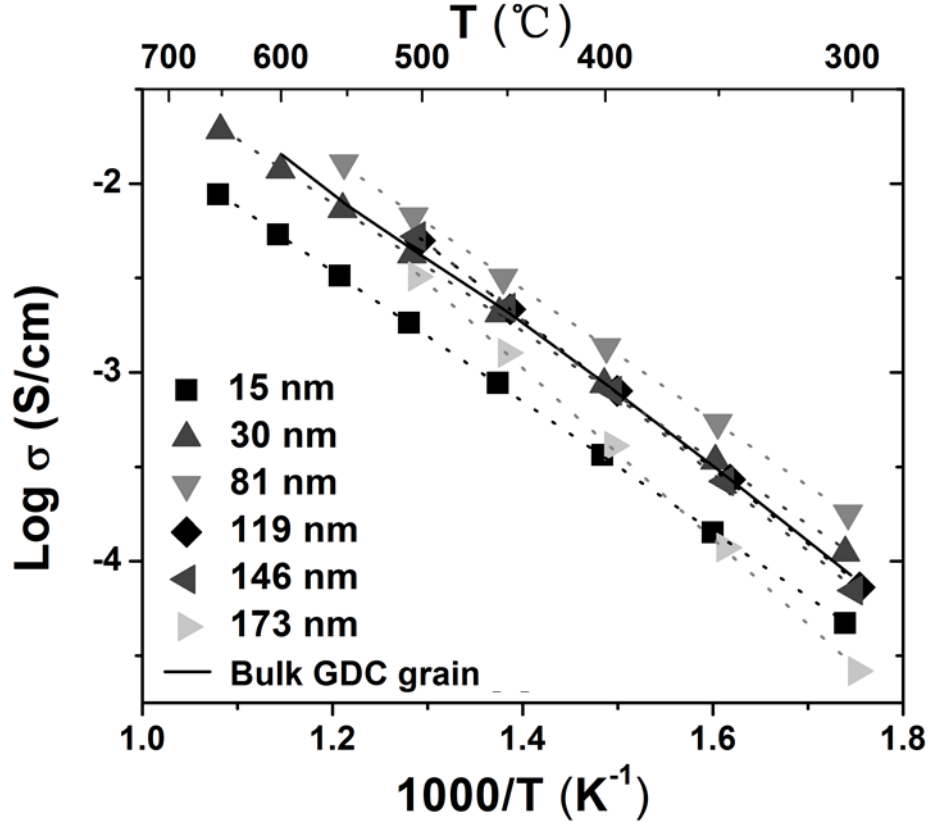


Figure 53 Arrhenius plot of conductivity of GDC thin films with thickness of 15 nm, 30 nm, 81 nm, 119 nm, 146 nm, 173 nm. Solid line represents the literature value for the grain conductivity of the bulk GDC [81]. Reprinted from reference [69].

An Arrhenius plot of the conductivity for GDC films is shown in Figure 53. Over the range of temperatures measured here, the conductivity increased with increasing thickness up to a thickness of 81 nm and then decreased as the thickness increased further. Literature data [81] for the grain conductivity of 20 mol% GDC bulk is also shown for comparison. The 30 nm thick GDC thin film has both conductivity magnitude and activation energy similar to the bulk GDC grain.

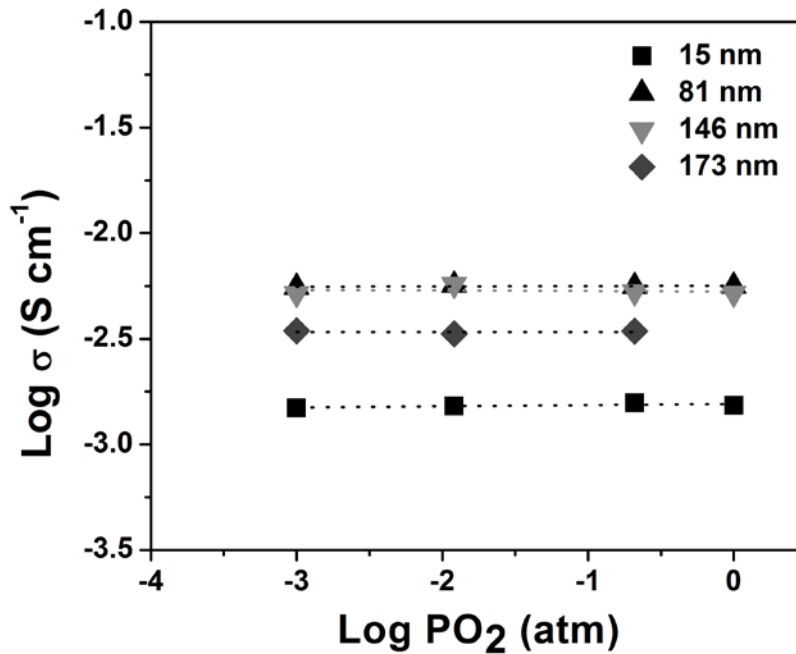


Figure 54 The oxygen partial pressure dependence of conductivity of GDC thin films with thickness of 15 nm, 81 nm, 146 nm and 173 nm at 500 °C. Reprinted from reference [69].

It is not expected that there is significant electron conduction at these temperatures and oxygen partial pressures for GDC thin films. Suzuki et al. [66] prepared nanocrystalline 20 mol% GDC thin films with a grain size of 36 nm on sapphire substrate using a spin coating technique and found there was no pO_2 dependence down to the oxygen partial pressure of 10^{-5} atm in the temperature range of 600 °C – 900 °C. Nevertheless, thin films prepared using different techniques may exhibit different microstructure and defect concentration may be altered near grain boundaries in ceria, so we chose to verify that our results represent ionic conduction. The oxygen partial pressure dependence of conductivity of GDC thin films with

thickness of 15 nm, 81 nm, 146 nm and 173 nm is shown in Figure 54. These thin films were measured in pure O₂, air, 1.2 % O₂ and 0.1 % O₂. The conductivities were essentially constant for all samples under the entire range of oxygen partial pressures. This result proves that the conductivity measured is ionic conduction with vacancy concentration fixed by the dopant content rather than electronic or mixed ionic and electronic conduction.

Chapter 4
DISCUSSION

4.1 Role of Strain on Oxygen Ion Conduction in Zirconia- and Ceria-based Thin Films

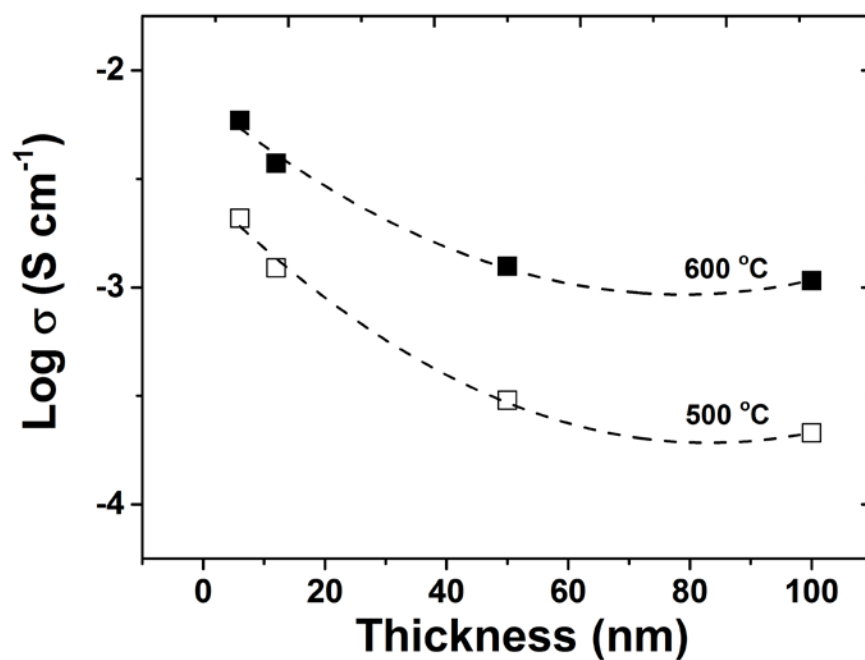


Figure 55 The thickness dependence of conductivity of YSZ thin films on Al_2O_3 .

Figure 55 shows the thickness dependence of conductivity of YSZ thin films on Al_2O_3 based on Figure 47(b). The conductivity of YSZ thin films increases with decreasing thickness and the increase is nearly 1 order of magnitude. Figure 29 shows

the lattice parameter (lattice strain) increases with decreasing thickness. Figure 29 and 55 together suggest it seems to be lattice strain increasing the ionic conductivity.

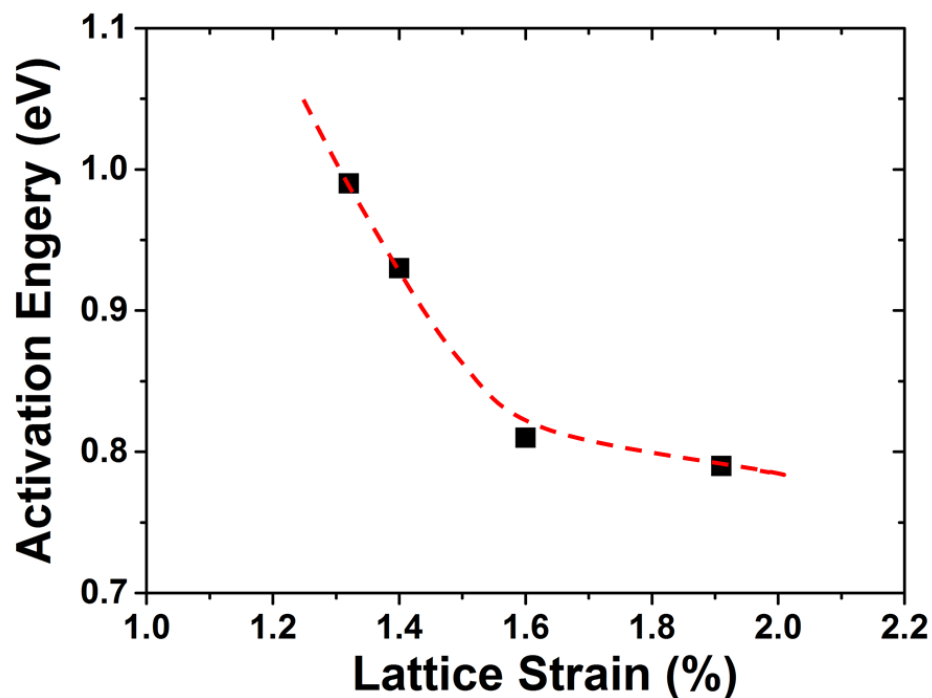


Figure 56 The relationship between lattice strain and activation energies

Figure 56 shows the relationship between lattice strain and activation energies based on Figure 47(b). Obviously, the increasing lattice strain decreases the activation energy, which supports that the lattice strain decreases the activation energy therefore increasing the ionic conductivity based on Equation 4.

From electron diffraction measurements as shown in Figure 33, the ratio of the distances of the sapphire and YSZ patterns provides a way to determine the strained YSZ lattice parameter. The lattice parameter of sapphire was assumed to remain at bulk values ($a = 4.758 \text{ \AA}$, $c = 12.99 \text{ \AA}$). Using this technique, the as-deposited 50 and

6 nm thick films had effective lattice parameters of 5.11 Å and 5.10 Å parallel to the substrate and 5.19 Å and 5.21 Å perpendicular to the substrate. After annealing, the lattice parameters of 6 nm thick film changed to 5.09 Å and 5.22 Å, respectively. Thus, compression in the (110) planes seemed to cause Poisson's-type dilation of the (111) planes. The lattice parameter values determined by electron diffraction are offset from those determined by XRD; it is not clear if this is due to TEM sample preparation or an uncompensated dilatative lattice strain in the substrate near the film interface. Note that the unit cell volume remained equal to the expected value for cubic YSZ: $5.11 \times 5.11 \times 5.19 = 5.10 \times 5.10 \times 5.21 = 5.09 \times 5.09 \times 5.22 = 5.14 \times 5.14 \times 5.14$.

The thinnest 9 mol% YSZ films reported here achieved increased conductivity of roughly half an order of magnitude at 650 °C and 1.5 orders of magnitude at 300 °C, much lower than the 8 order of magnitude enhancement reported by Garcia-Barriocanal et al.[39]. The activation energy in the present work is as low as 0.79 eV for standard YSZ composition. Decreased activation energies were also reported by Sillassen [40], but with nearly three orders of magnitude conductivity enhancement. As the samples measured here consist of YSZ films on sapphire substrates, conductivity contributions from electronic charge carriers in the substrate (e.g., STO) are negligible. It is also unlikely that the films measured here were chemically reduced. The sputtering environment had an oxygen partial pressure greater than 10^{-6} atm, but the concern may still be raised that the films were incompletely oxidized upon deposition. If so, the films would nevertheless rapidly and fully oxidize when heated in air at 650 °C before the conductivity measurements. Further, if the improved conductivity found in the thinner films were due to chemical reduction, then their conductivity would be expected to decrease upon holding at high temperature in air.

In fact, the opposite behavior was found with conductivity increasing each measurement cycle.

The evolution of the conductivity in the thinner films is believed to be due to the recrystallization and introduction of in-plane edge dislocations witnessed in the HR-TEM. From Figure 32(b) and 32(c), the as-deposited 6 nm thick films had significantly defected regions that reduced in size or were eliminated by the in situ heat treatment during impedance measurement. Similar recrystallization behavior was reported by Sankaranarayanan [83]. As the deposition rate of the films here was 25 nm/h, the 6 nm thick films were deposited in about 15 minutes while the 100 nm thick films took about 4 hours to deposit. Therefore, the 6 nm films experienced the 650 °C deposition temperature for a much shorter time than the thicker films. The thinner films thus contained more highly defected regions that were annealed away during the subsequent measurements at 650 °C. The thicker films, on the other hand, experienced the 650 °C temperature for a considerable length of time during deposition and thus were much more stable during subsequent measurements.

Recent theoretical and experimental reports suggest that tensile strain increases the oxygen ion conductivity of YSZ. Using multilayer films, Schichtel et al. have proposed that for an oxygen-ion conductor with vacancy charge carriers (positive migration volume), dilatative strain (negative pressure) will increase the conductivity along the strained region, while compressive strain (positive pressure) will decrease the ionic conductivity [41, 58]. Recently, Kushima [55] predicted an enhancement of oxygen diffusivity in biaxially tensile strained 9 mol% YSZ using kinetic Monte Carlo simulations at different temperature and strain states. According to that work, tensile strains between 0% and 4% result in progressively increasing conductivity and

decreasing activation energy. Increasing the tensile strain from 1% to 2%, as is suggested by the change in lattice parameter of the films reported here when decreasing the thickness from 100 nm to 6 nm, is suggested to increase the conductivity by a factor of around 5 at 800 K and 7 at 600 K.

The results presented here correspond well to these expectations. Figure 47(b) shows conductivity improvements of about an order of magnitude at 500 °C and one order and a half of magnitude at 300 °C when the thickness decreased from 100 nm to 6 nm. The XRD and TEM results show that the thinner films are more highly strained – likely because the strains were caused by the YSZ/Al₂O₃ interface, and the thinner films had more material in proximity to this interface. Still, unlike the reports from Schichtel et al. and Kushima et al., here the dilation occurs in the direction perpendicular to the substrate. Kushima et al. do not specifically discuss this configuration, but the suggestion from that work was that dilation decreased the ion migration barrier largely by weakening the oxygen-cation bond strength. The large amount of uniaxial dilation found here likely serves to decrease the bond strength in a similar manner. The added effects of the edge dislocations found in the 6 nm thick films are unknown, but Otsuka et al. [84] demonstrated that ionic conductivity of YSZ can be enhanced by introducing high density of dislocations. Thus, the dislocations in the thinner films may be increasing further the conductivity by serving as a fast in-plane ionic conduction pathway.

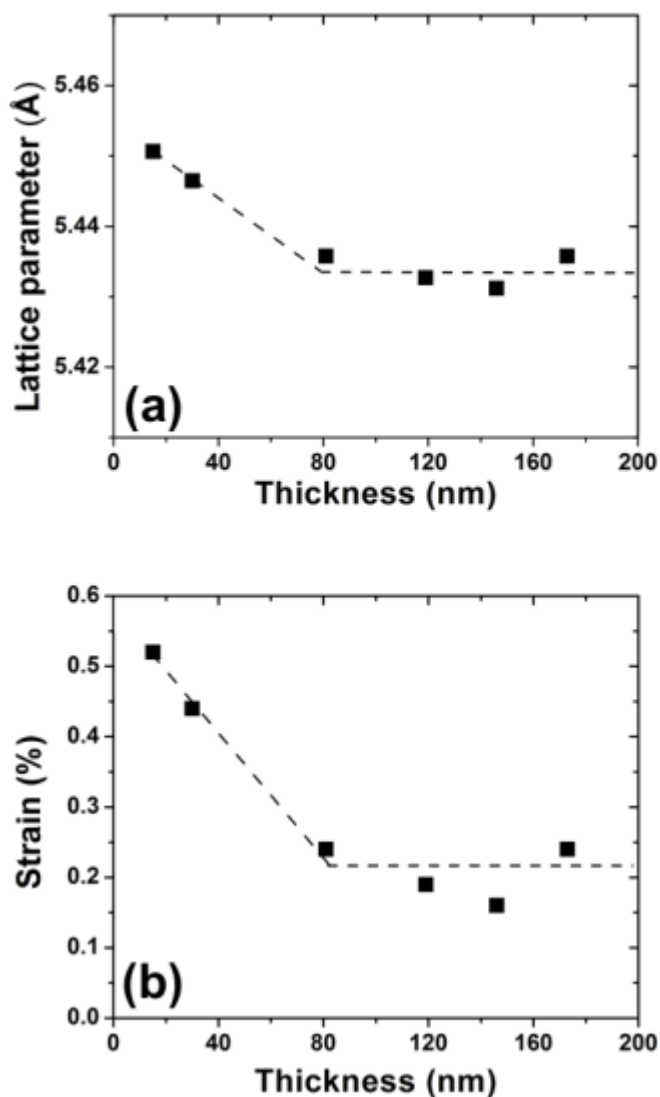


Figure 57 (a) The out-of-plane equivalent lattice parameter of GDC thin films on Al₂O₃ determined from XRD and (b) The out-of-plane strain of GDC thin films on Al₂O₃ determined from XRD. Reprinted from reference [69].

For GDC thin films on Al_2O_3 mentioned above (Figure 40), according to the (111) peak locations in the XRD patterns, the effective lattice parameters in the out-of-plane direction were calculated and are shown in Figure 57(a). The thicker films obtain a similar lattice parameter close to 5.43 Å, while the films less than 81 nm thick have higher values close to 5.44 Å and 5.45 Å. Zha et al. [85] synthesized bulk ceramic GDC solid solutions with varying dopant concentration using an oxalate coprecipitation process and measured the lattice parameter for 20 mol% GDC as 5.4226 Å. Based on this value, the strain (lattice parameter mismatch) was calculated as shown in Figure 57(b). The strain was 0.2 % for thicker films and 0.5 % for the thinnest films. The strain was much less than the 1 % to 2 % strain found for YSZ films deposited under nearly identical conditions (Figure 29). If the lattice parameters of the thicker films instead were taken as the standard value in our work, the strain would be nearly 0 for all of the thicker films and around 0.3 % for thinner films.

The thickness dependence of the conductivity at 500 °C and the activation energy of the $\sigma \cdot T$ product for the GDC films are shown in Figure 58(a) and 58(b). At 500 °C, the 81 nm thick film exhibited the highest conductivity. The activation energy was around 0.75 eV for the films with thickness ≤ 81 nm and increased with increasing thickness for the films thicker than 81 nm. The activation energy of the thicker films dropped significantly after aging. The activation energy of 146 nm thick films changed from 0.87 eV to 0.81 eV and that of 173 nm thick films changed from 0.96 eV to 0.89 eV.

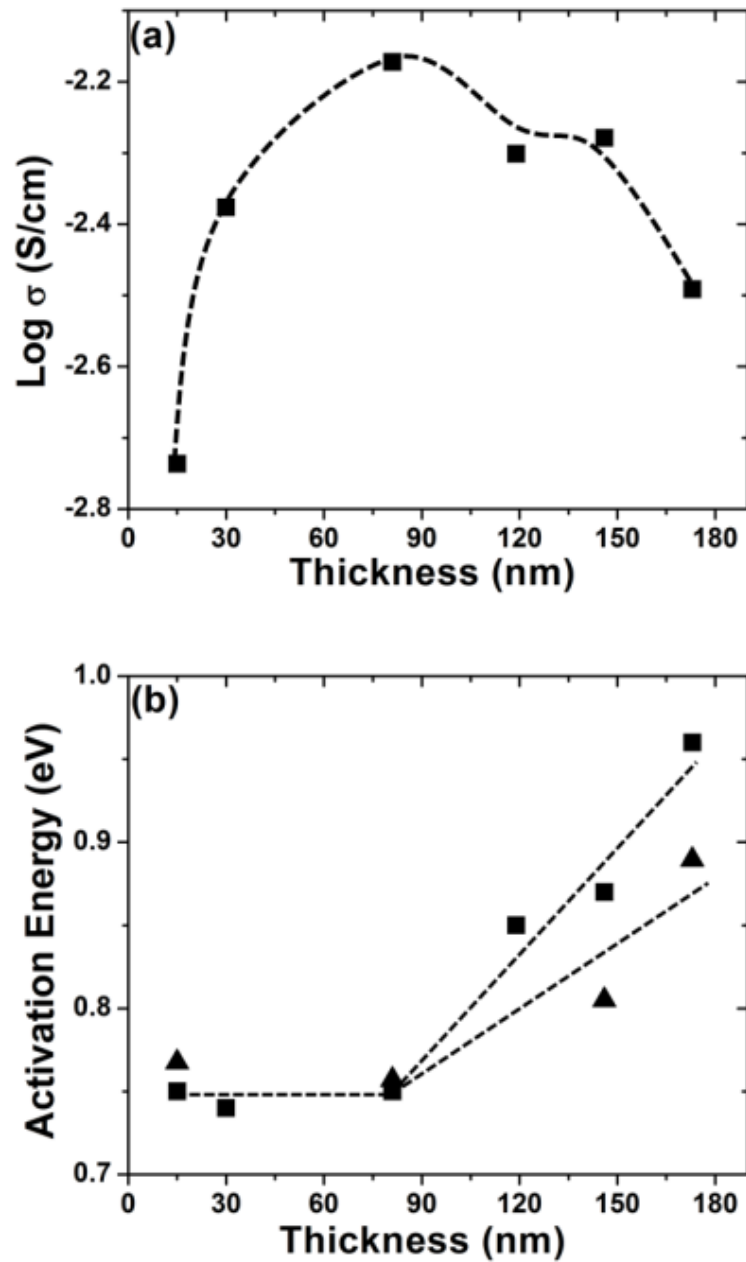


Figure 58 The thickness dependence of the (a) conductivity at 500 °C and (b) activation energy of the $\sigma \cdot T$ product (squares represent fresh samples, triangles represent annealed samples). Reprinted from reference [69].

For the (111) oriented GDC thin films on Al_2O_3 (0001), a moderate amount of strain existed for GDC thin films thinner than 81 nm, similar to the grain size. Unlike the behavior found for YSZ films, strain does not seem to play much role in the GDC films studied here, since the activation energy is not reduced significantly from what is expected from bulk material grain conduction. In addition, the reduction in activation energy for the thinnest films is not likely to have much utility, given that not only the activation energy but also the pre-exponential factor (and thus the conductivity) decreased for the thinnest films. Compared with the relaxed thicker films, the thinner films hold moderate dilatative out-of-plane strain, which presumably arises from substrate-induced compressive in-plane strain. A correlated in-plane compression with out-of-plane dilation, as expected from Poisson's ratio-type considerations, was found conclusively in the YSZ films deposited under identical conditions. Based on Schichtel et al.'s work [41, 58], for an oxygen-ion conductor with vacancy charge carriers, a positive migration volume means that dilatative strain (negative pressure) will increase the conductivity along the strained region, while compressive strain (positive pressure) will decrease the ionic conductivity. In-plane and out-of-plane strains with opposite polarity may thus yield non-monotonic conductivity behavior. As opposed to the previous work on YSZ, where in-plane compression yield very large out-of-plane dilation and correlated with increased conductivity, the moderate out-of-plane dilation found in nanoscale GDC films here is insufficient to create any effective increase in conductivity.

4.2 Role of Structure on Oxygen Ion Conduction in Zirconia- and Ceria-based Thin Films

As shown in Figure 58(b), for GDC films that had a thickness close to the grain size (20-60 nm), the lower activation energy is similar to what is normally found for GDC grain conduction, whereas for the films that are thicker than the grain size, the activation energy approached that of GDC grain boundaries. A few researchers have reported comparable results. As described previously, Huang et al. [70] observed that the impedance arc corresponding to the grain boundary disappeared for the thinner films; however, since our measurement is, unlike that of Huang et al., parallel to the substrate, the number of grain boundaries in the current path in the samples reported here does not change with film thickness. An activation energy of 0.74 eV was reported by Chen [86] for 20 mol% GDC epitaxial films, where a lack of grain boundary resistance is again to be expected. Suzuki et al. [66] reported 1 eV – 1.3 eV for polycrystalline thin films of the same composition. Similar aging behavior to what is reported here was observed by Chen et al. [87], who obtained an activation energy 0.86 eV for fresh GDC thin films on MgO and 0.74 eV for aged GDC thin films. This may be related to recrystallization near low angle grain boundaries, which may help the grain boundaries to become more ordered and reduce their blocking effect.

Given the columnar grain structure, it is perhaps surprising that the conduction behavior changes from grain boundary- to grain-controlled as the film thickness decreases. Grain boundary resistance is likely to be reduced for very low angle grain boundaries, which were conclusively found for YSZ films deposited under identical conditions. At increased film thickness, grain boundary distortions are found as shown in Figure 41(b), indicating that the grain boundaries are increasingly disordered and more likely to contribute significantly to the overall impedance. In addition, the

increasingly disordered fields in grain boundary may introduce microstrain in the biphasic amorphous-crystalline microstructure, which may change the ionic conductivity [54]. Aging may then help the grain structure surrounding the boundaries to become more ordered and decrease the activation energy as shown in Figure 58(b).

For the (111) oriented GDC thin films on Al_2O_3 (0001), as the GDC thin films became thicker, the grain boundaries got more distortion, which may make that grain boundary contributes more to the conductivity. As shown in Figure 58, when the thickness was below 81 nm, the ionic conductivity magnitude increased with thickness while the activation energy remained constant at 0.75 eV, similar to the activation energy of bulk GDC grain [86]. For GDC thin films thicker than 81 nm, the ionic conductivity decreased and the activation energy increased with increasing thickness. It was supposed that the grain boundary conduction dominated as the grain boundary got more disordered and distorted when the thickness increased. The GDC thin films achieved highest conductivity at the thickness of 81 nm, but the highest conductivity was just 1 to 2 times higher than the bulk value.

For YSZ thin films on various substrate surfaces, as shown in Figure 35, the XRD intensity decreased sharply from the film deposited on polished sapphire to those on ion cleaned and milled sapphire, indicating that crystallinity decreased accordingly. Here, crystallinity refers to the degree of structural order such that better crystallinity means less amorphous phase in the thin film. As shown in Figure 49, the conductivity decreased in the same order, high XRD intensity corresponding to high conductivity. Further, YSZ films on 30 min and 60 min ion cleaned sapphire exhibited nearly the same XRD intensity and nearly the same conductivity. Perhaps more telling results in this regard are found in the YSZ-MgO system. Figure 27 shows that ion

cleaning of the MgO substrate surface served to change the film's orientation from (111) to (100) yet did not decrease the XRD intensity. Figure 46 shows that the conductivity of these films is very similar, with the conductivity only decreasing for the film with significantly reduced XRD intensity on the milled MgO surface.

An ion blocking effect of grain boundaries would suggest a corresponding relationship between crystallinity and conductivity. Guo and Maier [51] found that the grain boundary resistivity of YSZ pellets was two or three orders of magnitude higher than the bulk resistivity, even in the absence of impurity phases. In addition, Navickas et al. [44] reasoned that an increase of conductivity in YSZ thin films with columnar microstructure by one order of magnitude in the across-plane direction relative to the through-plane direction can be attributed to the blocking effect of grain boundaries. In addition, Schlupp and Gauckler [88] measured the across-plane conductivity of YSZ thin films with different microstructures and found the grain boundary conductivity was around 0.002 S/cm at 500 °C, while the grain conductivity was around 0.1 S/cm at 500 °C.

Here, more evidence supporting this hypothesis is found. The YSZ thin films on ion cleaned sapphire surfaces had highly decreased crystallinity compared with the film on polished sapphire, and thus a greater concentration of disordered grain boundaries are likely. The increased volume fraction of grain boundaries is believed to dominate the conduction behavior, decreasing the conductivity. On milled MgO, the appearance of both (111) and (100) oriented grains again suggests the thin film is more disordered compared with the films displaying predominantly a single orientation, and again it seems to have induced lower conductivity.

The annealing effect (Figure 50), especially with a high annealing temperature like 1000 °C, may be also explained with the evolution of microstructure. The grain size was increased significantly from 27 nm to 33 nm when films were annealed at 1000°C. A similar grain coarsening was reported by Rodrigo et al. [89] on gadolinia-doped ceria (GDC) thin films. The GDC thin films prepared using PLD at 400 °C show a grain size close to 11 nm, which increased to 30 – 40 nm after annealing at 800 °C for 10 h. The increased grain size would decrease the grain boundary density accordingly. Here, for the annealed film at 1000 °C, lower grain boundary density mitigated the overall blocking effect from grain boundaries and increased the ionic conductivity.

Annealing under lower temperatures, like 650 °C and 800 °C was insufficient to improve the microstructure and increase the grain size. Sillassen et al. [90] also found the grain growth was negligible for samples deposited at 400 °C and then annealed at 800 °C for 1 h. However, prolonging the 800 °C annealing to 20 h also increased the conductivity. The increase may be related to the grain boundary ordering. Although 800 °C seems too low to increase the grain size, the grain boundary may evolve more ordered under 800 °C if the annealing process was long enough. The more ordered structure of grain boundary may decrease the blocking effect. The lower activation energy (1.02 eV) compared with other samples supports the decreased blocking effect for the ionic conduction.

4.3 Proton Conduction supported by YSZ Thin Films

The results given in Section 3.5 at measurement temperatures above 550 °C coincide well with the high temperature measurements given by Guo et al. [33], with nanoscale YSZ thin films exhibiting similar conductivities in both dry and humidified

air. Studies by Scherrer et al. [91], Tande et al. [92], and Avila-Paredes et al. [93-95] focused on proton conduction at low temperatures (from room temperature up to 400 °C) and observed proton conduction especially close to room temperature. Scherrer et al. [91] reported significant proton conduction for porous but not dense YSZ films below 400 °C. One reason for the different electrical property of these dense films compared to those in this study is likely because the previous studies measured films that were a few hundreds nanometer thick, much thicker than the films in this study.

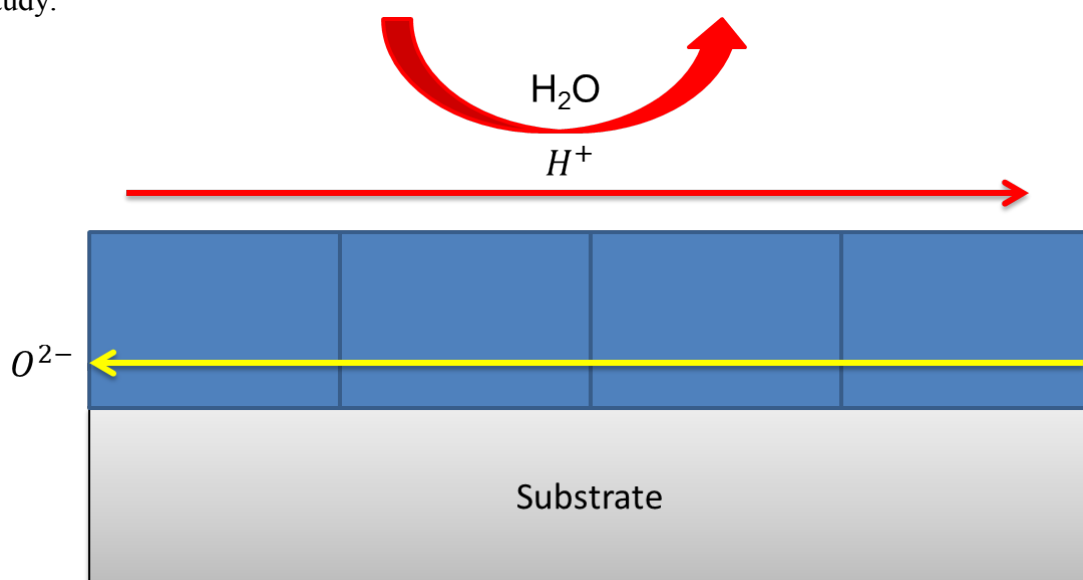
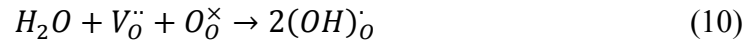


Figure 59 Schematic diagram of proton conduction

No significant proton conduction through grain boundaries can be concluded here. The lateral grain sizes of 6nm thick film and 50 nm thick film are comparable, while the grain size perpendicular to the substrate is 6 nm for 6 nm thick films and 28 nm for 50 nm thick film according to Scherrer equation. Thus, the volume fraction of grain boundaries is relatively similar in these two films, but somewhat larger in the

thicker film. If proton conduction were to be occurring via the grain boundaries, then the thicker film would exhibit greater proton conduction; this is not the behavior observed in this study.

The observation of proton conduction only in the thinner films suggests instead that proton conduction occurs at one or both interfaces, most likely the free surface exposed to the environment, as shown in Figure 59. In the intermediate temperature range (400 °C – 500 °C), water is likely to adsorb chemically on the oxide surfaces [96]. The associated defect chemical reaction on the surface is



This reaction produces proton defects $((OH)_{\text{O}}^{\bullet})$ on the oxide surface [97, 98].

If we assume that bulk oxygen ion conduction and surface proton conduction occur in parallel, as shown in Figure 59, then the resistance of surface conduction,

R_{sur} , is:

$$R_{sur} = \frac{1}{\frac{1}{R_{hum}} - \frac{1}{R_{dry}}} \quad (11)$$

where R_{hum} and R_{dry} are the sample resistances in humidified air and dry air, respectively. A surface conductivity is defined as:

$$\sigma_{sur} = \frac{D}{l * R_{sur}} \quad (12)$$

where, σ_{sur} , D , and l are the surface conductivity, the inter-electrode spacing, and the total length of the electrodes, respectively. Figure 60 shows an Arrhenius plot of the surface conductivity of the 6 nm thick film. Below 500 °C, the surface conductivity is thermally activated with an activation energy of 1.03 eV. This activation energy is very close to conventional values of YSZ oxygen ion conduction.

Based on Equation (11) and (12), the total conductivity in humid air, σ_{hum} , is:

$$\sigma_{hum} = \sigma_{dry} + \frac{\sigma_{sur}}{t} \quad (13)$$

where, σ_{dry} and t are the conductivity in the dry air and the thickness of film, respectively. As shown in Figure 61, as t increases, σ_{sur} contributes less to the overall conductivity. This explains when the thickness of YSZ thin films increases from 6 nm to 50 nm, the surface conduction becomes less perceptible.

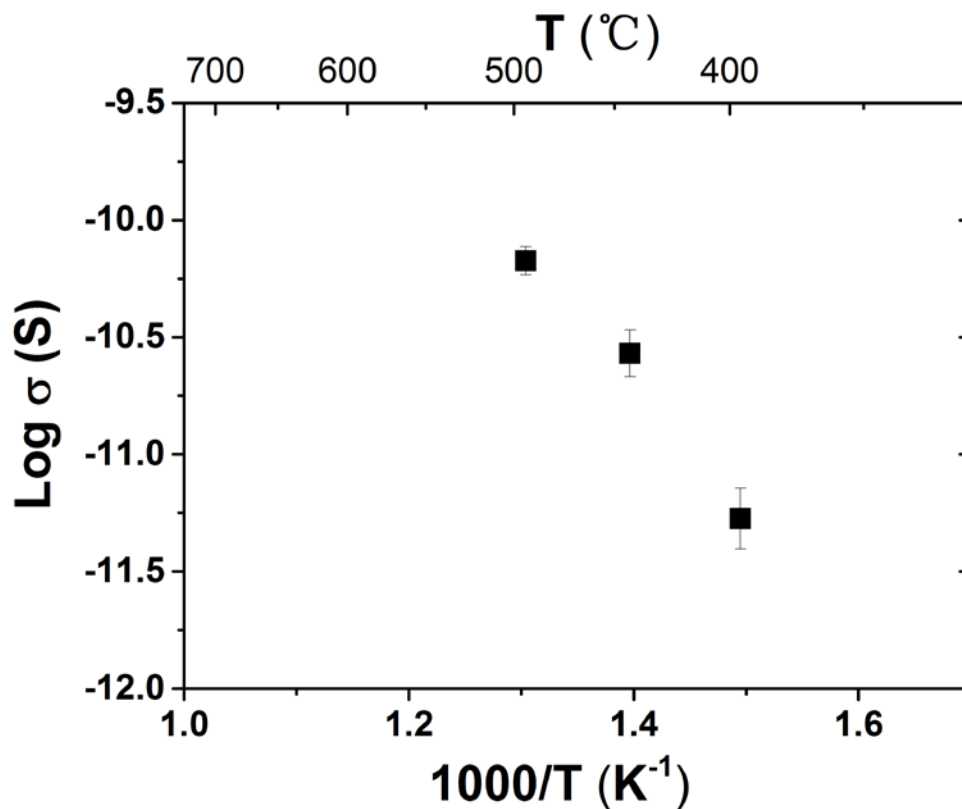


Figure 60 Arrhenius plot of the surface conductivity of the 6 nm thick YSZ thin film measured in the flowing humidified air with a water vapor partial pressure of 32 mbar

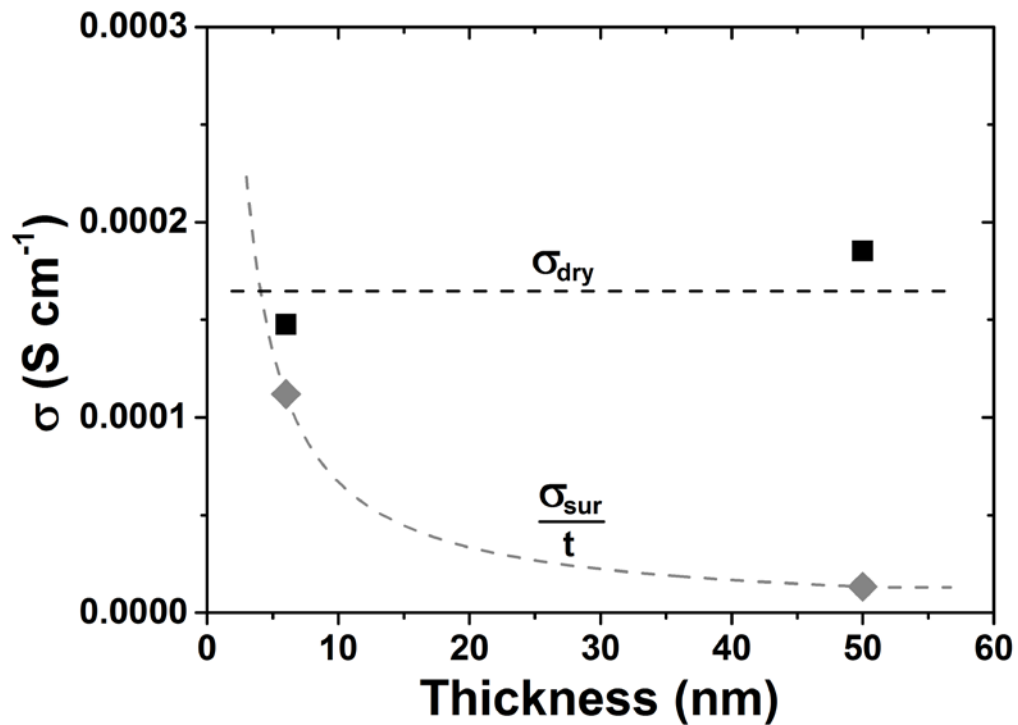


Figure 61 The thickness dependence of conductivity at 500 °C

When measuring the sample in open laboratory air, the sample had the same conductivity as in humidified air. The similarity of these values suggests that all available adsorption sites are filled at these water vapor pressures, and that open air offers sufficient water vapor for this proton conduction mechanism at intermediate temperatures. Literature reports[99] have reported that the impedance of nanoparticle ZrO₂ film changed four orders of magnitude when the relative humidity varied from 11% to 98%, which indicates more water is adsorbed onto the top surface of oxides when the relative humidity increases.

Chapter 5

CONCLUSIONS

5.1 Summary

In this study, reactive RF co-sputtering with metal targets was used successfully to prepare zirconia and ceria based solid oxide electrolyte thin films with arbitrary composition within a solid solution space and with uniform thicknesses down to 6 nm.

YSZ thin films deposited on MgO (111) and, especially, MgO (100) showed highly variable crystal orientations, while MgO (110) offered much more stable growth. Regardless of whether the growth was epitaxial or highly disordered polycrystalline, 50 nm thick YSZ thin films on MgO (100), (110), and (111) substrates exhibited similar conductivity with YSZ single crystal. While decreasing the thickness further to 12 nm, the conductivities of YSZ thin films were decreased 3 – 7 times. YSZ thin films deposited on Al_2O_3 obtained a stable epitaxial growth along $[110] (111)\text{YSZ} // [10\bar{1}0] (0001)\text{Al}_2\text{O}_3$. The films had compressive in-plane strain and dilatative out-of-plane strain, with the amount of strain increasing as the film thicknesses decreased. By tailoring the thickness of YSZ thin film on Al_2O_3 from 100 nm to 6 nm, the lattice strain can be increased from 1% to 2%. The corresponding conductivity increased by about 1 order of magnitude and the activation energy decreased from 0.99 eV to 0.79 eV.

Ion cleaning of the MgO substrate surface was found to change the YSZ thin films' texture from (111) to (100) without large change to the conductivity, while ion

cleaning of the Al_2O_3 substrate surface decreased the crystallinity without changing the texture and reduced the ionic conductivity of YSZ thin films by a factor of 4. Thus, crystallinity not texture was found to determine the ionic conductivity. Substrate surface structure was proven to change the microstructure of films, and poorer crystallinity leads to decreased ionic conductivity. Variations in the substrate surface were found to decrease the conductivity of YSZ thin films by over one order of magnitude. In addition, a post annealing with a temperature as high as $1000\text{ }^\circ\text{C}$ was able to increase the crystallinity of YSZ thin films therefore increasing the conductivity by a factor of 2. Post annealing was found to be important to determine the microstructure and electrical property of YSZ thin films.

By decreasing the thickness of YSZ thin films to 6 nm, surface proton conduction becomes significant. The results suggest that for ultrathin YSZ films, not only the electron/hole conduction but also proton conduction should be considered. Proton conduction takes place along film interfaces instead of the grain boundaries, based on the correlation of the electrical performance and microstructure of thin films. The proton conduction had an activation energy of 1.03 eV.

Based on the above research findings, the variation of reported YSZ thin film conductivity comes from: an underappreciated importance of surface proton conduction, increased conductivity with substrate-induced strain in epitaxial or nearly epitaxial films and reduced conductivity with poor crystallinity.

GDC thin films deposited on MgO were randomly oriented along multi axes, suggesting a polycrystalline structure. While, on Al_2O_3 , GDC thin films' growth became stable only oriented in (111) orientation, just like YSZ thin films on Al_2O_3 . In the thickness range of 15 nm – 173 nm, the maximum conductivity of GDC thin films

was obtained at the thickness of 81 nm. Interestingly, as GDC thin films' thickness increases above 100 nm, the electrical properties changes from a bulk-like conduction to a grain boundary-like conduction. When the thickness was close to the grain size (20-60 nm), the ionic conductivity behavior was dominated by grain conduction with an activation energy of ≈ 0.75 eV and increased with increasing thickness. When the thickness was much larger than the grain size (above 100 nm), the ionic conductivity became controlled by grain boundary conduction and decreased with increasing thickness as the activation energy increased. The activation energy decreased for the thicker films upon annealing. Combined with TEM characterization, the results indicate that increasingly disordered grain boundary structure is found at increased thickness. A moderate amount of lattice strain is indicated in the thinnest films, but out-of-plane dilation is believed to be insufficient to overcome in-plane compression, leading to a net decrease in conductivity.

5.2 Recommendations for Future Work

The research described above raises additional questions.

(1) The high stability of YSZ/ Al_2O_3 system has not been well explained. Compared with YSZ/MgO system, YSZ/ Al_2O_3 system always offers an epitaxial growth along $[110] (111)\text{YSZ} // [10\bar{1}0] (0001)\text{Al}_2\text{O}_3$. Even on ion cleaned and milled Al_2O_3 substrate surface, YSZ thin films still orient in (111) directions. While even on MgO (100) polished surface, YSZ thin films show variable orientations. The high stability can be partly explained by the similarity of atom symmetry on Al_2O_3 (0001) and YSZ (111) surface, which are both three-fold geometry. Compared with MgO, Al_2O_3 offers a lattice parameter closer to that of YSZ, which decreases the lattice mismatch.

However, YSZ is an ionic crystal and the atomic bonding shows anisotropic property. The crystallography is insufficient to explain the interface match. The Zr-Y, Zr-O, Y-O bonding and atomic surface energy should be taken into account for the stability. DFT calculation may be a suitable tool to analyze this problem.

(2) The effect of strain on the ionic conductivity has been concluded in the thesis. But we observed both tensile out-of-plane strain and compressive in-plane strain at the same time. In the literature, the tensile strain increases the conductivity while the compressive strain decreases the conductivity. Then what is the overall effect of tensile strain and compressive strain? Whether it increases or decreases the conductivity?

A separated study of tensile and compressive strain is proposed here. The tensile out-of-plane strain and compressive in-plane strain can be quantified simultaneously using an aberration corrected TEM. By exit wave reconstruction, strain mapping can be obtained. Fitting the overall effect of strain on conductivity to both variable tensile and compressive strain will achieve the separated effect for tensile strain and compressive strain.

(3) Although the blocking effect of grain boundary has been emphasized in the thesis, the quantification of the blocking effect is still not quite clear. There are not sufficient reports quantifying the blocking effect of grain boundary for several reasons. First, although the resistance of grain boundary may be easily obtained, an accurate conductivity may be hard to achieve as the geometry of grain boundary is usually not quite clear and hard to quantify. So the reported conductivity of grain boundary is quite rough. Second, the chemical composition, defect species and crystallinity of grain boundary are different from sample to sample, so they exhibited different

blocking effects (high or low). So the sample with a certain microstructure shows an unknown conductivity without the clear quantification of conductivity in grain boundary.

REFERENCES

1. Minh, N.Q., *Ceramic Fuel-Cells*. Journal of the American Ceramic Society, 1993. **76**(3): p. 563-588.
2. Wachsman, E.D. and K.T. Lee, *Lowering the Temperature of Solid Oxide Fuel Cells*. Science, 2011. **334**(6058): p. 935-939.
3. Baur, E. and H. Preis, *Über Brennstoff-Ketten mit Festleitern*. Z. Elektrochem., 1937. **43**: p. 727-732.
4. Ahn, J.S., et al., *High-performance bilayered electrolyte intermediate temperature solid oxide fuel cells*. Electrochemistry Communications, 2009. **11**(7): p. 1504-1507.
5. Faraday, M., *Experimental research in electricity art*. 1339 (London: Taylor and Francis), 1839.
6. Nernst, W., *Mutter erde*, 1899. **2**: p. 192.
7. Scott, H.G., *Phase Relationships in Zirconia-Yttria System*. Journal of Materials Science, 1975. **10**(9): p. 1527-1535.
8. http://www.doitpoms.ac.uk/tlplib/fuel-cells/sofc_electrolyte.php?printable=1.
9. Arachi, Y., et al., *Electrical conductivity of the $ZrO_2-Ln(2)O(3)$ ($Ln = \text{lanthanides}$) system*. Solid State Ionics, 1999. **121**(1-4): p. 133-139.
10. Yamamoto, O., *Solid oxide fuel cells: fundamental aspects and prospects*. Electrochimica Acta, 2000. **45**(15-16): p. 2423-2435.
11. Jiang, J., W.D. Shen, and J.L. Hertz, *Fabrication of epitaxial zirconia and ceria thin films with arbitrary dopant and host atom composition*. Thin Solid Films, 2012. **522**: p. 66-70.
12. Jung, W., J.L. Hertz, and H.L. Tuller, *Enhanced ionic conductivity and phase meta-stability of nano-sized thin film yttria-doped zirconia (YDZ)*. Acta Materialia, 2009. **57**(5): p. 1399-1404.
13. Gerstl, M., et al., *Measurement of (^{18}O) tracer diffusion coefficients in thin yttria stabilized zirconia films*. Solid State Ionics, 2011. **184**(1): p. 23-26.
14. Opitz, A.K. and J. Fleig, *Investigation of $O(2)$ reduction on Pt/YSZ by means of thin film microelectrodes: The geometry dependence of the electrode impedance*. Solid State Ionics, 2010. **181**(15-16): p. 684-693.
15. Radhakrishnan, R., A.V. Virkar, and S.C. Singhal, *Estimation of charge-transfer resistivity of $La_{0.8}Sr_{0.2}MnO_3$ cathode on $Y_{0.16}Zr_{0.84}O_2$ electrolyte using patterned electrodes*. Journal of the Electrochemical Society, 2005. **152**(1): p. A210-A218.
16. Evans, A., et al., *Review on microfabricated micro-solid oxide fuel cell membranes*. Journal of Power Sources, 2009. **194**(1): p. 119-129.

17. Baertsch, C.D., et al., *Fabrication and structural characterization of self-supporting electrolyte membranes for a micro solid-oxide fuel cell*. Journal of Materials Research, 2004. **19**(9): p. 2604-2615.
18. Birkholz, M., *Thin Film Analysis by X-Ray Scattering*. "Thin Film Analysis by X-Ray Scattering", 2006 WILEY-VCH Verlag GmbH & Co. KGaA, Weinheim.
19. Johnson, A.C., et al., *Fabrication and electrochemical performance of thin-film solid oxide fuel cells with large area nanostructured membranes*. Journal of Power Sources, 2010. **195**(4): p. 1149-1155.
20. Kim, S.G., et al., *Fabrication and characterization of a YSZ/YDC composite electrolyte by a sol-gel coating method*. Journal of Power Sources, 2002. **110**(1): p. 222-228.
21. Zhang, Y.W., et al., *Electrical conductivity enhancement in nanocrystalline (RE₂O₃)_(0.08)(ZrO₂)_(0.92) (RE=Sc, Y) thin films*. Applied Physics Letters, 2000. **77**(21): p. 3409-3411.
22. Matsuda, M., et al., *Fabrication of bilayered YSZ/SDC electrolyte film by electrophoretic deposition for reduced-temperature operating anode-supported SOFC*. Journal of Power Sources, 2007. **165**(1): p. 102-107.
23. Karthikeyan, A., C.L. Chang, and S. Ramanathan, *High temperature conductivity studies on nanoscale yttria-doped zirconia thin films and size effects*. Applied Physics Letters, 2006. **89**(18).
24. Wu, S.G., et al., *Y₂O₃ stabilized ZrO₂ thin films deposited by electron beam evaporation: Structural, morphological characterization and laser induced damage threshold*. Applied Surface Science, 2006. **253**(3): p. 1561-1565.
25. Boulouz, M., et al., *Effect of the dopant content on the physical properties of Y₂O₃-ZrO₂ and CaO-ZrO₂ thin films produced by evaporation and sputtering techniques*. Materials Science and Engineering B-Solid State Materials for Advanced Technology, 1999. **67**(3): p. 122-131.
26. Hata, T., et al., *Yttria-stabilized zirconia (YSZ) heteroepitaxially grown on Si substrates by reactive sputtering*. Vacuum, 2000. **59**(2-3): p. 381-389.
27. Sanna, S., et al., *Fabrication and Electrochemical Properties of Epitaxial Samarium-Doped Ceria Films on SrTiO₃-Buffered MgO Substrates*. Advanced Functional Materials, 2009. **19**(11): p. 1713-1719.
28. Sanna, S., et al., *Enhancement of Ionic Conductivity in Sm-Doped Ceria/Yttria-Stabilized Zirconia Heteroepitaxial Structures*. Small, 2010. **6**(17): p. 1863-1867.
29. De Jonghe, L.C., C.P. Jacobson, and S.J. Visco, *Supported electrolyte thin film synthesis of solid oxide fuel cells*. Annual Review of Materials Research, 2003. **33**: p. 169-182.
30. Kosacki, I., et al., *Electrical conductivity of nanocrystalline ceria and zirconia thin films*. Solid State Ionics, 2000. **136**: p. 1225-1233.

31. Sillassen, M., et al., *Low-Temperature Superionic Conductivity in Strained Yttria-Stabilized Zirconia*. *Advanced Functional Materials*, 2010. **20**(13): p. 2071-2076.
32. Jiang, J., et al., *Improved ionic conductivity in strained yttria-stabilized zirconia thin films*. *Applied Physics Letters*, 2013. **102**(14).
33. Guo, X., et al., *Ionic conduction in zirconia films of nanometer thickness*. *Acta Materialia*, 2005. **53**(19): p. 5161-5166.
34. Navickas, E., et al., *Measurement of the across-plane conductivity of YSZ thin films on silicon*. *Solid State Ionics*, 2012. **211**: p. 58-64.
35. Joo, J.H. and G.M. Choi, *Electrical conductivity of YSZ film grown by pulsed laser deposition*. *Solid State Ionics*, 2006. **177**(11-12): p. 1053-1057.
36. Rivera, A., J. Santamaria, and C. Leon, *Electrical conductivity relaxation in thin-film yttria-stabilized zirconia*. *Applied Physics Letters*, 2001. **78**(5): p. 610-612.
37. Gerstl, M., et al., *The relevance of interfaces for oxide ion transport in yttria stabilized zirconia (YSZ) thin films*. *Physical Chemistry Chemical Physics*, 2013. **15**(4): p. 1097-1107.
38. Jiang, J. and J.L. Hertz, *On the variability of reported ionic conductivity in nanoscale YSZ thin films*. *Journal of Electroceramics*, 2014. **32**(1): p. 37-46.
39. Garcia-Barriocanal, J., et al., *Colossal ionic conductivity at interfaces of epitaxial ZrO(2): Y(2)O(3)/SrTiO(3) heterostructures*. *Science*, 2008. **321**(5889): p. 676-680.
40. Sillassen, M., et al., *Low-Temperature Superionic Conductivity in Strained Yttria-Stabilized Zirconia (vol 20, pg 2071, 2010)*. *Advanced Functional Materials*, 2010. **20**(19): p. 3194-3194.
41. Schichtel, N., et al., *Elastic strain at interfaces and its influence on ionic conductivity in nanoscaled solid electrolyte thin films-theoretical considerations and experimental studies*. *Physical Chemistry Chemical Physics*, 2009. **11**(17): p. 3043-3048.
42. Kosacki, I., et al., *Surface interface-related conductivity in nanometer thick YSZ films*. *Electrochemical and Solid State Letters*, 2004. **7**(12): p. A459-A461.
43. Kim, H.R., et al., *'Illusional' nano-size effect due to artifacts of in-plane conductivity measurements of ultra-thin films*. *Physical Chemistry Chemical Physics*, 2011. **13**(13): p. 6133-6137.
44. Navickas, E., et al., *Simultaneous Measurement of the In- and Across-Plane Ionic Conductivity of YSZ Thin Films*. *Journal of the Electrochemical Society*, 2012. **159**(4): p. B411-B416.
45. Kosacki, I., et al., *Nanoscale effects on the ionic conductivity in highly textured YSZ thin films*. *Solid State Ionics*, 2005. **176**(13-14): p. 1319-1326.
46. Karthikeyan, A., M. Tsuchiya, and S. Ramanathan, *Studies on structure-electrochemical conduction relationships in doped-zirconia thin films*. *Solid State Ionics*, 2008. **179**(21-26): p. 1234-1237.

47. Aoki, M., et al., *Solute segregation and grain-boundary impedance in high-purity stabilized zirconia*. Journal of the American Ceramic Society, 1996. **79**(5): p. 1169-1180.
48. Henzler, M., *Texture of Surfaces Cleaned by Ion Bombardment and Annealing*. Surface Science, 1970. **22**(1): p. 12-&.
49. Kim, K.S. and N. Winograd, *X-Ray Photoelectron Spectroscopic Studies of Nickel-Oxygen Surfaces Using Oxygen and Argon Ion-Bombardment*. Surface Science, 1974. **43**(2): p. 625-643.
50. Frija, M., et al., *Finite element modelling of shot peening process: Prediction of the compressive residual stresses, the plastic deformations and the surface integrity*. Materials Science and Engineering a-Structural Materials Properties Microstructure and Processing, 2006. **426**(1-2): p. 173-180.
51. Guo, X. and J. Maier, *Grain boundary blocking effect in zirconia: A Schottky barrier analysis*. Journal of the Electrochemical Society, 2001. **148**(3): p. E121-E126.
52. Thompson, C.V., *On the grain size and coalescence stress resulting from nucleation and growth processes during formation of polycrystalline thin films*. Journal of Materials Research, 1999. **14**(7): p. 3164-3168.
53. Quinn, D.J., B. Wardle, and S.M. Spearing, *Residual stress and microstructure of as-deposited and annealed, sputtered yttria-stabilized zirconia thin films*. Journal of Materials Research, 2008. **23**(3): p. 609-618.
54. Rupp, J.L.M., *Ionic diffusion as a matter of lattice-strain for electroceramic thin films*. Solid State Ionics, 2012. **207**: p. 1-13.
55. Kushima, A. and B. Yildiz, *Oxygen ion diffusivity in strained yttria stabilized zirconia: where is the fastest strain?* Journal of Materials Chemistry, 2010. **20**(23): p. 4809-4819.
56. Hayashi, H., et al., *Thermal expansion coefficient of yttria stabilized zirconia for various yttria contents*. Solid State Ionics, 2005. **176**(5-6): p. 613-619.
57. Vonk, V., et al., *Atomic structure and composition of the yttria-stabilized zirconia (111) surface*. Surface Science, 2013. **612**: p. 69-76.
58. Korte, C., et al., *Influence of interface structure on mass transport in phase boundaries between different ionic materials Experimental studies and formal considerations*. Monatshefte Fur Chemie, 2009. **140**(9): p. 1069-1080.
59. Schichtel, N., et al., *On the influence of strain on ion transport: microstructure and ionic conductivity of nanoscale YSZ vertical bar Sc2O3 multilayers*. Physical Chemistry Chemical Physics, 2010. **12**(43): p. 14596-14608.
60. Korte, C., et al., *Ionic conductivity and activation energy for oxygen ion transport in superlattices - the semicoherent multilayer system YSZ (ZrO(2)+9.5 mol% Y(2)O(3))/Y(2)O(3)*. Physical Chemistry Chemical Physics, 2008. **10**(31): p. 4623-4635.
61. Aydin, H., et al., *Oxygen tracer diffusion along interfaces of strained Y2O3/YSZ multilayers*. Physical Chemistry Chemical Physics, 2013. **15**(6): p. 1944-1955.

62. Aydin, H., C. Korte, and J. Janek, *O-18-tracer diffusion along nanoscaled Sc₂O₃/yttria stabilized zirconia (YSZ) multilayers: on the influence of strain*. Science and Technology of Advanced Materials, 2013. **14**(3).
63. Park, J.Y. and E.D. Wachsman, *Stable and high conductivity ceria/bismuth oxide bilayer electrolytes for lower temperature solid oxide fuel cells*. Ionics, 2006. **12**(1): p. 15-20.
64. Saraf, L., et al., *Oxygen transport studies in nanocrystalline ceria films*. Journal of Materials Research, 2005. **20**(5): p. 1295-1299.
65. Rupp, J.L.M. and L.J. Gauckler, *Microstructures and electrical conductivity of nanocrystalline ceria-based thin films*. Solid State Ionics, 2006. **177**(26-32): p. 2513-2518.
66. Suzuki, T., I. Kosacki, and H.U. Anderson, *Microstructure-electrical conductivity relationships in nanocrystalline ceria thin films*. Solid State Ionics, 2002. **151**(1-4): p. 111-121.
67. Chiodelli, G., et al., *Synthesis and characterization of Ce_{0.8}Gd_{0.2}O_{2-y} polycrystalline and thin film materials*. Solid State Ionics, 2005. **176**(17-18): p. 1505-1512.
68. Bieberle-Hutter, A., J.L. Hertz, and H.L. Tuller, *Fabrication and electrochemical characterization of planar Pt-CGO microstructures*. Acta Materialia, 2008. **56**(2): p. 177-187.
69. Jiang, J., W.D. Shen, and J.L. Hertz, *Structure and ionic conductivity of nanoscale gadolinia-doped ceria thin films*. Solid State Ionics, 2013. **249-250**: p. 139-143.
70. Huang, H., et al., *High ionic conductivity in ultrathin nanocrystalline gadolinia-doped ceria films*. Applied Physics Letters, 2006. **89**(14).
71. Lee, K.R., et al., *Lattice distortion effect on electrical properties of GDC thin films: Experimental evidence and computational simulation*. Solid State Ionics, 2012. **229**: p. 45-53.
72. Sata, N., et al., *Mesosopic fast ion conduction in nanometre-scale planar heterostructures*. Nature, 2000. **408**(6815): p. 946-949.
73. Jiang, J., et al., *Microstructure and ionic conductivity of yttria-stabilized zirconia thin films deposited on MgO*. Journal of the American Ceramic Society: p. DOI: 10.1111/jace.12740.
74. Fischer, R., et al., *Material Properties of High-Quality Gaas Epitaxial Layers Grown on Si Substrates*. Journal of Applied Physics, 1986. **60**(5): p. 1640-1647.
75. Kim, S., Y.M. Kang, and S. Baik, *Growth of Pbtio₃ Thin-Films by Rf-Sputtering on Vicinal Mgo(100) Substrates*. Thin Solid Films, 1995. **256**(1-2): p. 240-246.
76. Jiang, J., et al., *The effects of Substrate Surface Structure on Ytria-stabilized Zirconia Thin Films*. Applied Surface Science, 2014. **293**: p. 191.

77. Hamaguchi, S. and S.M. Rosnagel, *Liner conformality in ionized magnetron sputter metal deposition processes*. Journal of Vacuum Science & Technology B, 1996. **14**(4): p. 2603-2608.
78. De Souza, R.A., et al., *Oxygen diffusion in nanocrystalline yttria-stabilized zirconia: the effect of grain boundaries*. Physical Chemistry Chemical Physics, 2008. **10**(15): p. 2067-2072.
79. Bray, D.T. and U. Merten, *Transport Numbers in Stabilized Zirconia*. Journal of the Electrochemical Society, 1964. **111**(4): p. 447-452.
80. Jiang, J., W. Shen, and J.L. Hertz, *Structure and ionic conductivity of nanoscale gadolinia-doped ceria thin films*. Solid State Ionics, 2013. **249**: p. 139-143.
81. Joo, J.H. and G.M. Choi, *Electrical conductivity of thin film ceria grown by pulsed laser deposition*. Journal of the European Ceramic Society, 2007. **27**(13-15): p. 4273-4277.
82. Gerstl, M., et al., *The separation of grain and grain boundary impedance in thin yttria stabilized zirconia (YSZ) layers*. Solid State Ionics, 2011. **185**(1): p. 32-41.
83. Sankaranarayanan, S.K.R.S. and S. Ramanathan, *Interface proximity effects on ionic conductivity in nanoscale oxide-ion conducting yttria stabilized zirconia: An atomistic simulation study*. Journal of Chemical Physics, 2011. **134**(6).
84. Otsuka, K., et al., *Dislocation-enhanced ionic conductivity of yttria-stabilized zirconia*. Applied Physics Letters, 2003. **82**(6): p. 877-879.
85. Zha, S.W., C.R. Xia, and G.Y. Meng, *Effect of Gd (Sm) doping on properties of ceria electrolyte for solid oxide fuel cells*. Journal of Power Sources, 2003. **115**(1): p. 44-48.
86. Chen, L., et al., *High temperature electrical conductivity of epitaxial Gd-doped CeO₂ thin films*. Solid State Ionics, 2004. **175**(1-4): p. 103-106.
87. Chen, L., et al., *Electrical properties of a highly oriented, textured thin film of the ionic conductor Gd : CeO₂-delta on (001) MgO*. Applied Physics Letters, 2003. **83**(23): p. 4737-4739.
88. Schlupp, M.V.F., et al., *Influence of microstructure on the cross-plane oxygen ion conductivity of yttria stabilized zirconia thin films*. Physica Status Solidi a-Applications and Materials Science, 2012. **209**(8): p. 1414-1422.
89. Rodrigo, K., et al., *The effects of thermal annealing on the structure and the electrical transport properties of ultrathin gadolinia-doped ceria films grown by pulsed laser deposition*. Applied Physics a-Materials Science & Processing, 2011. **104**(3): p. 845-850.
90. Sillassen, M., et al., *Ionic conductivity and thermal stability of magnetron-sputtered nanocrystalline yttria-stabilized zirconia*. Journal of Applied Physics, 2009. **105**(10).
91. Scherrer, B., et al., *On Proton Conductivity in Porous and Dense Yttria Stabilized Zirconia at Low Temperature*. Advanced Functional Materials, 2013. **23**: p. 1957-1964.

92. Tande, C., D. Perez-Coll, and G.C. Mather, *Surface proton conductivity of dense nanocrystalline YSZ*. Journal of Materials Chemistry, 2012. **22**(22): p. 11208-11213.
93. Kim, S., et al., *On the conduction pathway for protons in nanocrystalline yttria-stabilized zirconia*. Physical Chemistry Chemical Physics, 2009. **11**(17): p. 3035-3038.
94. Avila-Paredes, H.J., et al., *Room-temperature protonic conduction in nanocrystalline films of yttria-stabilized zirconia*. Journal of Materials Chemistry, 2010. **20**(30): p. 6235-6238.
95. Avila-Paredes, H.J., et al., *Protonic conductivity of nano-structured yttria-stabilized zirconia: dependence on grain size*. Journal of Materials Chemistry, 2010. **20**(5): p. 990-994.
96. Raz, S., et al., *Characterization of adsorbed water layers on Y2O3-doped ZrO2*. Solid State Ionics, 2001. **143**(2): p. 181-204.
97. Kreuer, K.D., et al., *Transport in proton conductors for fuel-cell applications: Simulations, elementary reactions, and phenomenology*. Chemical Reviews, 2004. **104**(10): p. 4637-4678.
98. X, G., *Property degradation of tetragonal zirconia induced by low-temperature defect reaction with water molecules*. Chemistry of Materials, 2004. **16**(21): p. 3988-3994.
99. Wang, J., et al., *Sensitivity and complex impedance of nanometer zirconia thick film humidity sensors*. Sensors and Actuators B-Chemical, 2009. **139**(2): p. 418-424.

Appendix A

REPRINT PERMISSION LETTERS

Permission letters for reprinting of Figure 2, 4, 5 and 10 are listed below:

Figure 2

License Number	3430550593287
License date	Jul 15, 2014
Licensed content publisher	Springer
Licensed content publication	Journal of Materials Science (full set)
Licensed content title	Phase relationships in the zirconia-yttria system
Licensed content author	H. G. Scott
Licensed content date	Jan 1, 1975
Volume number	10
Issue number	9
Type of Use	Thesis/Dissertation
Portion	Figures
Author of this Springer article	No
Order reference number	None
Original figure numbers	3
Title of your thesis / dissertation	The Role of Strain and Structure on Oxygen Ion Conduction in Nanoscale Zirconia and Ceria Thin films
Expected completion date	Jul 2014
Estimated size(pages)	140
Total	0.00 USD
Terms and Conditions	

Figure 4

Supplier	Elsevier Limited The Boulevard,Langford Lane Kidlington,Oxford,OX5 1GB,UK
Registered Company Number	1982084
Customer name	Jun Jiang
Customer address	126 Spencer Lab, University of Delaware Newark, DE 19716
License number	3426140382620
License date	Jul 11, 2014
Licensed content publisher	Elsevier
Licensed content publication	Solid State Ionics
Licensed content title	Electrical conductivity of the ZrO ₂ -Ln ₂ O ₃ (Ln=lanthanides) system
Licensed content author	Y. Arachi,H. Sakai,O. Yamamoto,Y. Takeda,N. Imanishai
Licensed content date	June 1999
Licensed content volume number	121
Licensed content issue number	1-4
Number of pages	7
Start Page	133
End Page	139
Type of Use	reuse in a thesis/dissertation
Portion	figures/tables/illustrations
Number of figures/tables/illustrations	4
Format	both print and electronic
Are you the author of this Elsevier article?	No
Will you be translating?	No
Title of your thesis/dissertation	The Role of Strain and Structure on Oxygen Ion Conduction in Nanoscale Zirconia and Ceria Thin films
Expected completion date	Jul 2014

Estimated size (number of pages)	140
Elsevier VAT number	GB 494 6272 12
Permissions price	0.00 USD
VAT/Local Sales Tax	0.00 USD / 0.00 GBP
Total	0.00 USD
Terms and Conditions	

Figure 5

Supplier	Elsevier Limited The Boulevard,Langford Lane Kidlington,Oxford,OX5 1GB,UK
Registered Company Number	1982084
Customer name	Jun Jiang
Customer address	126 Spencer Lab, University of Delaware Newark, DE 19716
License number	3426140835143
License date	Jul 11, 2014
Licensed content publisher	Elsevier
Licensed content publication	Electrochimica Acta
Licensed content title	Solid oxide fuel cells: fundamental aspects and prospects
Licensed content author	Osamu Yamamoto
Licensed content date	3 May 2000
Licensed content volume number	45
Licensed content issue number	15-16
Number of pages	13
Start Page	2423
End Page	2435
Type of Use	reuse in a thesis/dissertation
Intended publisher of new work	other
Portion	figures/tables/illustrations
Number of figures/tables/illustrations	7
Format	both print and electronic
Are you the author of this Elsevier article?	No
Will you be translating?	No
Title of your thesis/dissertation	The Role of Strain and Structure on Oxygen Ion Conduction in Nanoscale Zirconia and Ceria Thin films

Expected completion date	Jul 2014
Estimated size (number of pages)	140
Elsevier VAT number	GB 494 6272 12
Permissions price	0.00 USD
VAT/Local Sales Tax	0.00 USD / 0.00 GBP
Total	0.00 USD
Terms and Conditions	

Figure 10

License Number	3430551110336
License date	Jul 15, 2014
Licensed content publisher	Royal Society of Chemistry
Licensed content publication	Physical Chemistry Chemical Physics
Licensed content title	Elastic strain at interfaces and its influence on ionic conductivity in nanoscaled solid electrolyte thin films—theoretical considerations and experimental studies
Licensed content author	N. Schichtel,C. Korte,D. Hesse,J. Janek
Licensed content date	Mar 20, 2009
Volume number	11
Issue number	17
Type of Use	Thesis/Dissertation
Requestor type	academic/educational
Portion	figures/tables/images
Number of figures/tables/images	2
Format	print and electronic
Distribution quantity	1
Will you be translating?	no
Order reference number	None
Title of the thesis/dissertation	The Role of Strain and Structure on Oxygen Ion Conduction in Nanoscale Zirconia and Ceria Thin films
Expected completion date	Jul 2014
Estimated size	140
Total	0.00 USD
Terms and Conditions	